

EBERHARD KARLS  
UNIVERSITÄT  
TÜBINGEN



---

# Precision Calculations for Weakino- Pair Production at Hadron Colliders

---

Matthias KESENHEIMER

DISSERTATION

TÜBINGEN  
2018



# Precision Calculations for Weakino- Pair Production at Hadron Colliders

DISSERTATION

der Mathematisch-Naturwissenschaftlichen Fakultät  
der Eberhard-Karls Universität Tübingen  
zur Erlangung des Grades eines  
Doktors der Naturwissenschaften  
(Dr. rer. nat.)

vorgelegt von  
**MATTHIAS KESENHEIMER**  
aus Tübingen

TÜBINGEN  
2018

GEDRUCKT MIT DER GENEHMIGUNG DER MATHEMATISCH-NATURWISSENSCHAFTLICHEN  
FAKULTÄT DER EBERHARD-KARLS UNIVERSITÄT TÜBINGEN

TAG DER MÜNDLICHEN QUALIFIKATION: 03.07.2018

DEKAN:

PROF. DR. WOLFGANG ROSENSTIEL

1. BERICHTERSTATTER:

PROF. DR. BARBARA JÄGER

2. BERICHTERSTATTER:

APL. PROF. DR. THOMAS GUTSCHE





# Abstract

A matter of particular interest after the discovery of the Higgs boson is the search for supersymmetric particles which could give answers to several important questions in particle physics. Essential for the search for these hypothetical particles at the Large Hadron Collider (LHC) are calculations of observables with the highest possible precision. To this end, higher-order corrections in the strong interaction and the resummation of logarithmically enhanced contributions via parton-shower simulations have to be considered.

The signatures of supersymmetric particles in detectors are significantly affected by hard jets in the final state which originate from the radiation of hard gluons and quarks. It is thus necessary to include them in higher-order calculations. The central concern of this thesis is an extensive phenomenological study of pair-production processes in the Minimal Supersymmetric Standard Model (MSSM) taking into account the radiation of hard jets. For that purpose, we calculate matrix elements at the next-to-leading order (NLO) in the strong coupling for electroweakino-pair production processes without and with a hard jet in the final state. To further refine the precision of experimentally accessible observables, the matrix elements of the hard scattering process are matched to a parton-shower Monte Carlo program via the POWHEG formalism.

During the implementation of the processes we do not use any simplification with regard to masses or resonance effects. The complete NLO-QCD calculation includes complicated resonance structures in the real corrections which we regularize by a suitable subtraction method. To obtain well-defined matrix elements, we use the so-called PROSPINO subtraction scheme for singly resonant real-emission matrix elements. For diagrams that are doubly resonant an extended version of this method is being used. This subtraction method is the first to be applicable to processes with three final-state particles at tree level.

Additionally, by using the POWHEG-BOX we are able to generate arbitrary NLO distributions corrected by parton-shower effects. With the help of usual phase-space cuts we investigate the influence of the corrections to observables in experimental analyses. Typical and important observables are mono-jet distributions and distributions of missing transverse energy. These observables are notably vital for the search of neutral supersymmetric particles which could be the candidates for the long-sought dark matter.





# Zusammenfassung

Von besonderem Interesse ist nach der Entdeckung des Higgs-Bosons die Suche nach supersymmetrischen Teilchen, die Antworten auf offene Fragen der Teilchenphysik liefern können. Unerlässlich für die Suche nach diesen hypothetischen Teilchen am Large Hadron Collider (LHC) sind Berechnungen von Observablen mit höchster Präzision. Dazu ist es insbesondere nötig, Korrekturen höherer Ordnung bezüglich der starken Wechselwirkung zu berechnen und die Resummation logarithmisch verstärkter Beiträge durch Partonschauerimulationen durchzuführen.

Die Signaturen von supersymmetrischen Signalen im Detektor werden maßgeblich durch harte Jets im Endzustand, die aus der Abstrahlung farbgeladener Teilchen entstehen, verändert und müssen daher in die Rechnung einbezogen werden. Zentrales Anliegen dieser Dissertation ist eine umfassende phänomenologische Studie von Paarproduktionsprozessen im Minimalen Supersymmetrischen Standardmodell (MSSM) unter Berücksichtigung von Jetabstrahlung. Dazu berechnen wir die Matrixelemente für Elektroweakino-Paarproduktionsprozesse mit und ohne einem harten Jet in nächstführender Ordnung (NLO) in der starken Kopplung und binden diese in ein Partonschauerprogramm ein. Wichtigstes Hilfsmittel, um die Matrixelemente der harten Streuung mit einem Partonschauerprogramm zu verknüpfen, ist dabei der POWHEG-Formalismus.

Bei der Implementierung der Prozesse benutzen wir keine Vereinfachungen in Hinblick auf Massen oder Resonanzeffekte. Die vollständige NLO-QCD-Rechnung beinhaltet komplizierte Resonanzstrukturen in den reellen Korrekturen, die wir durch einen geeigneten Ansatz regularisieren. Um wohldefinierte Matrixelemente zu erhalten, benutzen wir für einfach resonante reelle Matrixelemente das sogenannte PROSPINO-Subtraktionsschema. Für Diagramme, die doppelte Resonanzen enthalten, benutzen wir eine erweiterte Subtraktionsmethode. Diese Subtraktionsmethode ist neuartig für Prozesse mit drei Teilchen im Endzustand auf Born-Niveau.

Wir sind in der Lage durch das Verwenden der POWHEG-BOX beliebige NLO-Verteilungen mit Partonschauereffekten zu generieren. Anhand experimentell üblicher Phasenraumschnitte untersuchen wir den Einfluss der Korrekturen auf wichtige Observablen, wie Monojet-Verteilungen und Verteilungen für die fehlende transversale Energie, in experimentellen Analysen. Diese Observablen sind wesentlich für die Suche nach supersymmetrischen Teilchen, die als Kandidaten für dunkle Materie in Frage kommen.



# List of Publications

1. J. Baglio, B. Jäger and M. Kesenheimer, *Precise predictions for electroweakino-pair production in association with a jet at the LHC*, *JHEP* **07** (2018) 055
2. J. Baglio, B. Jäger and M. Kesenheimer, *Electroweakino pair production at the LHC: NLO SUSY-QCD corrections and parton-shower effects*, *JHEP* **07** (2016) 083



# Contents

|          |  |           |
|----------|--|-----------|
| <b>1</b> | <b>Basic concepts</b>                                    | <b>3</b>  |
| 1.1      | Particle physics and quantum field theory . . . . .      | 3         |
| 1.2      | The Standard Model . . . . .                             | 4         |
| 1.3      | Problems of the Standard Model . . . . .                 | 8         |
| 1.3.1    | The Higgs naturalness problem . . . . .                  | 8         |
| 1.4      | Supersymmetry . . . . .                                  | 10        |
| 1.4.1    | SUSY algebra . . . . .                                   | 10        |
| 1.4.2    | The Minimal Supersymmetric extension of the SM . . . . . | 12        |
| 1.4.3    | The SUSY Lagrangian . . . . .                            | 15        |
| 1.4.4    | Soft breaking of SUSY . . . . .                          | 17        |
| 1.4.5    | $R$ -parity . . . . .                                    | 20        |
| 1.5      | Constrained models and experimental status . . . . .     | 21        |
| <b>2</b> | <b>Theoretical background</b>                            | <b>27</b> |
| 2.1      | Calculating observables in QFT . . . . .                 | 27        |
| 2.1.1    | The running of the strong coupling constant . . . . .    | 27        |
| 2.1.2    | Perturbative QFT . . . . .                               | 30        |
| 2.1.3    | Non-perturbative QFT . . . . .                           | 32        |
| 2.2      | Ingredients of an NLO calculation . . . . .              | 35        |
| 2.2.1    | Phase space . . . . .                                    | 37        |
| 2.2.2    | Regularization and renormalization . . . . .             | 39        |
| 2.2.3    | Renormalization constants . . . . .                      | 41        |
| 2.2.4    | On-shell scheme . . . . .                                | 44        |
| 2.2.5    | The $\overline{\text{MS}}$ -scheme . . . . .             | 46        |
| 2.2.6    | SUSY restoring counterterm . . . . .                     | 47        |
| 2.2.7    | Complex mass scheme and renormalization . . . . .        | 48        |
| 2.3      | Infrared divergences . . . . .                           | 49        |
| 2.3.1    | Jets and infrared safety . . . . .                       | 51        |

|          |  |            |
|----------|--|------------|
| 2.3.2    | The FKS subtraction method . . . . .   | 53         |
| 2.4      | Resummation and parton showers . . . . .                                     | 55         |
| 2.5      | Combining NLO corrections with PS . . . . .                                  | 59         |
| 2.5.1    | The POWHEG-BOX . . . . .   | 61         |
| 2.5.2    | Parallelization of the POWHEG-BOX . . . . .                                  | 61         |
| <b>3</b> | <b>Weakino-pair and weakino-pair plus jet production at hadron colliders</b> | <b>63</b>  |
| 3.1      | On-shell resonances - overview . . . . .                                     | 64         |
| 3.1.1    | Subtraction of on-shell resonances . . . . .                                 | 66         |
| 3.1.2    | Breit-Wigner factor . . . . .  | 69         |
| 3.1.3    | Off-to-on-shell momentum reshuffling . . . . .                               | 71         |
| 3.1.4    | Jacobian correction factor . . . . .   | 74         |
| 3.1.5    | Putting it all together . . . . .  | 76         |
| 3.2      | Weakino-pair production . . . . .  | 77         |
| 3.2.1    | Born and virtual corrections . . . . .                                       | 77         |
| 3.2.2    | Real corrections . . . . .   | 80         |
| 3.2.3    | On-Shell resonances . . . . .  | 81         |
| 3.2.4    | Numerical checks . . . . .   | 82         |
| 3.2.5    | Phenomenological setup and results . . . . .                                 | 83         |
| 3.3      | Weakino-pair plus jet production . . . . .                                   | 92         |
| 3.3.1    | Born and virtual corrections . . . . .                                       | 92         |
| 3.3.2    | Additional renormalization constants . . . . .                               | 95         |
| 3.3.3    | Real corrections . . . . .   | 99         |
| 3.3.4    | On-shell resonances . . . . .  | 100        |
| 3.3.5    | Numerical checks . . . . .   | 103        |
| 3.3.6    | Phenomenological setup and results . . . . .                                 | 104        |
| 3.3.7    | Choice of the spectrum and input parameters . . . . .                        | 104        |
| 3.3.8    | Cross sections and distributions at the LHC . . . . .                        | 105        |
| <b>4</b> | <b>Conclusion and outlook</b>  | <b>111</b> |
|          | <b>Appendices</b>  | <b>115</b> |
| A        | Compiling and initializing the code . . . . .                                | 117        |
| A.1      | Preface . . . . .  | 117        |
| A.2      | Dependencies . . . . .   | 117        |
| A.3      | Compiling . . . . .  | 118        |
| A.4      | Preprocessor flags . . . . .   | 119        |

|     |  |     |
|-----|--|-----|
| A.5 | Running and cleaning . . . . .                                       | 120 |
| B   | Input parameters for the weakino and weakino-jet executables . . . . | 123 |
| C   | The runparallel.sh script . . . . .                                  | 129 |
| D   | Fortran routines for the parametrization of phase spaces . . . . .   | 135 |
| E   | Selecting doubly on-shell resonant diagrams with FEYNARTS . . . .    | 141 |





# Introduction

Our world and the universe give us a huge and mysterious playground to investigate. For the last hundred years physics has developed from classical Newtonian mechanics to an incredibly deep field of interest which, with new types of funding and industrial interests, has become accessible for many new researchers all over the world. With more and more people dedicating their time to reveal the mysteries of nature, with better ways to communicate and publicly accessible publication platforms, physics has made a big leap forward. These advances have been especially noticeable in modern particle physics which describes the interactions of fundamental particles.

Understanding the matter which surrounds us on a fundamental level has helped physicists to uncover puzzling questions and to gain knowledge about our universe in general. However, particle physics has a lot more applications in our daily life than one might think at first sight. In medicine, new therapies of cancer treatment involve the irradiation of the cancerous tissue by high-energetic proton beams. This method is less harmful for the surrounding healthy tissue than gamma ray therapy. Furthermore, Magnetic Resonance Imaging (MRI) only became economical by producing superconducting magnets with industrial processes required also for magnets used in particle accelerators. Additionally, experiments at hadron colliders produce vast quantities of data which have to be stored, transmitted and edited rapidly. To easily exchange and share the experimental data, the World Wide Web was invented in 1989. The technologies used by particle physicists to handle this amount of data show benefits in computer and communication science. Besides the many positive secondary effects on industry, medicine, and other areas, particle physics widens our understanding and deepens the knowledge of mankind.

One question particle physicists want to have an answer for is, for example, if supersymmetry is realized in nature. In short, supersymmetry is a novel symmetry relation between bosonic and fermionic particles which would have remarkable physical consequences. In this thesis we will focus on the determination of theoretical predictions for pair-production processes which are postulated in the minimal supersymmetric extensions of the Standard Model. Although the Standard Model (SM) describes the interaction of subatomic particles at high-energetic collision experiments with unprecedented precision, there are still flaws in the framework of the SM. Parts of these deficiencies, that will be discussed later, can be addressed by supersymmetric extensions. How the theory that describes nature best turns out to be in the end, remains to be seen. However, precision calculations can pave the way

## *Introduction*

to understand the physics of high-energy collisions better. Therefore, the results of this work may be helpful to find evidence if supersymmetry is realized or not.

This thesis is organized as follows. In Chap. 1 we discuss the basic concepts needed to understand how the Standard Model of particle physics is built up. Furthermore, we introduce the concept of supersymmetry and how supersymmetry can complement the SM. We continue in Chap. 2 with discussing the technical details of precision calculations and the tools that are necessary to get phenomenological results within the framework of quantum field theory. Ways of how to improve these results are considered, too. Finally, in Chap. 3 we present the subtleties of our calculations and show the phenomenological results of weakino-pair and weakino-pair plus jet production. The conclusion is given in Chap. 4.

# 1 Basic concepts

## 1.1 Particle physics and quantum field theory

Quantum field theory (QFT) is the mathematical framework which is used to model the properties of nature on a fundamental level. QFT combines the principles of classical field theory, quantum mechanics and special relativity. The unification of quantum mechanics and special relativity is based on two essential requirements. In particular, these are commutator relations between operators and the invariance of the equations of motion under Lorentz transformations. Furthermore, the number of particles is not fixed as in the case of classical quantum mechanics. Describing the systems with state vectors in the infinite Hilbert space is thus not only complicated but also very impracticable. Hence, the formalism to describe fundamental particle interactions relies on the more common field object.

Already in the early 19th century, the concept of fields proved to be a useful tool to describe the properties of light and gravity. In particle physics different types of fields have to be distinguished. Fields with different transformation properties under Lorentz transformations represent particles of different spin. For instance, scalar, vector and tensor fields have to be used to describe the properties of bosons with integer spin, whereas fermions with half-integer spin have to be treated as Dirac fields, the so-called spinors. Within the framework of QFT, particles are seen as excitations of these fields. Furthermore, the vacuum, which has in general a highly non-trivial complexity, is the state of lowest energy of all given fields. By considering only the dynamics of fields instead of the dynamics of a single particle state, the number of particles is not fixed a priori. Therefore, describing multi-particle interactions in which particles can be annihilated and created, is much simpler.

## Introduction

In perturbative QFT (c.f. Sec. 2.1.2), interactions between charged<sup>1</sup> particles are modeled by a particle exchange. Since these exchanged particles can not be detected directly, they are called virtual particles. Due to their fleeting appearance, virtual particles can be *off* their mass shell, which means that they do not satisfy the on-shell relation  $p^2 = m^2$ , where  $p$  is the momentum and  $m$  the mass of the particle. Additionally, interactions within most QFTs are local<sup>2</sup>, meaning that the space-time interval separating them is null. This demand for locality is deeply related to causality. If we would allow space-like separated interactions in a Lorentz invariant theory, we would also have to allow time-like separated interactions. This would imply that a state in the future could interact with a state in the past.

In the next section we want to introduce the Standard Model (SM) of particle physics and briefly discuss the problems of the SM that currently exist.

## 1.2 The Standard Model

Uniting the electromagnetic, weak and strong interaction in a consistent theoretical framework, the SM of particle physics is one of the most successful and precisely measured models in modern physics. Quantum electrodynamics (QED) describes the interaction of (electrically) charged particles with light, whereas the weak interaction is the fundamental theory of particle interactions that cause radioactive decay. The weak interaction and QED were unified in 1971 by Glashow, Weinberg and Salam to the electroweak theory [2–4]. Although the electromagnetic and weak force behave differently at low energies, the phenomena of both forces are modeled collectively by the electroweak theory at high energies. The strong force plays an important role for nuclear interactions and is responsible for the generation of hadrons, such as neutrons, protons or pions. The theory of strong interactions is represented by quantum chromodynamics (QCD) [5, 6].

Within the framework of the SM all matter consists of point-like elementary particles with fermionic character. As we know today, these fundamental matter particles are the quarks and leptons. Quarks and leptons are divided into three generations which differ only in the masses of the respective particles. Additionally, for every fermion an antiparticle with opposite charge exists in the SM.

---

<sup>1</sup>Charges are a general concept of QFT and refer not only to the electric charge. We will see in Sections 1.2 and 1.4.2 that charges emerge as properties of a specific gauge group.

<sup>2</sup>For an example of a non-local effective field theory describing the bound state of two mesons see Ref. [1] and references therein.

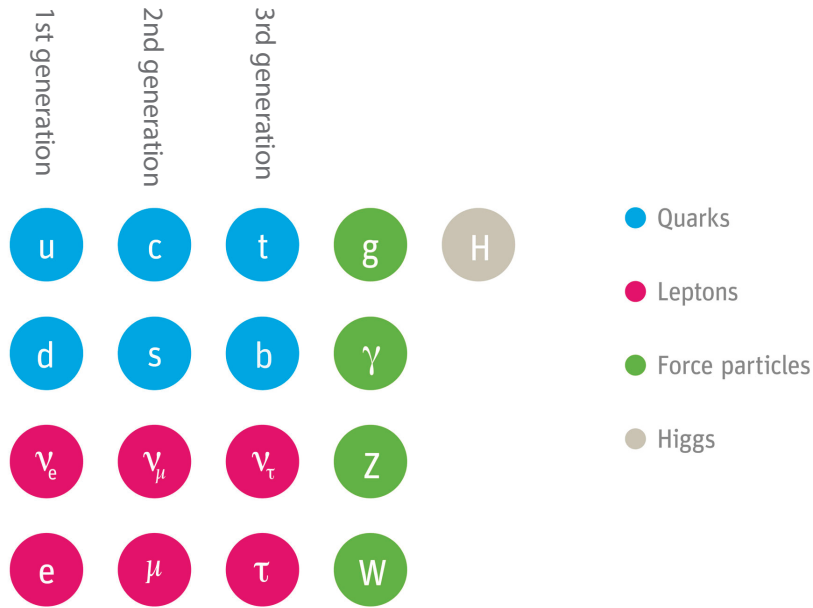


Figure 1.1: The elementary particle content of the SM. The (fermionic) matter particles are divided into three generations, sorted by the mass of the particles. Depicted in green are the gauge bosons which are responsible for the interactions between the particles. The Higgs boson generates the masses of the particles. Picture according to [7].

Interactions between the matter particles of the SM are constructed by exploiting miscellaneous internal and external symmetries. External symmetries, or the symmetries of space-time transformations, are described by the Poincaré group which generalizes four-dimensional transformations in Minkowski space by Lorentz rotations, Lorentz boosts and four-dimensional translations. All fields of the SM Lagrangian belong to a specific representation of the Poincaré group which determines their spin. Particles of one Poincaré multiplet should have the same mass, although this symmetry is broken in nature. This symmetry breaking is induced by the Higgs mechanism as we will discuss below.

Furthermore, the fields of the SM Lagrangian underlie internal symmetries, the gauge symmetries, that determine how the particles can interact among each other. These gauge symmetries are local in the SM, meaning that the quantum numbers are conserved at each local interaction point. The three Lie groups that describe the gauge symmetries of the SM are the color group  $SU(3)_C$ , the weak

## Introduction

isospin group of left-handed particles  $SU(2)_L$ , and the symmetry group of the weak hypercharge  $U(1)_Y$ . These symmetry groups define transformations between the fields under which the Lagrangian is invariant. The strength of processes of the SM is measured in terms of fundamental coupling constants. Electroweak processes depend on the fine structure constant  $\alpha = e^2/4\pi$ , where  $e$  is the electric charge, while QCD processes depend on the strong coupling constant  $\alpha_s = g_s^2/4\pi$ ,  $g_s$  being the strong charge.

Gauge bosons, the particles which are responsible for the interactions between the matter fields, always transform under the adjoint representation of the respective group, while the fermionic matter fields are described by the fundamental (if charged under the specific gauge group) or by the trivial (if uncharged) representation. In detail, the particles of the SM and their properties under the respective gauge groups are as follows.

All quarks are charged under the strong interaction, meaning that they are in the fundamental representation with regard to  $SU(3)_C$ . The up  $u$ , charm  $c$  and the top quark  $t$  carry  $+2/3e$  electrical charge, while the down  $d$ , strange  $s$  and the bottom quark  $b$  carry the charge  $-1/3e$ . The leptonic sector consists of the electron  $e$ , muon  $\mu$  and the tau lepton  $\tau$  with integer charge  $-1e$ . Particles with no electric charge are the electron neutrino  $\nu_e$ , the muon neutrino  $\nu_\mu$  and the tau neutrino  $\nu_\tau$ . What is more, the left-handed components of all fermionic fields (later indicated by a subscript  $L$ ) are in the fundamental representation of  $SU(2)_L$ , whereas the right-handed components (indicated by a subscript  $R$ ) are in the trivial representation. The electroweak force is transmitted by the massless  $B$  and  $W$  bosons, where  $B$  is in the adjoint representation of  $U(1)_Y$  and the three  $W = (W_1, W_2, W_3)$  bosons are in the adjoint representation of  $SU(2)_L$ . After symmetry breaking, the  $B$  and  $W_3$  bosons form the photon field  $\gamma$  and the massive  $Z$  boson, while the massive  $W^\pm$  bosons are generated dynamically as a mixture of  $W_1$  and  $W_2$ . The transmitters of the strong interaction are the gluons  $g$  which are in the adjoint representation with regard to  $SU(3)_C$  and in the trivial representation of  $SU(2)_L$ . In particular, since the gluon fields are in the adjoint representation of  $SU(3)_C$  there are in total  $N^2 - 1 = 8$  different gluon fields in the SM, where  $N = 3$  is the dimension of the color gauge group. Figure 1.1 shows the particle content of the SM.

The existence of mass terms for the weak gauge bosons  $Z$  and  $W^\pm$  are explained by the Englert-Brout-Higgs-Guralnik-Hagen-Kibble mechanism<sup>3</sup> [8–10]. Furthermore, the EBHGHK mechanism prevents the weak gauge bosons from having unphysical

---

<sup>3</sup>We use the abbreviation EBHGHK mechanism or simply Higgs mechanism in the following.

interactions at high energies [11, 12] which is the requirement for unitarity. Introducing mass terms for gauge bosons by hand would break the gauge invariance of the Lagrangian. The simplest way to keep the  $SU(2)_L \times U(1)_Y$  gauge symmetry of the Lagrangian and to maintain unitarity of all interactions at high energies, is to break the symmetry spontaneously below a certain energy scale. In particular, this means the SM Lagrangian is still symmetric under  $SU(2)_L \times U(1)_Y$  transformations, although the vacuum realized by the theory is not. Hence, the symmetry  $SU(2)_L \times U(1)_Y$  is broken by the vacuum. However, an exact symmetry  $U(1)_{EM}$ , which is the gauge algebra of the electromagnetic interactions, remains. The energy scale where the symmetry breaking occurs is of order of the electroweak scale ( $\approx 250$  GeV). At energies lower than the weak scale, the symmetry is spontaneously broken by the EBHGHK mechanism and the gauge bosons obtain mass by absorbing the degrees of freedom of the Nambu-Goldstone bosons that occur after the spontaneous symmetry breaking [13–15]. At energies higher than the weak scale, the weak gauge bosons behave as if they were massless. The gauge symmetry cancels the longitudinal polarization of the weak gauge bosons which prevents unphysical interactions to take place. In detail, the interaction of a longitudinally polarized vector boson is equivalent to the interaction of a corresponding Nambu-Goldstone boson at high energies. This is known as the Goldstone boson equivalence theorem (GBET), see Ref. [12, 16]. As it turns out, the contribution of this Nambu-Goldstone boson is equal and opposite to the Higgs contribution. Thus, the problematic contributions cancel and unitarity is preserved at high energies.

The most obvious implication of the Higgs mechanism is the appearance of a  $CP$ -even Higgs boson with spin 0 which remains as one scalar degree of freedom after the symmetry breaking. In 2012, the Higgs boson was finally found by the ATLAS [17] and the CMS [18] experiments and the mass was measured by both collaborations to be around 125 GeV. Furthermore, the couplings to SM particles are consistent with the prediction of a SM-like Higgs boson [19], but still leave room for alternative models such as the supersymmetric extension to the SM.

## 1.3 Problems of the Standard Model

In contrast to its remarkable accuracy the SM was tested for, there are many fundamental questions left unanswered. The observation of neutrino oscillations<sup>4</sup> [20–23] represents a first experimental deviation. Two of the most severe imperfections that unveil additional limitations of the SM are the Higgs naturalness problem, which we will briefly discuss in the subsequent section, and the unsolved origin of dark energy and dark matter. The latter, supported by experimental observations of the bullet cluster [24, 25] and by galaxy rotation curves (c.f. Ref. [26] and references therein), is a strong indication that there are more fundamental particles in nature which are not covered by the SM.

Having imperfections in a model is nothing new. For many years simple approaches like the V-A-current-current (Fermi) theory worked very well for calculations in lowest order of the perturbation theory. With the perturbation theory breaking down completely at the weak scale, which was unknown at that time, problems arose as the first higher order corrections were tried to be made. Being a purely theoretical problem in these years, the non-renormalizability of the Fermi theory sparked the interest of Glashow, Salam and Weinberg, which developed in 1971 the solution to the problems of the Fermi theory. It is plausible that concentrating nowadays on the imperfections of the SM can pay off, too.

### 1.3.1 The Higgs naturalness problem

Since the SM is a renormalizable theory, finite results are obtained for virtual loop corrections even if the loop momentum approaches infinity. Although this means that the SM is by its own well defined and could in principle make predictions up to infinite energies, the imperfections make us believe that the SM is effectively part of a larger theory. This means that predictions of the SM are only correct up to a certain scale. Hence, integrals of quantum loop corrections need not to be evaluated to arbitrary high momenta, but only up to a certain energy scale, where new physics occurs. By introducing a new energy scale to the SM by means of a cut-off in loop integrals, it turns out that the four-boson loop correction to the Higgs mass is of

---

<sup>4</sup>From the experimentally proven neutrino oscillations we know that at least two neutrinos must have mass. Since mass terms for neutrinos would require a right-handed spinor component, neutrino masses can not be explained in the SM. The SM does not introduce right-handed neutrinos in its original conception since right-handed neutrinos are singlets with regard to the weak interaction and were not observed yet.



order of the cut-off squared. The dependence of the Higgs mass on a quadratic divergence leads to the Higgs mass fine tuning problem. In order to have a light Higgs boson, the parameters of the Higgs potential have to be determined very precisely depending on the cut-off which is unnatural. For this reason, the Higgs fine tuning problem is sometimes referred to as the Higgs naturalness problem. For more details on the Higgs naturalness problem see Refs. [27, 28].

The Higgs naturalness problem is a special property of the scalar nature of the Higgs field and it does, for instance, not occur in loop corrections to fermionic fields. Indeed, the chiral symmetry ensures that corrections to the fermion mass are always proportional to the mass itself ( $\delta m \propto m$ ). If the mass of the fermion is small, the correction to the mass is small, too, and no fine-tuning problem occurs. Furthermore, as the mass of the fermion goes to zero the chiral symmetry is restored.

For the Higgs field there is no such symmetry as the chiral symmetry which could prevent quadratic divergences. Therefore, the mass of the Higgs boson is not prevented from getting unphysically large. However, supersymmetry (SUSY) could stabilize the mass of the Higgs boson in the sense that SUSY introduces a symmetry relation between bosons and fermions. If SUSY was a true symmetry of nature, additional fermionic particles would enter the virtual loop corrections to the Higgs mass. These loop corrections would have the same cut-off dependency with a different sign which would lead to a cancellation of the quadratic cut-off terms. In order to have an exact cancellation, the mass of the introduced fermionic partner particle and the mass of the Higgs boson should degenerate or should be at least of the same order. Even if the symmetry is not exact and the cancellation of the fermionic and bosonic degrees of freedom in the loop-correction is not perfect, only logarithmic terms depending on the cut-off are left, which is unproblematic.

Although there are many other models to address the Higgs naturalness problem (technicolor [29], preon models [30, 31], top quark condensate [32], etc.), the most appealing one is the supersymmetric extension of the SM. The alternative models all have in common that the Higgs boson is a composite particle of new fundamental particles. However, these models are very constrained and fermion masses are difficult to describe with these models.

## 1.4 Supersymmetry

Supersymmetric models, from a theoretical viewpoint very compelling by themselves, provide an elegant way to solve parts of the problems of the SM. The most obvious predictions of supersymmetric models are additional fundamental particles which differ from their SM counterparts only by half a unit in spin. Among the many new particles which are introduced, the most attractive property of SUSY is that dark matter can be explained. As we have seen in the previous section, SUSY can cure the hierarchy problem of the SM. Additionally, SUSY helps in the unification of the fundamental forces at a higher scale which is necessary for theories with the goal of describing all forces as manifestations of one single, all-encompassing force (grand unified theories, GUT [33, 34]). In the SM the gauge couplings (electromagnetic, weak and strong couplings) do not meet at a certain scale, in SUSY however they do. On the way to the theory of everything, which unifies the non-gravitational forces with gravity, the most promising models incorporate SUSY in a natural way. Even the unsolved mystery of dark energy has been tried to be explained by SUSY, see Ref. [35–37]. Besides all that, SUSY is the largest space-time symmetry that could possibly be realized in nature. If SUSY is considered as a local gauge theory, general relativity is included automatically in a theory called supergravity [38].

These are many reasons, why SUSY is so attractive and why it is good to get a better understanding of SUSY. The following section will be dedicated to the basic theoretical details of SUSY. We will discuss the minimal supersymmetric extension of the SM, the particle spectrum and the soft breaking of SUSY.

### 1.4.1 SUSY algebra

An important step towards the SUSY algebra was the Coleman-Mandula theorem [39]. It states that every Lie-algebra that encompasses the Poincaré and an internal symmetry group, can only be a direct product of these two groups. This means that every space-time symmetry can only be trivially combined with an internal symmetry. As a result of this theorem, no other tensorial symmetries can occur other than those which are already part of the Poincaré group. More specifically, no other symmetry operators besides the four-momentum operator  $P_\mu$ , which is the generator of space-time translations, and the angular momentum operator  $M_{\mu\nu}$ , being the generator of homogeneous Lorentz transformations, exist.

However, as was found later by Haag, Łopuszański and Sohnius [40] the Coleman-

Mandula theorem did not exclude charges that transform as spinors under Lorentz transformations. Such charges, denoted by  $Q_a$  ( $a = \{1, 2\}$ ), are mathematically two component Weyl-spinors which have anti-commutation relations among themselves. These anti-commutation relations define the Poincaré super algebra which is the building block of every supersymmetric extension of the Standard Model.

Basically, the operator  $Q$  is used to define the transformation from a bosonic into a fermionic state and vice versa:

$$Q_a |J\rangle = |J \pm 1/2\rangle, \quad (1.1)$$

where  $J$  is the spin of the particle. To get the commutator and anti-commutator relations among the generators  $Q$  we start at the observation that, since  $Q$  is a symmetry operator,  $Q$  commutes with the Hamiltonian  $H$ ,

$$[Q_a, H] = 0. \quad (1.2)$$

Equivalently, any combination of the operator  $Q$  commutes with the Hamiltonian  $H$ , too, meaning

$$\left[ \{Q_a, Q_b^\dagger\}, H \right] = 0. \quad (1.3)$$

The symmetric object  $\{Q_a, Q_b\} = Q_a Q_b + Q_b Q_a$  ( $a, b = \{1, 2\}$ ) transforms like a spin-1 object. As we know from the Coleman-Mandula theorem, the only conserved vector in a relativistic theory which satisfies Eq. (1.3) is the four-momentum generator  $P_\mu$ . It turns out by further examination [27] that the anti-commutator of  $Q$  and  $Q^\dagger$  can be linked to this generator by

$$\{Q_a, Q_b^\dagger\} = (\sigma^\mu)_{ab} P_\mu. \quad (1.4)$$

Additionally, the symmetry generator  $Q$  has to satisfy the following commuting and anti-commuting relations [27]

$$\{Q_a, Q_b\} = \{Q_a^\dagger, Q_b^\dagger\} = 0, \quad (1.5)$$

$$[Q_a, P_\mu] = [Q_a^\dagger, P_\mu] = 0, \quad (1.6)$$

$$[M^{\mu\nu}, Q_a] = -i\sigma_{ab}^{\mu\nu} Q_b, \quad (1.7)$$

where  $\sigma^\mu = (\mathbf{1}, \sigma_i)$ ,  $\bar{\sigma}^\mu = (\mathbf{1}, -\sigma_i)$ ,  $\sigma_i$  ( $i = 1, 2, 3$ ) are the usual Pauli matrices and  $\sigma^{\mu\nu} = \frac{i}{4}(\sigma^\mu \bar{\sigma}^\nu - \sigma^\nu \bar{\sigma}^\mu)$ . The angular momentum operator  $M_{\mu\nu}$  together with the four-momentum generator  $P_\mu$  defines the Poincaré algebra

$$[M^{\mu\nu}, P^\rho] = g^{\mu\rho} P^\nu - g^{\nu\rho} P^\mu. \quad (1.8)$$

Equation (1.4) gives an interesting insight into SUSY, too. If two SUSY generators  $Q$  operate on a physical state, the four-momentum vector  $P_\mu$  or, in other words, a derivative is generated. As the Dirac equation being effectively the square root of the Klein-Gordon equation, the SUSY algebra can be viewed as the generalization of the Dirac equation by providing the square root of a derivative.

As we mentioned earlier and as one might intuitively see from Eq. (1.4), if SUSY is considered as a local gauge symmetry and not only as a global symmetry, general relativity is included automatically. According to Ref. [38], local SUSY can be seen as the square root of general relativity. This relies on the fact that Eq. (1.4) connects two SUSY generators  $Q_i$  with the four-momentum vector  $P_\mu$ . Since  $P_\mu$  is the generator of the Poincaré group, local SUSY implies general relativity.

### 1.4.2 The Minimal Supersymmetric extension of the SM

Similar to the symmetry groups of the SM (c.f. Sec. 1.2), the SUSY algebra of Eq. (1.4) assigns every particle to a supermultiplet, or accordingly, supermultiplets are representations of the SUSY algebra. Effectively, the particle content of the SM is doubled which leads to the Minimal Supersymmetric extension of the Standard Model (MSSM). Particles of one supermultiplet have the same quantum numbers and mass (the generator  $Q$  commutes with the Hamiltonian  $H$ , or similarly, with  $P^\mu$  and  $P^2 = M^2$ , where  $M$  is the particle mass), but differ in their spin by  $1/2$ .

The simplest supermultiplet can be built by a (massive) spin-1/2 Weyl fermion with two (fermionic) degrees of freedom, and a complex scalar field with two (bosonic) degrees of freedom. This supermultiplet is called the chiral supermultiplet and an example of physical relevance is the  $SU(2)_L$  doublet with spin  $1/2$  partnered with another  $SU(2)_L$  doublet with spin  $0$ , i.e.

$$\begin{pmatrix} \nu_{eL} \\ e_L \end{pmatrix} \leftrightarrow \begin{pmatrix} \tilde{\nu}_{eL} \\ \tilde{e}_L \end{pmatrix}, \quad (1.9)$$

where  $\nu_{eL}$  is the left-handed component of the electron-neutrino field,  $e_L$  is the left-handed component of the electron field,  $\tilde{\nu}_{eL}$  is the electron-sneutrino and  $\tilde{e}_L$  is the selectron. Right-handed leptons transform as a  $SU(2)_L$  singlet, therefore, no right-handed neutrino exists in the SM (and in the MSSM) and the right-handed component of the electron spinor  $e_R$  is partnered with the complex spin-0 field  $\tilde{e}_R$ . Note that the helicity indices  $L$  and  $R$  of the spin-0 particles refer to the helicity

of their superpartners which does not imply that the spin-0 particles are helicity eigenstates.

In a similar way, every other spin-1/2 fermion of the SM is assigned to a complex spin-0 field. More specifically, the quark fields transforming under the  $SU(3)_C$  group as triplets and under the  $SU(2)_L$  group as doublets or singlets, are partnered with spin-0 fields named *squarks*. In general, the superpartners of the SM matter fields are denoted by a tilde above their field symbols. Furthermore, to assemble the name of the spin-0 SUSY particles an additional *s* is put in front of the name of the SM particle.

Gauge multiplets are formed by associating the (massless) spin-1 bosons with their SUSY counterparts. A massless spin-1 particle can have two (transversal) polarizations. Therefore, every massless gauge boson is partnered with a massless spin-1/2 fermion which is described by a Weyl-spinor with two fermionic degrees of freedom. Superpartners to gauge bosons are generically called *gauginos*. An example are the gluon fields that transform as octets under  $SU(3)_C$  which are partnered with gluinos:

$$g \leftrightarrow \tilde{g}. \quad (1.10)$$

Since gluons transform under the self-conjugate adjoint representation of the  $SU(3)_C$  group, gluinos must have the same transformation properties. In particular, the left and right-handed components of the gluinos need to have the same gauge transformation properties, which implies that gluinos are Majorana fermions.

The only particle left which needs pairing with a superpartner, is the Higgs boson. The Higgs field of the SM constitutes a weak isospin doublet with weak hypercharge  $Y_W = +1$ . However, the MSSM needs two Higgs doublets to prevent gauge anomalies. Gauge anomalies originate from quantum corrections to multi-vector-boson vertices if a chiral asymmetry exists. Particularly in the SM, these anomalies arise in triangular fermionic loops which are known as Adler-Bardeen-Jackiw anomalies [41], see Fig. 1.2. All quantum-gauge theories should be anomaly free which is indeed the case for the SM. Diagrams of the kind shown in Fig. 1.2 are proportional to  $\text{Tr}(Q^3)$  where  $Q$  are the (charge) generators of the involved gauge symmetries. If the theory should be anomaly free, all of these traces have to be zero. For that purpose, a cancellation between leptons and quarks is necessary which implies that the SM would be incomplete if it would consist of quarks or leptons only. Similar to the requirement that the SM needs both leptons and quarks, it is necessary to have a second Higgs doublet in the MSSM. In the MSSM the superpartners of the Higgs fields give rise to new degrees of freedom in the triangular fermionic loop which do

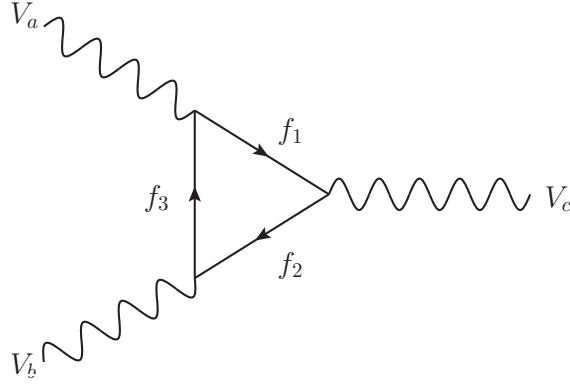


Figure 1.2: Three vector bosons coupling to a triangular fermionic loop. Diagrams of this kind are responsible for Adler-Bardeen-Jackiw anomalies.

not cancel if only one Higgs doublet is considered. Thus, gauge anomalies are introduced. If instead a second Higgs isospin doublet with weak hypercharge  $Y_W = -1$  is demanded, the additional degrees of freedom are canceled and gauge symmetry is preserved again [42]. Additional methods can be applied to prevent gauge anomalies. However, introducing a second Higgs doublet is the simplest approach. The two Higgs doublets of the MSSM are labeled by  $(H_u^+, H_u^0)$  and  $(H_d^0, H_d^-)$ , where the first doublet couples to  $u$ -type quarks and the latter to  $d$ -type quarks only.

Since the Higgs boson is a spin-0 particle, the superpartners must be fermions with spin 1/2. Hence, the Higgs bosons of the MSSM and the superpartners form a chiral supermultiplet. Superpartners of the Higgs bosons are called higgsinos and are labeled by  $(\tilde{H}_u^+, \tilde{H}_u^0)$  and  $(\tilde{H}_d^0, \tilde{H}_d^-)$  for the isospin doublet with hypercharge  $Y_W = 1$  and  $Y_W = -1$ , respectively.

The particle content of the MSSM is summarized in Table 1.1 and Table 1.2. The transformation properties under  $SU(3)_C \times SU(2)_L$  gauge transformations and the weak hypercharge of the particles are given in the last column. The weak hypercharge  $Y_W$  is given by  $Y_W = 2(Q - T_3)$ , where  $Q$  is the electric charge of the particle and  $T_3$  is the third component of the weak isospin.

Note that in supergravity models, which result from local SUSY, at least two additional particles occur in the spectrum: the spin-2 graviton and its associated spin-3/2 particle which is called gravitino. The gravitino is the gauge boson for local SUSY transformations [43].

| Names                               |           | spin 0                            | spin 1/2                         | SU(3) <sub>C</sub> , SU(2) <sub>L</sub> , U(1) <sub>Y</sub> |
|-------------------------------------|-----------|-----------------------------------|----------------------------------|---|
| squarks, quarks<br>(× 3 families)   | q         | $(\tilde{u}_L, \tilde{d}_L)$      | $(u_L, d_L)$                     | <b>3, 2</b> , $+\frac{1}{3}$                                |
|                                     | $\bar{u}$ | $\tilde{u}_R$                     | $u_R^c$                          | <b><math>\bar{3}</math>, 1</b> , $-\frac{4}{3}$             |
|                                     | $\bar{d}$ | $\tilde{d}_R$                     | $d_R^c$                          | <b><math>\bar{3}</math>, 1</b> , $+\frac{2}{3}$             |
| sleptons, leptons<br>(× 3 families) | L         | $(\tilde{\nu}_{eL}, \tilde{e}_L)$ | $(\nu_{eL}, e_L)$                | <b>1, 2</b> , $-1$  |
|                                     | $\bar{e}$ | $\tilde{e}_R$                     | $e_R^c$                          | <b><math>\bar{1}</math>, 1</b> , $2$                        |
| Higgs, Higgsinos                    | $H_u$     | $(H_u^+, H_u^0)$                  | $(\tilde{H}_u^+, \tilde{H}_u^0)$ | <b>1, 2</b> , $+1$  |
|                                     | $H_d$     | $(H_d^0, H_d^-)$                  | $(\tilde{H}_d^0, \tilde{H}_d^-)$ | <b>1, 2</b> , $-1$  |

Table 1.1: The matter fields and their superpartners of the MSSM. Table taken from Ref. [27].

| Names             | spin 1/2                     | spin 1       | SU(3) <sub>C</sub> , SU(2) <sub>L</sub> , U(1) <sub>Y</sub> |
|-------------------|------------------------------|--------------|---|
| gluinos, gluons   | $\tilde{g}$                  | $g$          | <b>8, 1, 0</b>  |
| winos, $W$ bosons | $\tilde{W}^\pm, \tilde{W}^0$ | $W^\pm, W^0$ | <b>1, 3, 0</b>  |
| bino, $B$ boson   | $\tilde{B}$                  | $B$          | <b>1, 1, 0</b>  |

Table 1.2: The gauge fields and their superpartners of the MSSM. Table taken from Ref. [27].

### 1.4.3 The SUSY Lagrangian

We will not go into much detail here since a good introduction how to build supersymmetric Lagrangians can be found elsewhere in the literature, see for instance Refs. [27, 44]. However, we want to briefly sketch the general layout of a supersymmetric Lagrangian. This may give an additional insight into the framework of SUSY, although the following discussion does not raise the claim of completeness.

A general SUSY Lagrangian can be divided into multiple parts:

$$\mathcal{L}_{\text{SUSY}} = \mathcal{L}_{\text{chiral}} + \mathcal{L}_{\text{gauge}} + \mathcal{L}_{\text{soft}}. \quad (1.11)$$

The chiral Lagrangian  $\mathcal{L}_{\text{chiral}}$  describes the kinetic terms of the SM matter particles and their superpartners including the couplings to the gauge bosons.  $\mathcal{L}_{\text{chiral}}$  comprises the Klein-Gordon Lagrangian for spin-0 fields  $\phi^i$  (Higgs, squarks and sleptons) and the Dirac Lagrangian in Weyl representation for (left-handed) spin-1/2 fields  $\psi^i$

## Introduction

(higgsinos, quarks and leptons). Note that the Hermitian conjugate of a left-handed Weyl spinor transforms as a right-handed Weyl spinor and vice versa. Therefore, the Lagrangian can be redefined to contain left-handed fields only. In the following, we choose the names of right-handed Weyl spinors to carry a dagger and the names of left-handed Weyl spinors to carry no dagger.

The potential  $V$  includes mass terms for the scalar particles and the Higgs potential. Masses of fermionic particles are given by  $M^{ij}$ . The Yukawa term (last line of the following equation) describes the interaction between the scalar fields  $\phi^i$  and spinor fields  $\psi^i$  with coupling strength  $y^{ijk}$ .

$$\begin{aligned} \mathcal{L}_{\text{chiral}} = & \nabla^\mu \phi^{*i} \nabla_\mu \phi_i - V(\phi, \phi^*) \\ & + i\psi^{\dagger i} \bar{\sigma}^\mu \nabla_\mu \psi_i - \frac{1}{2} M^{ij} \psi_i \psi_j - \frac{1}{2} M_{ij}^* \psi^{\dagger i} \psi^{\dagger j} \\ & - \frac{1}{2} y^{ijk} \phi_i \psi_j \psi_k - \frac{1}{2} y_{ijk}^* \phi^{*i} \psi^{\dagger j} \psi^{\dagger k}. \end{aligned} \quad (1.12)$$

The indices  $i, j$  and  $k$  run over the appropriate gauge and flavor indices of the bosons and fermions.

For the gauge part we have

$$\mathcal{L}_{\text{gauge}} = -\frac{1}{4} F_{\mu\nu}^a F^{\mu\nu,a} + i\lambda^{\dagger a} \bar{\sigma}^\mu \nabla_\mu \lambda^a + \frac{1}{2} D^a D^a, \quad (1.13)$$

where  $F_{\mu\nu}^a = \partial_\mu A_\nu^a - \partial_\nu A_\mu^a + g f^{abc} A_\mu^b A_\nu^c$  is the Yang-Mills strength with the gauge coupling  $g$ . The factor  $f^{abc}$  is the antisymmetric structure constant of the respective gauge group representations of the fields  $A_\mu^a$ . The kinetic part of the gauge fields  $A_\mu^a$  (gluons,  $B$  and  $W$  bosons) is encoded in the first term, whereas the gauginos  $\lambda^a$  (gluinos, binos and winos) are described by the second term. The indices  $a, b$  and  $c$  are the gauge indices of the respective group.

The auxiliary term  $1/2 D^a D^a$  is added to close the SUSY algebra for off-shell fields, meaning that these auxiliary fields cancel the mismatch between the bosonic and fermionic degrees of freedom in the off-shell case. Note, that usually auxiliary fields are also present in  $\mathcal{L}_{\text{chiral}}$ . However, they can be expressed in terms of scalar fields and are therefore already included in  $\mathcal{L}_{\text{chiral}}$ . The auxiliary fields can be eliminated at the classical level through the corresponding equations of motion.

Interactions between the gauge and the chiral sector are introduced by gauging the chiral Lagrangian with the covariant derivative  $\nabla_\mu = \partial_\mu - ig A_\mu^a T^a$ . The coupling strength  $g$  can either be the electric charge  $e$  or the strong coupling strength  $g_s$ , depending on the representation of the chiral fields with respect to the gauge group. The generators  $T^a$ , which satisfy  $[T^a, T^b] = f^{abc} T^c$ , determine the transformation



properties of the fields under general  $SU(N)$  group transformations. If the gauge group is Abelian, for example  $U(1)_{\text{EM}}$ , the structure constant  $f^{abc}$  is equal to zero. For  $SU(2)$ , the group of the weak isospin of left-handed particles,  $f^{abc}$  is equal to the antisymmetric tensor  $\epsilon^{abc}$  and  $T^a$  are basically the Pauli matrices. In  $SU(3)$ , the generators  $T^a$  are given by the  $3 \times 3$  Gell-Mann matrices. The covariant derivative of the gaugino fields is given by  $\nabla_\mu \lambda^a = \partial_\mu \lambda^a + g f^{abc} A_\mu^b \lambda^c$ .

The soft SUSY breaking term  $\mathcal{L}_{\text{soft}}$  will be given in the following section.

#### 1.4.4 Soft breaking of SUSY

As we have seen in Sec. 1.4.2, the SM particles and their superpartners should have the same mass. This is a direct result from the generator of Poincaré super algebra  $Q$  commuting with the generator of continuous space-time translations  $P_\mu$ . The fact that we have not observed any superpartners yet simply implies that the masses of the superpartners have to be higher than the masses of the SM particles. Thus the symmetry between SM particles and their superpartners is not exact and has to be broken somehow.

To break SUSY, two possible methods exist. On the one hand, SUSY could be broken spontaneously by a mechanism similar to the spontaneous breaking of the electroweak symmetry. This possibility is highly preferable since less parameters are necessary that need to be experimentally fitted to data. Many dedicated mechanism have been discussed [45–48], however, nobody knows if and how the spontaneous breaking of SUSY is exactly realized in nature. Additionally, by breaking global SUSY spontaneously, massless Nambu-Goldstone bosons and their corresponding superpartners (goldstinos) occur which have not been found by experiments yet. In contrast to the Higgs mechanism where the Goldstone bosons of the symmetry breaking are absorbed into the longitudinal components of the weak vector bosons, the Goldstone bosons of the spontaneous SUSY breaking do not vanish. Therefore, these Goldstone bosons and the corresponding goldstinos are physical and manifest themselves in the SUSY spectrum.

In practice though, symmetry breaking terms are introduced into the SUSY Lagrangian explicitly to parametrize our lack of understanding of the origin of SUSY breaking. These explicit symmetry breaking terms have to fulfill strict requirements. For instance, they should not introduce new quadratic divergences, otherwise this would again lead to the fine tuning problem discussed in the introduction which SUSY originally had a solution for. The explicit symmetry breaking terms that break SUSY only at lower energy scales and leave the physics at higher scales un-

## Introduction

touched are called *soft SUSY breaking* (SSB) terms. The SSB terms must be of positive mass dimension in order to be able to have a natural hierarchy between the electroweak scale and any higher energy scale. Thus, the hard processes keep on respecting the symmetry while the soft processes violate it. No new quadratic divergences contribute to the Higgs mass since the soft symmetry breaking terms are negligible at very high energies. In fact, it was shown by Ref. [49] that SSB terms do not introduce new quadratic divergences in quantum correction to all orders in perturbation theory. Although SUSY breaking is in most models realized by explicit terms, these terms, which effectively model the low energy effects of a theory at a higher scale, have to originate from a mechanism of spontaneous symmetry breaking.

In general, the SSB Lagrangian can be written as

$$\begin{aligned} \mathcal{L}_{\text{soft}} = & -\frac{1}{2}M_a\lambda^a\lambda^a - \frac{1}{2}a^{ijk}\phi_i\phi_j\phi_k - \frac{1}{2}b^{ij}\phi_i\phi_j - t^i\phi_i + \text{h.c.} \\ & - (m^2)_j^i\phi^{*j}\phi_i. \end{aligned} \quad (1.14)$$

The individual terms are the gaugino mass terms  $M_a$ , the trilinear (bilinear) couplings  $a^{ijk}$  ( $b^{ij}$ ) between three (two) scalar particles, and the scalar squared-mass terms  $(m^2)_j^i$ . The tadpole couplings  $t^i$  arise only if the scalar fields  $\phi_i$  are gauge singlets which is not the case for the MSSM. The Lagrangian  $\mathcal{L}_{\text{soft}}$  breaks SUSY since there are no gauge bosons nor supersymmetric counterparts for the individual terms in  $\mathcal{L}_{\text{soft}}$ . To limit the number of free parameters, the trilinear and the bilinear couplings  $a^{ijk}$  and  $b^{ij}$  are usually set to the constants  $A_0$  and  $B_0$  at the GUT scale, respectively.

One direct consequence of SUSY breaking is that the mass eigenstates of the superpartners are not necessarily the interaction eigenstates which we will discuss in the following. Similar to the breaking of the electroweak symmetry in the SM by the Higgs mechanism, where one neutral Higgs boson is left from one isospin Higgs doublet, three neutral ( $h_0$ ,  $H_0$ ,  $A_0$ ) and two charged Higgs bosons ( $H^+$ ,  $H^-$ ) are the remainders of the electroweak symmetry breaking in the MSSM. As in the case of the SM, three degrees of freedom, that would usually form the Goldstone bosons of the symmetry breaking mechanism, are absorbed into the longitudinal components of the  $W^\pm$  and  $Z$  bosons and form their mass terms. The photon  $\gamma$  and the  $Z$  boson are dynamically generated as a mixture of the  $B$  and the  $W^0$  bosons. This mixing is defined by the Weinberg mixing matrix which originates from the Glashow-Salam-Weinberg model [2–4].

What is more, the Higgsinos and the weak gauginos with similar charge mix among each other. The resulting mass eigenstates are the neutralinos  $\tilde{\chi}_i$  ( $i = 1, \dots, 4$ ) and

the charginos  $\tilde{\chi}_j^\pm$  ( $j = 1, 2$ ), commonly referred to as weakinos throughout this thesis. The interaction eigenstates of the squarks with similar mass and quantum numbers mix to give the mass eigenstates  $\tilde{u}_i, \tilde{d}_i, \tilde{s}_i, \tilde{c}_i, \tilde{b}_i$  and  $\tilde{t}_i$  ( $i = 1, 2$ ). It is sufficient to neglect the mixing of the first and second generation of squarks since the off-diagonal elements of the two  $6 \times 6$  mixing matrices vanish for the first and second generation for vanishing quark masses. The same applies for the right- and left-handed components of the selectron  $\tilde{e}$ , smuon  $\tilde{\mu}$  and stau  $\tilde{\tau}$  which mix to form the mass eigenstates with indices  $i = 1, 2$ . Similarly to the mixing of the squarks, the mixing of the first and second generation can be neglected and the interaction eigenstates of the selectron and smuon become equal to their mass eigenstates. Additionally, no other  $CP$ -violating interactions other than the standard  $CP$ -violating terms of the Yukawa sector are typically considered in the MSSM which would lead otherwise to the SUSY flavor problem [50–52]. We obtain for the particle content of the MSSM after electroweak and SUSY breaking:

$$\begin{aligned}
 \tilde{W}^+, \tilde{W}^-, \tilde{H}_u^+, \tilde{H}_d^- &\rightarrow \tilde{\chi}_1^+, \tilde{\chi}_1^-, \tilde{\chi}_2^+, \tilde{\chi}_2^-, \\
 \tilde{B}^0, \tilde{W}^0, \tilde{H}_u^0, \tilde{H}_d^0 &\rightarrow \tilde{\chi}_1^0, \tilde{\chi}_2^0, \tilde{\chi}_3^0, \tilde{\chi}_4^0, \\
 \tilde{u}_L, \tilde{u}_R, \tilde{d}_L, \tilde{d}_R &\rightarrow \tilde{u}_L, \tilde{u}_R, \tilde{d}_L, \tilde{d}_R, \\
 \tilde{s}_L, \tilde{s}_R, \tilde{c}_L, \tilde{c}_R &\rightarrow \tilde{s}_L, \tilde{s}_R, \tilde{c}_L, \tilde{c}_R, \\
 \tilde{t}_L, \tilde{t}_R, \tilde{b}_L, \tilde{b}_R &\rightarrow \tilde{t}_1, \tilde{t}_2, \tilde{b}_1, \tilde{b}_2, \\
 \tilde{e}_L, \tilde{e}_R, \tilde{\nu}_{eL} &\rightarrow \tilde{e}_L, \tilde{e}_R, \tilde{\nu}_{eL}, \\
 \tilde{\mu}_L, \tilde{\mu}_R, \tilde{\nu}_{\mu L} &\rightarrow \tilde{\mu}_L, \tilde{\mu}_R, \tilde{\nu}_{\mu L}, \\
 \tilde{\tau}_L, \tilde{\tau}_R, \tilde{\nu}_{\tau L} &\rightarrow \tilde{\tau}_1, \tilde{\tau}_2, \tilde{\nu}_{\tau L},
 \end{aligned} \tag{1.15}$$

and for the Higgs and the electroweak gauge bosons:

$$\left. \begin{array}{l} H_u^+, H_u^0, H_d^0, H_d^- \\ W^\pm, W^0, B^0 \end{array} \right\} \rightarrow \left\{ \begin{array}{l} h^0, H^0, A^0, H^\pm, \\ W^\pm, Z, \gamma. \end{array} \right.$$

The bosons  $h^0$  and  $H^0$  are  $CP$ -even, whereas  $A^0$  is  $CP$ -odd. Throughout the rest of this thesis we identify  $h^0$  with the lightest Higgs boson which was experimentally discovered recently.

### 1.4.5 $R$ -parity

Besides many other symmetries, the Lagrangians of supersymmetric theories can exhibit another important discrete symmetry. Under the so-called  $R$ -parity [53, 54] all SM fields are even while the superpartners of the SM fields are odd. The  $R$ -parity of a particle with baryon number  $B$ , lepton number  $L$  and spin  $S$  is given by [55]

$$R = (-1)^{3B+L+2S}. \quad (1.16)$$

$R$ -parity emerges from a continuous  $U(1)$   $R$ -invariance [56] that is broken by a finite gravitino mass [43]. After breaking the continuous  $R$ -invariance of the MSSM Lagrangian by a finite gravitino mass, the discrete  $R$ -parity remains. If  $R$ -parity would not be a symmetry of the MSSM Lagrangian, additional baryon or lepton number violating terms would be allowed. These additional terms would then lead to processes which are experimentally excluded or are at least suppressed by orders of magnitudes. For instance, a non-conserved  $R$ -parity would lead to the decay of the proton whose lifetime of more than  $10^{34}$  years at 90% confidence level is supported by experiments [57].

$R$ -parity conservation has interesting phenomenological implications. Since  $R$ -parity is conserved in the MSSM, superpartners can only be produced in pairs (the initial states at hadron colliders have  $R = 1$ ) and the lightest supersymmetric particle (LSP) is stable. This means that decay chains of supersymmetric pair production processes will always end in at least one stable LSP. Since in many models the LSP is neutral and therefore leaves the detector unnoticed, important observables for supersymmetric pair production processes with conserved  $R$ -parity are missing energy and monojet signatures. Due to its properties, the LSP can be identified as a suitable dark matter candidate.

Although  $R$ -parity conservation is a promising tool to comply with experimental results, many models and calculations exist that study the effects of  $R$ -parity violation<sup>5</sup>. For example, neutrino masses and mixing matrices could be automatically generated by  $R$ -parity violating terms [56].

---

<sup>5</sup>Note that  $R$ -parity can be broken without supersymmetry being broken [55].

## 1.5 Constrained models and experimental status

In the last decades, the parameter space for constrained supersymmetric models has been narrowed more and more. It appears to a lot of physicists that SUSY is ruled out and to them it seems that our world is not supersymmetric. However, these considerations are usually based on specific constrained or simplified models, meaning that several simplifying relations between the SUSY parameters are considered or that not the whole particle content of the MSSM is taken into account. The supersymmetric parameter space is much larger than the number of parameters in the SM. In total, 124 parameters including the parameters of the SM have to be controlled to obtain testable results [58]. Although testing SUSY for all possible parameter combinations is unpractical, in principle SUSY could hide in an exotic parameter space which is inaccessible by constrained or simplified models. In practice though, one has to rely on constrained models to search for evidence of SUSY.

The most prominent constrained models are [59]:

- CMSSM [60]: Relations among the parameters of the constrained MSSM are motivated by supergravity models. The soft SUSY breaking (SSB) masses are required to be equal at the GUT scale ( $\approx 2 \times 10^{16}$  GeV). The gaugino soft masses unify to the common value  $m_{1/2}$ , whereas the SSB masses of all sfermions and Higgs bosons are set to  $m_0$  at the GUT scale. Additionally, a common trilinear SSB parameter  $A_0$ , the ratio of Higgs vacuum expectation values (VEVs)  $\tan\beta$  and the sign of the Higgs mixing parameter  $\text{sign}(\mu)$  are defined at the electroweak scale. No additional flavor-violating terms are present in the CMSSM, except the terms which are already present in the SM. In that sense, the CMSSM is a minimal flavor violating (MFV) model. The free parameters of the CMSSM are

$$m_{1/2}, m_0, A_0, \tan\beta, \text{sign}(\mu). \quad (1.17)$$

- mSUGRA [61–64]: The minimal supergravity model has similar motivations as the CMSSM, except additional simplifying relations between parameters are considered. For instance the sum of the bilinear SSB parameter  $B_0$  and the universal scalar mass  $m_0$  are associated with the trilinear SSB parameter  $A_0$ , meaning  $A_0 = B_0 + m_0$ . The ratio of the Higgs VEVs  $\tan\beta$  is fixed by

the radiative electroweak symmetry breaking conditions [65]. Hence, the free parameters of mSUGRA are

$$m_{1/2}, m_0, A_0, \text{sign}(\mu). \quad (1.18)$$

- NUHM [66, 67]: In the non-universal Higgs mass model less restrictive boundary conditions at the GUT scale are assumed. Due to these assumptions, the mass spectrum of the non-universal Higgs mass model shows more features in the SUSY mass spectrum than other unified models. In particular, the SSB Higgs masses are chosen different from the SSB sfermion masses at the GUT scale. Depending on whether the two SSB Higgs masses  $m_{H_u}, m_{H_d}$  are the same or different, two scenarios are distinguished:

$$\text{NUHM1: } m_{1/2}, m_0, m_H \equiv m_{H_u} = m_{H_d}, A_0, \tan \beta, \text{sign}(\mu),$$

$$\text{NUHM2: } m_{1/2}, m_0, m_{H_u}, m_{H_d}, A_0, \tan \beta, \text{sign}(\mu).$$

- pMSSM(10) [68]: The phenomenological MSSM is considered as a complementary framework to the GUT motivated models. All free parameters are defined at the electroweak scale. However, to gain control over the vast parameter space, well-motivated assumptions are made. Motivated by the absence of flavor-violating terms, the equality of the SSB contributions to the squark masses of the first and second generation is assumed, which is made also for the three slepton generations. For the sake of simplicity, the SSB contributions to the masses of the left- and right-handed sfermions are considered to be equal. The pMSSM10 has the following free parameters:

three gaugino masses:  $M_{1,2,3}$ ,

two squark masses:  $m_{\tilde{q}_1} = m_{\tilde{q}_2} \neq m_{\tilde{q}_3}$ ,

one slepton mass:  $m_{\tilde{l}}$ ,

trilinear SSB parameter:  $A_0$ ,

Higgs mixing parameter:  $\mu$ ,

pseudoscalar Higgs mass:  $M_A$ ,

ratio of Higgs VEVs:  $\tan \beta$ .

Within the parameter space of these models, phenomenological searches for supersymmetric particles at hadron colliders are made. Up to this moment, experiments have only provided exclusion limits since no excess above the SM expectation was

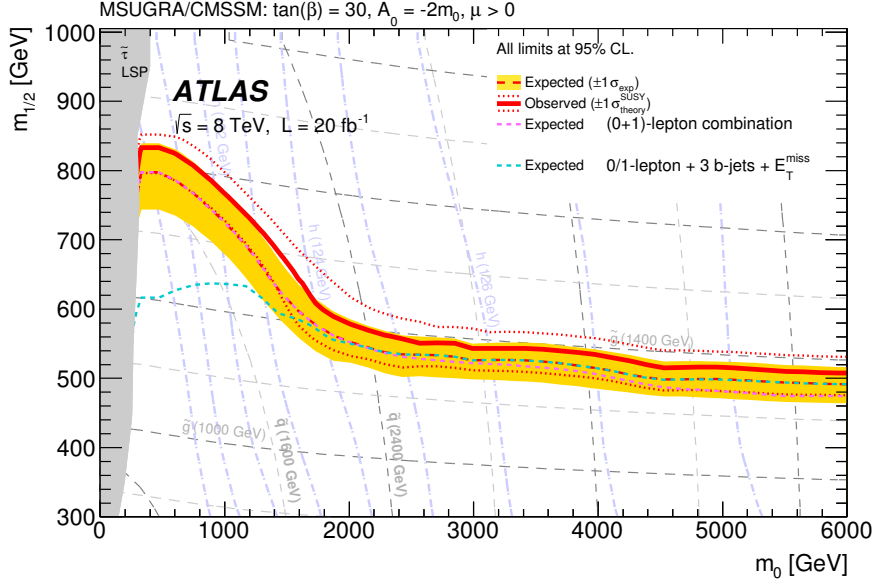


Figure 1.3: Exclusion limits from the ATLAS experiment for the mSUGRA model with  $\tan\beta = 30$ ,  $A_0 = -2m_0$  and  $\text{sign}(\mu) > 0$ . Figure taken from Ref. [69]. The excluded regions of the  $(m_0, m_{1/2})$ -plane are below and to the left of the lines. The solid red curve represents the 95% confidence level (CL) of the observed limit, while the dotted red curves show the  $\pm 1\sigma$  variation of the signal cross section due to the PDF and scale uncertainties. The dotted magenta (respectively cyan) line with the shaded yellow band around is the 95% CL of the expected limit with the  $\pm 1\sigma$  variation for the  $(0+1)$ -lepton combination<sup>6</sup> (respectively the  $(0+1)$ -lepton combination with 3 bottom jets and missing energy).

yet observed. We want to briefly discuss the recent limits on different mass parameters with respect to specific constrained models. The exclusion limits presented here are valid only in the considered model. Therefore, comparing the exclusion limits of two different models is difficult.

Figure 1.3 shows the exclusion limit for the mSUGRA model for the gaugino soft mass  $m_{1/2}$  and the Higgs soft mass  $m_0$  with additional constraints (see the caption of Fig. 1.3 for more details). This search excludes gluino masses smaller than  $\approx 1400$  GeV. By using a spectrum calculator (`SoftSUSY 4.0` [70]) we get, for

<sup>6</sup> The  $(0+1)$ -lepton combination refers to the statistical combination of events with no leptons + 2 – 6 jets +  $E_T^{\text{miss}}$ , and 1-lepton (soft+hard) + jets +  $E_T^{\text{miss}}$  [69].

example, a chargino mass of  $m_{\tilde{\chi}_1^\pm} \approx 500$  GeV for the point  $m_{1/2} = 600$  GeV and  $m_0 = 2200$  GeV, which is not excluded by this analysis.

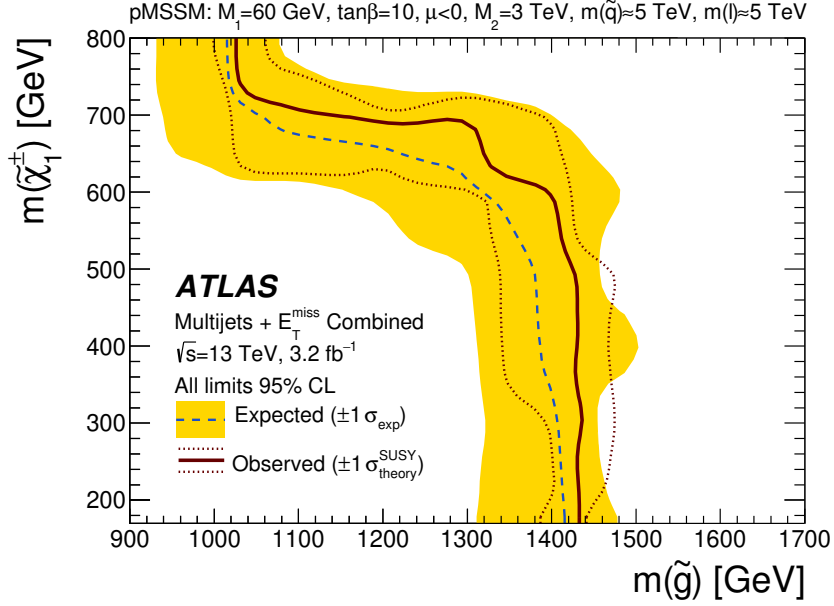


Figure 1.4: Exclusion limits from the ATLAS experiment for the pMSSM model with  $M_1 = 60$  GeV,  $\tan \beta = 10$ ,  $\text{sign}(\mu) < 0$ ,  $M_2 = 3$  TeV,  $m_{\tilde{q}} = 5$  TeV and  $m_{\tilde{l}} = 5$  TeV. Figure taken from Ref. [71]. Excluded regions of the  $(m_{\tilde{\chi}_1^\pm}, m_{\tilde{g}})$ -plane are below and to the left of the lines. The solid red curve represents the 95% confidence level (CL) of the observed limit, while the dotted red curves show the  $\pm 1\sigma$  variation of the signal cross section due to the PDF and scale uncertainties. The dotted blue line with the shaded yellow band around is the 95% CL of the expected limit with the  $\pm 1\sigma$  variation.

A more recent analysis has been made for the pMSSM by using experimental data with a center of mass energy of  $\sqrt{s} = 13$  TeV. Figure 1.4 shows the excluded region of the  $(m_{\tilde{\chi}_1^\pm}, m_{\tilde{g}})$ -plane in the pMSSM. The plot in Fig. 1.4 has been obtained by comparing the observed event count with that expected from SM background plus SUSY signal processes [71]. For the analysis, multijet processes including missing energy have been considered. As a result, we see that gluino masses up to 1400 GeV are excluded for this pMSSM slice. Although the data set used for this analysis is more up-to-date, a chargino mass  $m_{\tilde{\chi}_1^\pm}$  of  $\approx 200$  GeV is still compatible with the



experimental data if the gluino mass is sufficiently high.

This shows that the exclusion limits obtained for different models may give totally contrary results. It is only possible to make a meaningful statement on the status of SUSY if all of these different exclusion limits for the specific models are considered. For more results on ongoing SUSY searches see Ref. [72, 73]. We take into account the recent constraints on SUSY in Chap. 3 where we will give the results for weakino-pair and weakino-pair plus jet production in the framework of the MSSM. However, before going into the details of weakino-pair and weakino-pair plus jet production, we want to give an overview of the current techniques to compute observables in the framework of QFT.



## 2 Theoretical background

### 2.1 Calculating observables in QFT

Although QFT is known to be the most successful and best tested theory in physics, calculations in the framework of QFT are very challenging. The non-trivial structure of the vacuum of quantum chromodynamics (QCD), the non-perturbative regime of QCD, multi-particle interactions, infrared and ultraviolet divergences - just to mention a few of them - are obstacles on the way to physical observables, which have to be overcome by suitable mathematical methods. In this chapter we want to address the most important techniques that are necessary to obtain precise theoretical predictions for observables of high energy experiments. This includes the calculation of observables with perturbative methods (Sec. 2.2), the evaluation of phase space integrals (Sec. 2.2.1), dealing with ultraviolet (Sec. 2.2.2) and infrared (Sec. 2.3) divergent integrals, and the improvement of perturbative calculations in certain phase space regions by parton showers and resummation (Sec. 2.4).

#### 2.1.1 The running of the strong coupling constant

QCD is effectively divided by the running of the strong coupling constant  $\alpha_s$  (see Fig. 2.1) into the perturbative (high energy) and the non-perturbative regime (low energy). The boundary that separates the two regimes is around 1GeV. Features of QCD that are important at low energies, for example the confinement of color-charged particles, masses or the substructure of hadronic particles, have to be addressed by suitable methods, for example by effective field or lattice gauge theories. Processes with a relevant energy scale higher than  $\approx 1\text{GeV}$  can be calculated by perturbative approaches (further details below).

In an experiment the true charge of a particle is never measurable, instead the charged particle is surrounded by virtual particles that carry charge themselves (vacuum polarization). This cloud of charged particles screens (or in the case of

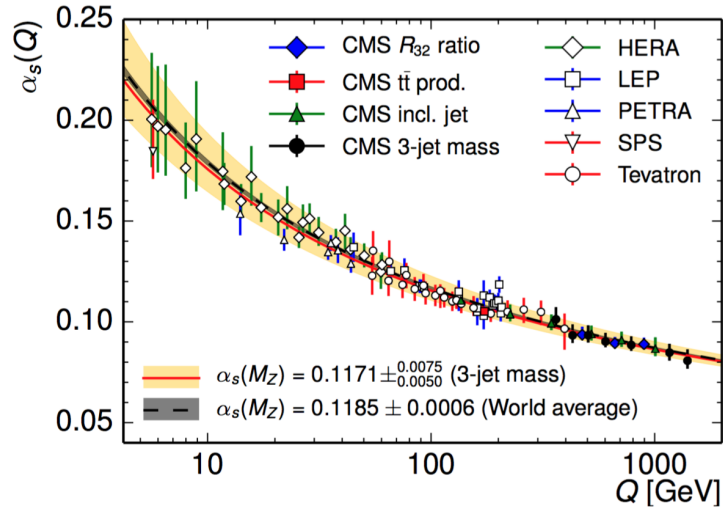


Figure 2.1: The dependence of the strong coupling constant  $\alpha_s$  on the energy scale. For lower energies the strong coupling constant rises up to values where a perturbative expansion of the physical observable in terms of the coupling constant is not feasible anymore. Plot taken from Ref. [74].

QCD: *anti*-screens) the true charge of the particle in the same way dipoles would do. For long distances this screening effect is small for QED, however, the opposite is true for QCD. Responsible for the increasing strength of the strong coupling constant at low energies are anti-screening effects which have the origin in the non-abelian character of QCD, meaning that even the gauge bosons of QCD carry charge. For a color-charged particle it is favorable to be surrounded by a cloud of gluons which increases the effective charge of the particle. Of course, quantitative calculations that rely on perturbative methods can be made to determine how „strong“ the effective charge is. Although, we will not explain the details of perturbative methods at this point, it is important to mention that the perturbative expansion of an observable into a power series introduces a dependence on a renormalization scale  $\mu_R$ . This dependence on a technical scale is unphysical why the observable should not depend on  $\mu_R$  if contributions to all orders of the expansion are taken into account.

Although the perturbative expansion up to all orders is technically impossible, we can still make predictions how the observable behaves at different energy scales. This behavior can be described by renormalization group equations (RGE) which follow directly from the argument above. For example, the RGE which describes how the strong coupling constant evolves from a given renormalization scale  $\mu_0$  to

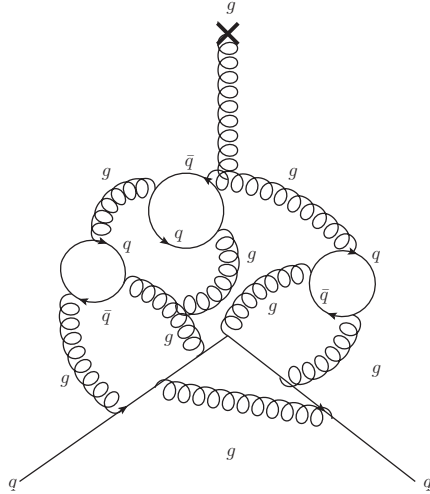


Figure 2.2: On the screening effect of the strong coupling constant  $\alpha_s$ . The probe (incoming gluon) does not „see“ the true charge of the quark, instead it couples to the cloud of gluons and quarks that surround the quark. Depending on the energy scale, the probe is being more or less influenced by the charge-cloud.

a different scale  $\mu_R$  is given by [75]

$$\mu_R^2 \frac{d\alpha_s(\mu_R^2)}{d\mu_R^2} = \beta(\alpha_s) = -\alpha_s^2 \sum_{n=0}^{\infty} \beta_n \alpha_s^n, \quad (2.1)$$

where  $\beta$  is the beta function of QCD which can be calculated by perturbative methods, and  $\beta_n$  are coefficients of the power series expansion of the beta function. The first two coefficients  $\beta_0$  and  $\beta_1$  are not dependent on the renormalization scheme (details in Sec. 2.2.2), while the other coefficients are [75]. In the one-loop approximation the solution of Eq. (2.1) is given by

$$\alpha_s(\mu_R^2) = \frac{\alpha_s(\mu_0^2)}{1 + \beta_0 \alpha_s(\mu_0^2) \log\left(\frac{\mu_R^2}{\mu_0^2}\right)}. \quad (2.2)$$

The analytic form of the first coefficient  $\beta_0$  in the SM is

$$\beta_0 = \frac{1}{4\pi} \left( \frac{11}{3} C_A - \frac{4}{3} T_F N_f \right), \quad (2.3)$$

where  $N_f$  is the number of active flavors, and  $C_A = 3$  and  $T_F = 1/2$  are the Casimir color factors.

The non-perturbative strength of the strong coupling constant at low energies has direct consequences on the observation of color-charged particles in nature. Quarks are always observed in color-neutral pairs - they are confined. Implications of color-confinement are observed later in this thesis by means of hadronization and the  $\overline{\text{MS}}$ -scheme. For very high energies, color-charged particles are asymptotically free [76, 77], meaning that  $\alpha_s(Q^2) \rightarrow 0$  for  $Q \rightarrow \infty$ .

### 2.1.2 Perturbative QFT

To calculate observables of processes with fundamental particles in QFT the  $\hat{S}$ -matrix

$$S_{fi} \equiv \langle f | \hat{S} | i \rangle, \quad (2.4)$$

is of special importance. In general the  $\hat{S}$ -matrix gives the amplitude of finding the final state  $\langle f |$  in the state  $(\hat{S} | i \rangle)$  after all possible interactions took place. The  $\hat{S}$ -operator which transfers an initial state to a final state can be written as

$$\hat{S} = \hat{T} \exp \left[ i \int d^4x \mathcal{L}_I \right]. \quad (2.5)$$

The Lagrangian  $\mathcal{L}_I$  encompasses all types of interactions which the particles of the theory could undergo,  $\hat{T}$  is the usual time ordering operator that acts on the fields after the exponential function has been expanded perturbatively.

Although other methods that are based on the evaluation of Eq. (2.5) exist<sup>1</sup>, we focus here on perturbation theory. In perturbation theory the observable is approximated by an infinite power series based on Eq. (2.5) where the coupling constants of the interactions are used as expansion parameters. These expansion parameters obviously have to be small compared to one in order to get a good convergence of the series, which is generally ensured by processes of the electroweak sector. In this case the fine structure constant  $\alpha$  which is relevant for electroweak processes is of order  $\mathcal{O}(1/100)$ . As already discussed in Sec. 2.1.1, applying perturbative methods to processes with color-charged particles work only well at energies above  $\approx 1\text{GeV}$ , or even better above  $10\text{GeV}$ , where the strong coupling constant  $\alpha_s$  is of order  $\mathcal{O}(1/10)$ .

To obtain observables with high precision, for most cases the perturbative expansion has to be carried out at least up to the second order (next-to-leading order, NLO). Many experimental measurements rely on theoretical calculations with even

---

<sup>1</sup>i.e. lattice gauge theory, see for example Ref. [78] for an overview.

higher precision, for example Higgs-pair production at next-to-next-to-leading order (NNLO) [79]. However, for processes beyond the SM a leading-order (LO) expansion of Eq. (2.5) is often already good enough. To make improvements to a fixed-order calculation, many corrections could be added, for example, corrections that are important in specific phase space regions, as it is done by resummation or parton showers (c.f. Sec. 2.4). Besides the cumbersome algebraic manipulation of complicated matrix elements for higher-order perturbative calculations, the analytic evaluation of integrals is time consuming. Therefore, in many cases computer aided tools can be used to simplify the calculation of observables by numerical methods, as we will see in the last chapter of this work.

To connect the non-trivial part of the  $\hat{S}$ -matrix with observables that can be measured at hadron colliders, we define the invariant matrix element  $\mathcal{M}_{fi}$  which is connected to the  $\hat{S}$ -matrix by

$$\langle f | \hat{S} - \mathbb{1} | i \rangle \equiv \frac{i\mathcal{M}_{fi} (2\pi)^4 \delta(P_f - P_i)}{\prod_{j=1}^{n_i} (2\pi)^{3/2} \prod_{k=1}^{n_f} (2\pi)^{3/2}}. \quad (2.6)$$

Formally, Eq. (2.6) follows from the Lehmann-Symanzik-Zimmermann reduction formula (LSZ) which was first discussed in Ref. [80]. We define  $P_f$  as the sum of the momenta of the final-state and  $P_i$  as the sum of the momenta of the initial-state particles. The delta-distribution  $(2\pi)^4 \delta(P_f - P_i)$  describes four-momentum conservation of the incoming and outgoing particles and occurs at all orders in every matrix element. The additional constants  $\prod_{j=1}^{n_i} (2\pi)^{3/2}$  and  $\prod_{k=1}^{n_f} (2\pi)^{3/2}$  are normalization constants which occur when the fields are Fourier transformed from position to momentum space. The number  $n_i$  equates to the number of incoming and  $n_f$  to the number of outgoing particles. The matrix element  $\mathcal{M}_{fi}$  could be determined in the framework of perturbation theory by so-called Feynman-rules, which are a simple but ingenious method to identify repeatedly occurring mathematical expressions with parts of a diagram [81].

Following from Fermi's Golden Rule, the (partonic) cross section of a 2 to  $n_f$  scattering process is obtained by integrating the invariant matrix element over the available phase space  $d\Phi_{n_f}$ , meaning

$$\sigma_{ab \rightarrow n_f} = \int d\mathcal{O} \frac{d\sigma}{d\mathcal{O}} = \frac{1}{F(p_a, p_b)} \int d\Phi_{n_f} |\mathcal{M}_{ab \rightarrow n_f}|^2, \quad (2.7)$$

where  $\mathcal{O}$  is an arbitrary observable that is experimentally measurable,  $d\sigma/d\mathcal{O}$  is the cross section differential in  $\mathcal{O}$  and

$$F(p_a, p_b) = 4\sqrt{(p_a \cdot p_b)^2 - m_a^2 m_b^2} \quad (2.8)$$

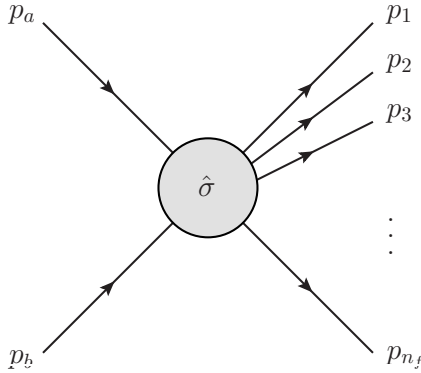


Figure 2.3: Scattering of two initial-state into  $n_f$  final-state particles at parton level.

is the flux factor,  $p_i$  and  $m_i$  ( $i = \{a, b\}$ ) are the momentum and the mass of the  $i$ -th incoming particle, respectively. For collider energies much higher than the masses of the incoming particles we can neglect their masses, so that  $m_i = 0$ . Therefore, the flux factor reduces to the simple form  $F = 2s$ , where  $s = (p_a + p_b)^2$  is the center of mass energy squared of the incoming (partonic) particles  $p_a$  and  $p_b$ .

### 2.1.3 Non-perturbative QFT

The last step is to understand how a cross section is calculated at a hadron collider such as the Large Hadron Collider (LHC). Here, particles having a substructure are collided which makes the process of calculating observables for hadron collisions a bit more cumbersome. Hadrons, especially protons, are composite particles, meaning that they are built up by partons such as quarks and gluons. The exact decomposition of protons and therefore the initial state of a proton-proton collision is not known precisely. Since the strong force between the partons in the low energy regime of a hadron does not allow a perturbative expansion of Eq. (2.5), we have to use other methods to describe the substructure of hadronic particles.

For this reason, a heuristic function that is measured in hadron collisions, is introduced to parametrize the internal structure of hadronic particles. This universal function  $f_a^{h_A}(x_A, \mu_F^2)$  is called parton distribution function (PDF) and it basically gives the probability of finding a parton  $a$  with momentum fraction  $x_A$  of the colliding hadron momentum  $P_A$ , inside the hadron  $h_A$ . The factorization scale  $\mu_F$  separates the non-perturbative regime, that is completely allocated to the PDFs, from the perturbative regime. Details on the factorization theorem will be given in



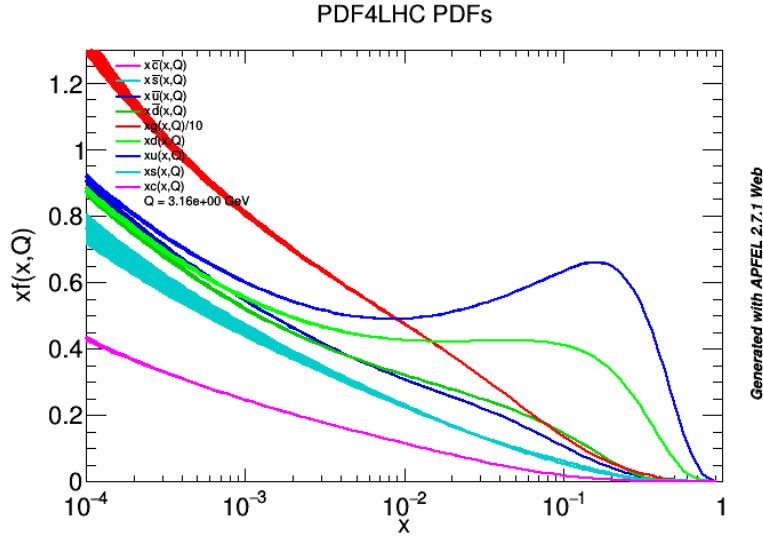


Figure 2.4: Different parton distribution functions multiplied by the momentum fraction  $x$  for the proton plotted with the APFEL webinterface<sup>2</sup> at the scale  $Q^2 = 10\text{GeV}^2$ . For better readability, the gluon densities are divided by a factor of ten.

### Sec. 2.3.

Scattering processes with highly energetic hadrons are most easily formulated in the Breit- or infinite-momentum frame [82]. In this frame, the internal degrees of freedom of the hadron are frozen due to time dilatation and no interaction between the partons occur. All partons roughly move in the same direction which means that we can assign the momentum fractions  $0 < x_A, x_B < 1$  of the hadron momentum  $P_A$  and  $P_B$  to the partons  $a$  and  $b$ , respectively:

$$\begin{aligned} p_a &= x_A P_A, \\ p_b &= x_B P_B. \end{aligned} \tag{2.9}$$

The parton distribution functions are universal, meaning that they are process independent. One can extract information on PDFs from basically every scattering experiment via fits and use it for the calculation of other hadronic processes.

The proton composition according to the PDF4LHC-PDF set is depicted at the energy scale of  $Q^2 = 10\text{ GeV}^2$  in Fig. 2.4. At large momentum fractions  $x$  the valence quark contributions of the up and down quarks dominate. This means that we can describe the proton at low energies solely as a composition of two up and one down

<sup>2</sup><https://apfel.mi.infn.it/home>

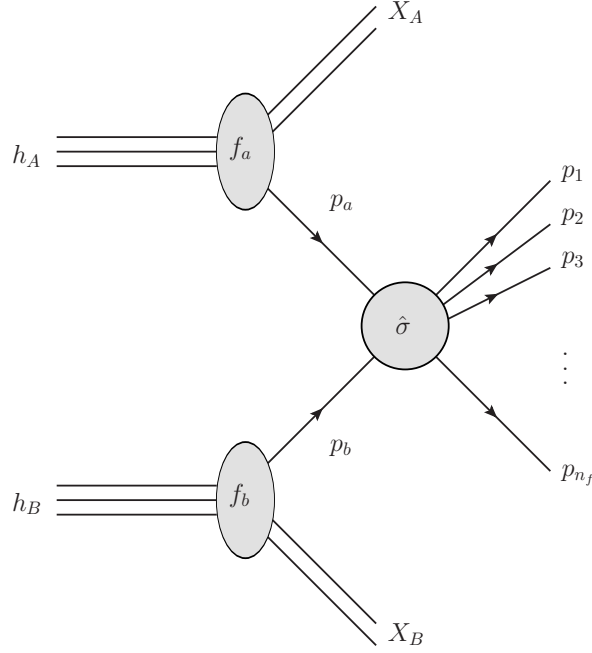


Figure 2.5: Scattering of two hadrons  $h_A$  and  $h_B$  into  $n_f$  final-state particles at the hadron level. We call  $X$  for the remainders of the hadrons, that are not involved in the scattering process. We do not care for them in an inclusive setup. Therefore, they are not considered any further.

quark. As we move to lower momentum fractions  $x$ , the sea quark contributions gain bigger influence and the gluon dominates the proton content.

We obtain the production rates at hadron level by folding the partonic cross section with the parton distribution functions of the hadrons  $h_A$  and  $h_B$

$$\begin{aligned} \sigma_{h_A h_B \rightarrow n_f} &= \sum_{a,b} \int_0^1 dx_A \int_0^1 dx_B f_a^{h_A}(x_A, \mu_F^2) f_b^{h_B}(x_B, \mu_F^2) \\ &\quad \times \sigma_{ab \rightarrow n_f}(s = x_A x_B S) \Theta(s \geq M^2), \end{aligned} \quad (2.10)$$

where  $M^2$  is the production threshold and is to be understood as the sum of the masses of the final-state particles

$$M^2 \equiv \left( \sum_{i=1}^{n_f} m_i \right)^2. \quad (2.11)$$

The partonic cross section  $\sigma_{ab \rightarrow n_f}$  is calculated as described in Eq. (2.7). It depends on the center of mass energy squared,  $s = (p_a + p_b)^2$ , or similarly on the hadronic

Mandelstam variable  $S = (P_A + P_B)^2$ , where  $P_A$  and  $P_B$  are the momenta of the hadrons  $h_A$  and  $h_B$ , respectively. The dependence on the final-state momenta  $p_i$  ( $i = 1, \dots, n_f$ ) is implicit in the above formula. The factorization theorem (c.f. Sec. 2.3) is only formulated for massless particles. Therefore, we have to put the masses of the partons  $m_a$  and  $m_b$  to zero. The relation  $s = x_A x_B S$  is thus exact, which would be a good assumption for high energetic hadron collisions anyway.

The integration can be rewritten in terms of the ratio of the partonic and hadronic Mandelstam variables  $\tau = s/S$  and the rapidity of the hadronic subsystem  $y = \frac{1}{2} \ln \frac{x_A}{x_B}$  which is more suitable for numerical calculations with Monte Carlo generators. We obtain

$$\sigma_{h_A h_B \rightarrow n_f} = \sum_{a,b} \int_{\frac{M^2}{S}}^1 d\tau \int_{\frac{1}{2} \ln \tau}^{-\frac{1}{2} \ln \tau} dy f_a^{h_A}(\tau, y, \mu_F^2) f_b^{h_B}(\tau, y, \mu_F^2) \sigma_{ab \rightarrow n_f}(s = \tau S), \quad (2.12)$$

which is used for the numerical evaluation of the cross-sections in this thesis.

## 2.2 Ingredients of an NLO calculation

Expanding the invariant matrix element  $\mathcal{M}_n = \sum_i \mathcal{M}_n^{(i)}$  for  $n$  final-state particles in terms of the coupling strength  $g_s(e)$  leads to different contributions to the observable of interest. The one with the lowest possible order in the coupling strength defines the leading order (LO) contribution. Usually the LO contribution is the most important one since terms that are proportional to higher-orders in the coupling constant are suppressed<sup>3</sup>. In the following we will focus on the LO and next-to-leading-order (NLO) contributions of a perturbative expansion for a simple  $2 \rightarrow n$  particle collision, meaning  $\mathcal{M}_n = \mathcal{M}_n^{(0)} + \mathcal{M}_n^{(1)}$ , where  $\mathcal{M}_n^{(0)}$  is the lowest order and  $\mathcal{M}_n^{(1)}$  the first correction to the matrix element. To this end, we examine the so-called Drell-Yan process which describes the annihilation of a quark and anti-quark into a virtual photon,  $q\bar{q} \rightarrow \gamma^*$ , followed by the splitting of the photon into two leptons,  $\gamma^* \rightarrow \ell\bar{\ell}$ . The Feynman rules for this process can be derived directly from the SM part of the Lagrangian defined in Sec. 1.4.3 and can be used to get the analytic expressions of the matrix element which correspond to the diagrammatic representation of Fig. 2.6.

The first approximation to the cross section, and the most important contribution

---

<sup>3</sup>Only if the coupling constant is much smaller than one.

## Theoretical Background

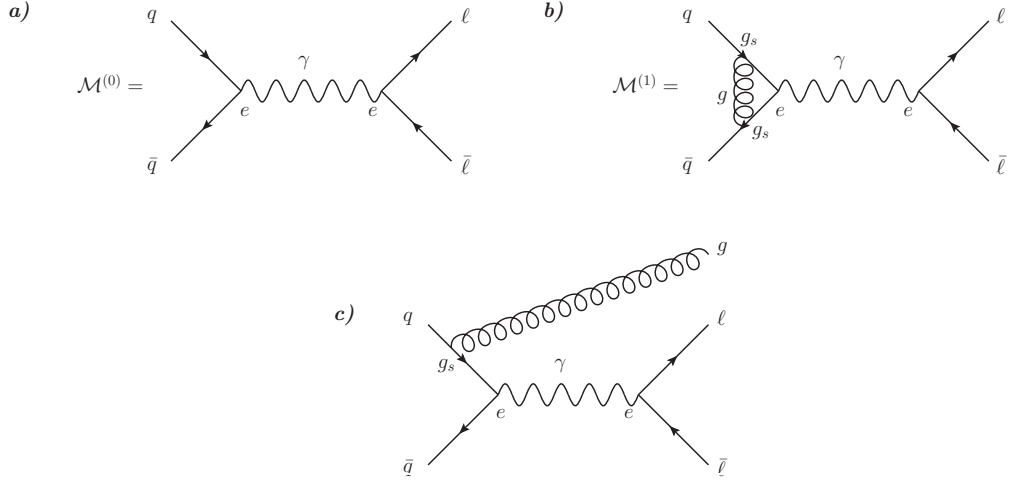


Figure 2.6: (a) Born, (b) virtual and (c) real contribution to the cross section of the Drell-Yan process  $q\bar{q} \rightarrow \ell\bar{\ell}$ . The Born amplitude is proportional to  $e^2$ , whereas the virtual is proportional to  $g_s^2 e^2$ . The real amplitude is proportional to  $g_s e^2$ .

is the Born amplitude which can be expressed following Eq. (2.7) by<sup>4</sup>

$$\sigma_n^{\text{LO}} = \sigma_n^{(0)} = \int d\Phi_n |\mathcal{M}_n^{(0)}|^2 \equiv \int d\Phi_n \mathcal{B}_n, \quad (2.13)$$

where we defined  $\mathcal{B}_n \equiv |\mathcal{M}_n^{(0)}|^2$  as the Born amplitude squared.

As it turns out, the total cross section at NLO consists of a  $n$ -particle and a  $(n+1)$ -particle contribution,

$$\sigma_n^{\text{NLO}} = \sigma_n^{\text{NLO}} + \sigma_{n+1}^{\text{NLO}}. \quad (2.14)$$

The  $n$ -particle contribution can again be split into the LO part  $\sigma_n^{(0)}$  and the first correction  $\sigma_n^{(1)}$ ,

$$\begin{aligned} \sigma_n^{\text{NLO}} &\equiv \sigma_n^{(0)} + \sigma_n^{(1)} \\ &= \int d\Phi_n |\mathcal{M}_n^{(0)} + \mathcal{M}_n^{(1)}|^2 \\ &\approx \int d\Phi_n \left\{ |\mathcal{M}_n^{(0)}|^2 + 2\text{Re} [\mathcal{M}_n^{(0)} \mathcal{M}_n^{(1)*}] \right\} + \mathcal{O}(\alpha_s^3) \\ &\equiv \int d\Phi_n (\mathcal{B}_n + \mathcal{V}_n). \end{aligned} \quad (2.15)$$

<sup>4</sup>Note that, for brevity, we omit the flux factor  $F$  from now on whenever it is not relevant.

The virtual amplitude is defined as the Born diagrams multiplied by the one-loop diagrams,  $\mathcal{V}_n \equiv 2\text{Re} [\mathcal{M}^{(0)}\mathcal{M}^{(1)*}]$ . The  $(n + 1)$ -particle contribution to the cross section at NLO are the real emission diagrams which are of the same order in the coupling strength as the virtual contribution  $\mathcal{V}_n$ . If the Born amplitude describes a  $2 \rightarrow n$  particle production process, the real amplitude reflects a  $2 \rightarrow n + 1$  process. Therefore, the real amplitude squared  $\mathcal{R}_{n+1}$  has to be integrated over a separate  $(n + 1)$ -particle phase space  $d\Phi_{n+1}$ . As we will see below in Sec. 2.3, the real emission diagrams have to be added to processes in order to cancel possible infrared (IR) singularities. An example of a real emission diagram is given in Fig. 2.6 (c). Finally, a general cross section at NLO can be written as

$$\sigma_{\text{NLO}} = \int d\Phi_n (\mathcal{B}_n + \mathcal{V}_n) + \int d\Phi_{n+1} \mathcal{R}_{n+1}. \quad (2.16)$$

### 2.2.1 Phase space

In the previous section we discussed how the total cross section  $\sigma_{\text{NLO}}$  could be calculated by integrating over the available phase space for the outgoing particles. To give a better insight into general phase space parametrizations and how to express them elegantly in terms of the final-state momenta, we want to briefly highlight the most important aspects here. The following section is based strongly on Refs. [83, 84].

As stated in the previous section, phase space integrals are used to sum over all possible final-state configurations. This summation follows from Fermi's Golden Rule which is used to obtain a measurable observable from the matrix element  $\mathcal{M}$ :

$$\sigma_n = \int d\Phi_n |\mathcal{M}_n|^2. \quad (2.17)$$

For a given 2 to  $n$  scattering process one has to determine the phase space measure  $d\Phi_n$  which is given by

$$d\Phi_n = \prod_{i=1}^n \left[ \frac{d^3 p_i}{(2\pi)^3 2E_i} \right] (2\pi)^4 \delta^4 \left( p - \sum p_i \right), \quad (2.18)$$

where  $p = p_a + p_b$  is the sum of the momenta of the incoming particles and  $E_i$  and  $p_i$  are the energy and momentum of the  $i$ -th final-state particle.

Evaluating this integral analytically can be very challenging. This is why Monte Carlo generators for processes with high multiplicity  $n$  and complex virtual and real contributions are useful.

## Theoretical Background

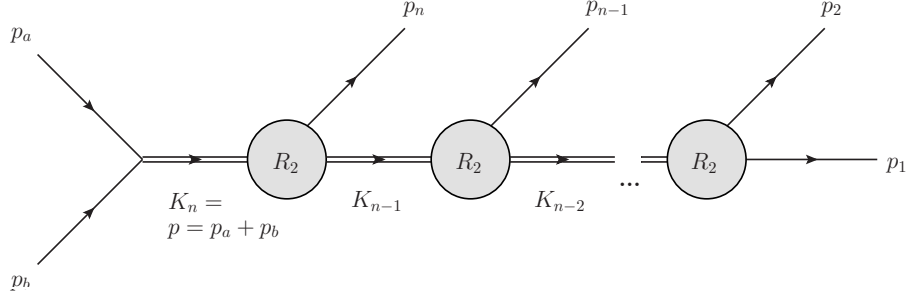


Figure 2.7: One possible general phase space parametrization with arbitrary multiplicity  $n$ .

For an arbitrary number of final-state particles we can define the phase space integral as

$$R_n(M_n^2) = \int_{\mu_{n-1}^2}^{(M_n - m_n)^2} dM_{n-1}^2 R_2(K_n; K_{n-1}^2, p_n^2) R_{n-1}(M_{n-1}^2), \quad (2.19)$$

where the two-body phase space is defined as

$$R_2(K_n; K_{n-1}^2, p_n^2) = \frac{\lambda^{\frac{1}{2}}(K_n^2, K_{n-1}^2, p_n^2)}{8K_n^2} \int d\Omega_n, \quad (2.20)$$

and the Kaellen triangle function  $\lambda$  is given by  $\lambda = x^2 + y^2 + z^2 - 2xy - 2yz - 2xz$ . We have to integrate over the solid angle  $\Omega_n$  to consider all possible angles between the final-state momenta.  $K_i$  and  $\mu_i$  are the sum of the final-state momenta and masses, respectively, up to the particle  $i$ :

$$K_i = p_1 + p_2 + \dots + p_i, \quad (2.21)$$

$$\mu_i = m_1 + m_2 + \dots + m_i. \quad (2.22)$$

Additionally, whenever the squared momentum  $K_i^2$  occurs, we are identifying it with the invariant mass squared  $M_i^2$ , meaning  $K_i^2 = M_i^2$ . Therefore, the invariant mass parameter squared  $M_n^2$  is equal to  $(p_1 + p_2 + \dots + p_n)^2 = (p_a + p_b)^2$ .

Eq. (2.19) has to be understood as an iterative formula, where one has to expand this equation until all momentum vectors are covered and the  $n$ -particle phase space is completely decomposed into nested two-particle phase spaces.

Next, we note that the flux factor defined in Eq. (2.8) can be expressed as a Lorentz invariant scalar using the Kaellen triangle function  $\lambda$ ,

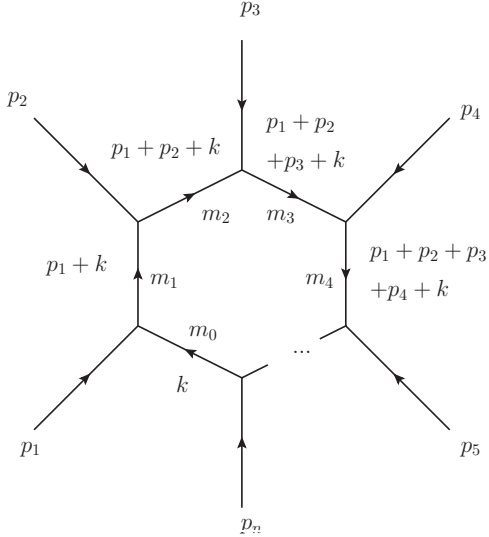
$$F = 2\lambda^{\frac{1}{2}}(p^2, m_a^2, m_b^2). \quad (2.23)$$

Finally, we define the cross section  $\sigma_n$  which consists of the phase space integral  $R_n$ , the matrix element squared  $|\mathcal{M}_n|^2$  and the factor  $(2\pi)^{3n-4}$  stemming from the phase space measure  $d\Phi_n$ :

$$\sigma_n = \frac{1}{(2\pi)^{3n-4} F} R_n(s) |\mathcal{M}_n|^2. \quad (2.24)$$

## 2.2.2 Regularization and renormalization

When Feynman diagrams are calculated, it is conspicuous that some diagrams occur which do not have a finite result and are thereby divergent. These divergences can appear when the diagram contains a closed particle loop. See Fig. 2.6 (b) for an example of such a loop diagram. Since the momentum  $k$  running in the loop is not fixed, we have to integrate over all possible values of  $k$ , that is from zero to infinity. Usually, these types of integrals are of the form



$$\propto \int \frac{d^4 k}{(2\pi)^4} f(k, p_1, p_2, \dots, p_n) \prod_{j=0}^n \frac{1}{(\sum_{i=0}^j p_i - k)^2 - m_j^2}, \quad (2.25)$$

where  $f$  is a general function of the momenta  $k$  and  $p_i$ . All momenta are incoming, thus the sum is zero due to momentum conservation,  $\sum_{i=1}^n p_i = 0$ . If  $n$  is small enough<sup>5</sup> these diagrams lead to divergences for large loop momentum  $k$ . To obtain finite results, these divergences have to be removed consistently from the calculation.

A theory which does have divergences can not be correct why quantum field theory was met with scepticism at the beginning. Especially Dirac pointed out that this indicates a physically meaningless theory [85]. However, as discovered later by Bethe

<sup>5</sup>By simply counting the powers of  $k$  in the numerator and denominator, we can estimate if the integral is divergent or finite.

## Theoretical Background

in 1947 [86], divergences can be subtracted by redefining the meaning of the input parameters of the calculation. Redefining the free parameters occurring in loop integrals is allowed, since they are not measurable by the experiment. At tree level the free parameters of the Lagrangian can be directly identified with the physical parameters measured by the experiment. However, when higher-orders are included, this simple relation does not hold anymore and the bare (original) and physical parameters differ by ultraviolet (UV) divergent contributions. Therefore, the bare parameters of the Lagrangian do not have a meaningful physical interpretation. By renormalizing all parameter such that the divergences of the bare parameters cancel the divergences of the loop integrals, the loop integrals become finite. For a broad overview of the method of renormalization see Ref. [87].

In detail, a regularization and renormalization procedure is carried out as follows. First the divergent integral must be regularized, that is to say a regulator has to be inserted which is used to separate the divergent part of the integral from the finite one. The most common regularization procedure is the dimensional regularization scheme (DREG) [88]. In this scheme, the dimensionality of the integration of loop integrals is reduced by an infinitesimally small number  $\varepsilon$ . Instead of carrying out the integration in four dimensions, the dimensionality of the integral is reduced to  $d = 4 - 2\varepsilon$  dimensions. After taking the limit  $\varepsilon \rightarrow 0$  the divergences manifest themselves in  $1/\varepsilon^n$  poles, where  $n \geq 1$ .

Formally, the dimensional regularization scheme is introduced by the replacement

$$\int \frac{d^4k}{(2\pi)^4} \rightarrow \mu_R^{4-d} \int \frac{d^d k}{(2\pi)^d}, \quad (2.26)$$

where  $\mu_R$  is the renormalization scale which is inserted to keep the correct mass dimension of the integral.

Advantages of the dimensional regularization over other regularization procedures (for example cutoff or the Pauli-Villars [89] method) are that linearity

$$\int d^d k (f(k) + g(k)) = \int d^d k f(k) + \int d^d k g(k), \quad (2.27)$$

scalability

$$\int d^d k f(sk) = s^{-d} \int d^d k' f(k'), \quad (2.28)$$

and translation invariance

$$\int d^d k f(k+q) = \int d^d k f(k), \quad (2.29)$$



of the loop integral are still valid. Most importantly, gauge invariance and other symmetries of the theory are not spoiled. Moreover, with DREG it is possible to regularize both UV and infrared divergences at once. An alternative regularization scheme is the dimensional reduction (DRED) [90], which is explained in more detail in Sec. 2.2.6. Additionally, calculations can also be regularized on the lattice by a finite lattice spacing [91].

### 2.2.3 Renormalization constants

After the integrals have been regularized by a suitable method, the parameters of the Lagrangians have to be renormalized. In the counterterm approach the UV-divergent bare parameters (labeled by the index 0) are expressed by a product of finite renormalized parameters and divergent renormalization constants. This method is in literature often referred to as the multiplicative renormalization. A theory is renormalizable if only a finite set of parameters needs to be renormalized at any perturbative order of the theory. For instance, the Standard Model, or more specifically massive Yang-Mills theories, are renormalizable as proven by 't Hooft [92–94].

To renormalize all UV-divergent parameters, the bare Lagrangian is split into a renormalized (physical) Lagrangian  $\mathcal{L}$  and a counterterm Lagrangian  $\delta\mathcal{L}$ ,

$$\mathcal{L}_0 = \mathcal{L} + \delta\mathcal{L}. \quad (2.30)$$

The renormalized Lagrangian  $\mathcal{L}$  has the same form as the bare Lagrangian  $\mathcal{L}_0$ . However, it depends on the renormalized parameters and fields which are used to calculate the Feynman rules of the processes of interest. When determining Feynman rules, the counterterm Lagrangian  $\delta\mathcal{L}$  gives additional rules that have to be included in the calculation in order to get finite results.

Let us consider in the following a simplified Lagrangian similar to the SUSY Lagrangian of Sec. 1.4.3 to shed light on the renormalization procedure. Since we are interested in the general procedure of renormalization, we do not take into account the scalar potential  $V(\phi, \phi^*)$ , the Yukawa term  $y\phi\bar{\Psi}\Psi$  and the auxiliary term  $1/2 D^2$ . We are considering one scalar field  $\phi$  with mass  $m_B$ , a Dirac spinor field  $\Psi = (\xi, \chi^\dagger)$  with mass  $m_F$  and chiral (Weyl) components  $\xi$  and  $\chi^\dagger$ , and a gauge vector field  $A$  with mass  $m_V$ . Furthermore, we are only interested in the kinetic part of the Lagrangian, since extending the renormalization procedure to interaction, gauge fixing or symmetry breaking terms is straight-forward. Hence, we

## Theoretical Background

have for the bare SUSY Lagrangian

$$\begin{aligned}\mathcal{L}_0^{\text{kin}} &= \nabla^\mu \phi_0^* \nabla_\mu \phi_0 - m_{B,0}^2 \phi_0^* \phi_0 + \bar{\Psi}_0 (i\not{\nabla} - m_{F,0}) \Psi_0 \\ &\quad - \frac{1}{4} F_{\mu\nu,0} F_0^{\mu\nu} + \frac{1}{2} m_{V,0}^2 A_{\mu,0} A_0^\nu\end{aligned}\quad (2.31)$$

where  $F_{\mu\nu,0} = \partial_\mu A_{\nu,0} - \partial_\nu A_{\mu,0}$  is the field strength tensor. Interactions with coupling strength  $g_0$  between the chiral and the gauge sector are introduced by gauging the chiral part of the Lagrangian (first line) with the covariant derivative  $\nabla_\mu = \partial_\mu - ig_0 A_{\mu,0}$ .

The following definitions for renormalization constants are similar to the definitions in Ref. [95]. We now renormalize all bare parameters of the Lagrangian by introducing

$$\begin{aligned}\phi_0 &\equiv Z_\phi^{1/2} \phi, \\ \xi_0 &\equiv (Z_\Psi^L)^{1/2} \xi, \\ \chi_0^\dagger &\equiv (Z_\Psi^R)^{1/2} \chi^\dagger, \\ A_0^\mu &\equiv Z_A^{1/2} A^\mu, \\ m_{B,0}^2 &\equiv Z_m^B m_B^2, \\ m_{F,0} &\equiv Z_m^F m_F, \\ m_{V,0}^2 &\equiv Z_m^V m_V^2, \\ g_0 &\equiv Z_g g,\end{aligned}\quad (2.32)$$

where the  $Z_i$  are the respective renormalization constants. We split the fermion field  $\Psi$  into chiral components with the chirality projector

$$P_{L/R} \equiv \frac{1 \mp \gamma_5}{2}.\quad (2.33)$$

In doing so, the Dirac part of the Lagrangian becomes (see Sec. 1.4.3)

$$\begin{aligned}\mathcal{L}_0^{\text{Dirac}} &= \bar{\Psi}_0 (i\not{\nabla} - m_{F,0}) \Psi_0 \\ &= i\xi_0^\dagger \bar{\sigma}_\mu \nabla^\mu \xi_0 + i\chi_0^\dagger \bar{\sigma}_\mu \nabla^\mu \chi_0 - m_{F,0} (\xi_0 \chi_0 + \xi_0^\dagger \chi_0^\dagger),\end{aligned}\quad (2.34)$$

with  $\bar{\sigma}^\mu = (\mathbb{1}, -\sigma_i)$  and  $\sigma_i$  ( $i = 1, 2, 3$ ) are the usual Pauli matrices.

After an infinitesimal expansion (leading divergences),  $Z_i = 1 + \delta Z_i$ , where  $\delta Z_i$  are

the counterterms, we obtain for the particle fields, masses and coupling constants

$$\begin{aligned}
 \phi_0 &= \left(1 + \frac{1}{2}\delta Z_\phi\right) \phi, \\
 \xi_0 &= \left(1 + \frac{1}{2}\delta Z_\Psi^L\right) \xi, \\
 \chi_0^\dagger &= \left(1 + \frac{1}{2}\delta Z_\Psi^R\right) \chi^\dagger, \\
 A_0^\mu &= \left(1 + \frac{1}{2}\delta Z_A\right) A^\mu, \\
 m_{B,0}^2 &= \left(1 + \delta Z_m^B\right) m_B^2 \equiv m_B^2 + \delta m_B^2, \\
 m_{F,0} &= \left(1 + \delta Z_m^F\right) m_F \equiv m_F + \delta m_F, \\
 m_{V,0}^2 &= \left(1 + \delta Z_m^V\right) m_V^2 \equiv m_V^2 + \delta m_V^2, \\
 g_0 &= (1 + \delta Z_g) g.
 \end{aligned} \tag{2.35}$$

We have introduced the new mass counter terms  $\delta m_B^2$ ,  $\delta m_F$  and  $\delta m_V^2$ . By inserting Eqs. (2.35) into Eq. (2.31), the bare Lagrangian  $\mathcal{L}_0$  splits into the renormalized Lagrangian  $\mathcal{L}$  and the counter Lagrangian  $\delta\mathcal{L}$ :

$$\mathcal{L}_0 = \mathcal{L} + \delta\mathcal{L}, \tag{2.36}$$

where

$$\begin{aligned}
 \mathcal{L} &= \nabla^\mu \phi^* \nabla_\mu \phi - m_B^2 \phi^* \phi \\
 &\quad + i\xi^\dagger \bar{\sigma}_\mu \nabla^\mu \xi + i\chi^\dagger \bar{\sigma}_\mu \nabla^\mu \chi - m_F (\xi\chi + \xi^\dagger \chi^\dagger) \\
 &\quad - \frac{1}{4} F_{\mu\nu} F^{\mu\nu} + \frac{1}{2} m_V^2 A_\mu A^\mu,
 \end{aligned} \tag{2.37}$$

and

$$\begin{aligned}
 \delta\mathcal{L} &= \left(\frac{1}{2}\delta Z_\phi^* + \frac{1}{2}\delta Z_\phi\right) \nabla^\mu \phi^* \nabla_\mu \phi - \left(\delta m_B^2 + \frac{1}{2}m_B^2\delta Z_\phi^* + \frac{1}{2}m_B^2\delta Z_\phi\right) \phi^* \phi \\
 &\quad + i\left(\frac{1}{2}\delta Z_\Psi^{L*} + \frac{1}{2}\delta Z_\Psi^L\right) \xi^\dagger \bar{\sigma}_\mu \nabla^\mu \xi + i\left(\frac{1}{2}\delta Z_\Psi^{R*} + \frac{1}{2}\delta Z_\Psi^R\right) \chi^\dagger \bar{\sigma}_\mu \nabla^\mu \chi \\
 &\quad - \left(\delta m_F + \frac{1}{2}m_F\delta Z_\Psi^L + \frac{1}{2}m_F\delta Z_\Psi^{R*}\right) \xi\chi \\
 &\quad - \left(\delta m_F + \frac{1}{2}m_F\delta Z_\Psi^{L*} + \frac{1}{2}m_F\delta Z_\Psi^R\right) \xi^\dagger \chi^\dagger \\
 &\quad - \frac{1}{4}\delta Z_A F_{\mu\nu} F^{\mu\nu} + \frac{1}{2}\left(\delta m_V^2 + m_V^2\delta Z_A\right) A_\mu A^\mu.
 \end{aligned} \tag{2.38}$$

The exact form of the counterterms is not fixed. As long as they cancel the UV-divergences of  $\mathcal{L}_0$ , the finite parts of the counterterms are arbitrary and we can

move finite parts between them and the free parameters of the Lagrangian. How the finite parts are fixed is determined by the renormalization conditions. Of course, the results for physical observables should not depend on our choice, as this dependence would be unphysical. However, when conducting a fixed-order perturbative calculation, the series expansion is truncated at a certain order in  $\alpha_s$  which introduces the aforementioned dependence on the renormalization scale  $\mu_R$  in the physical observables. For different renormalization conditions we then may get different results. This dependence should be viewed as theoretical uncertainty of our prediction. One should choose the condition that is best suited for the process under investigation. In the following sections we will go into further detail of different renormalization schemes.

### 2.2.4 On-shell scheme

The renormalization conditions follow from the general renormalized one-particle irreducible two-point functions [95]:

$$\begin{aligned}\hat{\Gamma}_{\mu\nu}^V(k) &= -ig_{\mu\nu} (k^2 - m_V^2) - i \left( g_{\mu\nu} - \frac{k_\mu k_\nu}{k^2} \right) \hat{\Sigma}_T^V(k^2) - i \frac{k_\mu k_\nu}{k^2} \hat{\Sigma}_L^V(k^2), \\ \hat{\Gamma}^B(k) &= i (k^2 - m_B^2) + i \hat{\Sigma}^B(k^2), \\ \hat{\Gamma}^F(k) &= i (\not{k} - m_F) \\ &\quad + i \left[ \not{k} P_L \hat{\Sigma}^{F,L}(k^2) + \not{k} P_R \hat{\Sigma}^{F,R}(k^2) + (m_F P_L + m_F P_R) \hat{\Sigma}^{F,S}(k^2) \right],\end{aligned}\quad (2.39)$$

where  $V$  denotes a spin-1 vector particle,  $B$  a spin-0 boson and  $F$  a spin-1/2 fermion with masses  $m_V$ ,  $m_B$  and  $m_F$ , respectively. The chirality projector  $P_{R/L}$  was defined earlier in Eq. (2.33). The  $\hat{\Sigma}$ 's are the respective renormalized self energy functions of the particles and are generally of the form

$$\hat{\Sigma}(k^2) = \Sigma(k^2) - \delta m^2 + (k^2 - m^2) \delta Z, \quad (2.40)$$

where  $\Sigma$  is the (unrenormalized) self energy function of the particle.

In the on-shell scheme, the renormalized mass parameters of the physical particles are chosen such that they are equal to the physical masses. Thus, in contrast to the  $\overline{\text{MS}}$ -scheme (c.f. Sec. 2.2.5) the on-shell scheme leads to a more intuitive interpretation of the parameters of the Lagrangian, and physical observables can be linked directly to the input parameters of the theory. Choosing the renormalized parameters equal to the physical parameters corresponds to taking the real parts of the poles of the propagators, or similarly, to the zeros of the one-particle irreducible

two-point functions. Additionally, we require that the renormalized one-particle irreducible two-point functions are diagonal if the external legs are on their mass shell which simplifies complicated matrix equations and the corresponding expressions for their eigenvalues.

More specifically, the renormalization conditions for the fields and masses are given by

$$\begin{aligned}
 \widetilde{\text{Re}} \hat{\Gamma}_{\mu\nu}^V(k) \epsilon^\nu(k) \Big|_{k^2=m_V^2} &= 0, \\
 \lim_{k^2 \rightarrow m_V^2} \frac{1}{k^2 - m_V^2} \widetilde{\text{Re}} \hat{\Gamma}_{\mu\nu}^V(k) \epsilon^\nu(k) &= -i \epsilon_\mu(k), \\
 \widetilde{\text{Re}} \hat{\Gamma}^B(k) \Big|_{k^2=m_B^2} &= 0, \\
 \lim_{k^2 \rightarrow m_B^2} \frac{1}{k^2 - m_B^2} \widetilde{\text{Re}} \hat{\Gamma}^B(k) &= i, \\
 \widetilde{\text{Re}} \hat{\Gamma}^F(k) u(k) \Big|_{k^2=m_F^2} &= 0, \\
 \lim_{k^2 \rightarrow m_F^2} \frac{k + m_F}{k^2 - m_F^2} \widetilde{\text{Re}} \hat{\Gamma}^F(k) u(k) &= i u(k). \tag{2.41}
 \end{aligned}$$

The operator  $\widetilde{\text{Re}}$  only takes the real parts of the loop integrals but not of complex parameters that can potentially occur in the above expressions. Since we are using real parameters, we replace  $\widetilde{\text{Re}}$  with the common real part  $\text{Re}$  from now on. Note that  $\epsilon^\mu(k)$  is the polarization vector of the spin-1 particle  $V$ , and  $u$  corresponds to the spinor of fermion  $F$ .

After applying the renormalization conditions to the renormalized one-particle irreducible two-point functions of Eq. (2.39) we obtain the explicit form of the renor-

malization constants:

$$\begin{aligned}
\delta m_V^2 &= \text{Re } \Sigma_T^V(m_V^2), \\
\delta Z_V &= -\text{Re} \left. \frac{\partial \Sigma_T^V(k^2)}{\partial k^2} \right|_{k^2=m_V^2}, \\
\delta m_B^2 &= \text{Re } \Sigma^B(m_B^2), \\
\delta Z_B &= -\text{Re} \left. \frac{\partial \Sigma^B(k^2)}{\partial k^2} \right|_{k^2=m_B^2}, \\
\delta m_F &= \frac{1}{2} m_F \text{Re} \left( \Sigma^{F,L}(m_F^2) + \Sigma^{F,R}(m_F^2) + 2\Sigma^{F,S}(m_F^2) \right), \\
\delta Z_F^L &= -\text{Re} \Sigma^{F,L}(m_F^2) \\
&\quad - m_F^2 \left. \frac{\partial}{\partial k^2} \text{Re} \left( \Sigma^{F,L}(k^2) + \Sigma^{F,R}(k^2) + 2\Sigma^{F,S}(k^2) \right) \right|_{k^2=m_B^2}, \\
\delta Z_F^R &= -\text{Re} \Sigma^{F,R}(m_F^2) \\
&\quad - m_F^2 \left. \frac{\partial}{\partial k^2} \text{Re} \left( \Sigma^{F,L}(k^2) + \Sigma^{F,R}(k^2) + 2\Sigma^{F,S}(k^2) \right) \right|_{k^2=m_B^2}. \tag{2.42}
\end{aligned}$$

### 2.2.5 The $\overline{\text{MS}}$ -scheme

Earlier in this thesis we observed that in QCD, in contrast to QED, color-charged particles cannot be measured isolatedly. Thus, color-charged particles always come in color-neutral combinations. Since the mass of an isolated quark can not be measured, renormalizing color-charged particles via the on-shell scheme is not reasonable. Additionally, the Thomson limit<sup>6</sup> of the strong coupling constant could not be defined properly in the on-shell scheme. A more suitable scheme to renormalize the quantities of color-charged particles presents the minimal subtraction scheme (MS) [96] or the modified minimal subtraction scheme ( $\overline{\text{MS}}$ ) [97]. In these two schemes only the  $1/\epsilon$ -poles (and some recurrent constants for the  $\overline{\text{MS}}$ -scheme), which usually come in the form

$$\frac{1}{\epsilon} \Gamma(1 + \epsilon) (4\pi)^\epsilon \stackrel{\epsilon \rightarrow 0}{\approx} \frac{1}{\epsilon} - \gamma_E + \log(4\pi) + \mathcal{O}(\epsilon), \tag{2.43}$$

are assigned to the renormalization constants,  $\gamma_E$  being the Euler-Mascheroni constant. Thus we define the renormalization constants  $\delta Z_i$  similar to Eqs. (2.42), with

<sup>6</sup>The Thomson limit is used in QED to define the electric charge at zero momentum transfer. At zero momentum transfer no corrections to the electric charge are expected, which fixes the renormalization constant for the electric charge. We will use the Thomson limit later in the  $\overline{\text{MS}}$ -scheme to fix the renormalization constant of the strong coupling constant, see Eq. (3.3.2).

the modification of only taking terms proportional to  $\Delta \equiv 1/\epsilon$  for the MS-scheme and proportional to  $\bar{\Delta} \equiv 1/\epsilon - \gamma_E + \log(4\pi)$  for the  $\overline{\text{MS}}$ -scheme.

A brief remark is in order here. For most of the calculations at high-energy hadron colliders it is sufficient to treat all quarks, except the top and bottom quarks, as massless particles. Therefore, the renormalization of the mass parameters of the light quarks is not required, while the mass of the bottom quark has to be renormalized in the  $\overline{\text{MS}}$ -scheme. However, in contrast to the statement above, due to its short lifetime, the top mass could be renormalized in the usual on-shell scheme. The top quark is more likely to decay weakly into leptons before it starts hadronizing. By measuring the invariant mass distribution of the two leptons, the top mass can be determined very precisely [98–100], which renders the on-shell scheme for the top mass well-defined.

## 2.2.6 SUSY restoring counterterm

As discussed in detail in Refs. [101–103] a mismatch between the  $(D - 2)$  transverse degrees of freedom of the gauge bosons and the two degrees of freedom of the gauginos is introduced by the dimensional regularization scheme. This results in a difference of the gauge coupling  $g^{\overline{\text{MS}}}$  and the Yukawa couplings  $\hat{g}^{\overline{\text{MS}}}$  beyond LO which is a strong breaking in the gauge sector and should be avoided in any circumstances. To remedy the inequality  $g^{\overline{\text{MS}}} \neq \hat{g}^{\overline{\text{MS}}}$  a finite SUSY restoring counterterm is added at next-to-leading order in the strong coupling  $\alpha_s$ ,

$$\hat{g}^{\overline{\text{MS}}} = g^{\overline{\text{MS}}} \left( 1 - \frac{\alpha_s}{6\pi} \right). \quad (2.44)$$

An alternative way of regularization that avoids this strong breaking of SUSY is the dimensional reduction scheme (DRED) for the calculation of the virtual corrections. In DRED fields remain defined in four dimensions (and the degrees of freedom are then preserved), while loop momenta are defined in  $D$  dimensions. Since this approach respects supersymmetry, the SUSY-restoring counterterm of Eq. (2.44) is not needed anymore. However, since the PDFs are using the  $\overline{\text{MS}}$ -scheme we have to use the same renormalization scheme in our calculation<sup>7</sup>. Thus, a finite shift of the virtual amplitudes passed to the Monte-Carlo program is necessary [104],

$$\mathcal{V} = \mathcal{V}^{\text{DRED}} - \frac{4}{3} \frac{\alpha_s}{2\pi} \mathcal{B}, \quad (2.45)$$

---

<sup>7</sup>Moreover, the choice of the  $\overline{\text{MS}}$ -scheme is constrained by the intrinsic treatment of IR singularities of the POWHEG-BOX.

where  $\mathcal{B}$  is the Born amplitude for a specific partonic subprocess calculated in four dimensions. As a cross-check, we have employed both regularization methods in our calculation, and we have found the same value for the virtual amplitude  $\mathcal{V}$  that enters the Monte-Carlo program in both schemes.

### 2.2.7 Complex mass scheme and renormalization

In quantum mechanics particles decay into other particles, if the mass of the mother particle is higher than the sum of the daughter particles and if the decay is not forbidden by conservation laws for the quantum numbers of the involved particles. Similar to the statistical description of radioactive decays, one introduces a mean lifetime  $\tau$  or the decay rate  $\Gamma = 1/\tau$  which in principle defines how many particles decay in a given time interval. The simplest method to include decay rates<sup>8</sup> of unstable particles is to replace the propagator of the particle with the Breit-Wigner form of the propagator:

$$\frac{1}{p^2 - m^2} \rightarrow \frac{1}{p^2 - m^2 + im\Gamma}. \quad (2.46)$$

However, this simple replacement spoils gauge invariance since the mass parameters of the numerator and denominator of the amplitude are treated differently. Instead, one can redefine the physical mass of the particle by a complex mass, which includes the particle width. This rule leads to the gauge independent complex mass scheme [105]:

$$m^2 \rightarrow \mu^2 = m^2 - im\Gamma. \quad (2.47)$$

Generally, the complex mass scheme has the same effect as replacing the propagator similar to Eq. (2.46). Wherever the mass occurs in the calculation the complex mass is used instead, especially for propagators that arise in loop functions. Due to the general replacement of the real mass parameter with the complex particle mass, complex parameters can even occur in the numerator of the matrix element. To still cancel all the UV divergences in the final matrix element, the renormalization procedure has to be slightly modified. Details can be found in Ref. [105], but the general procedure is the following:

- Introduce complex renormalization constants for renormalizing the mass  $m_0^2 = \mu^2 + \delta\mu^2$  and the field  $A_0 = (1 + \frac{1}{2}\delta Z)A$ .

---

<sup>8</sup>or similar *particle widths* in the language of quantum field theory



- Write the renormalized self energy in terms of the new renormalization constants  $\hat{\Sigma}(k^2) = \Sigma(k^2) - \delta\mu^2 + (k^2 - \mu^2)\delta Z$ .
- Apply the renormalization conditions  $\hat{\Sigma}(\mu^2) = 0$  and  $\hat{\Sigma}'(\mu^2) = 0$  which leads to explicit form of the renormalization constants  $\delta\mu^2 = \Sigma(\mu^2)$  and  $\delta Z = -\Sigma'(\mu^2)$ .
- Expand the (unrenormalized) self energy about the real arguments and neglect higher-orders in the coupling strength  $g$ , leading to terms  $\delta\mu^2 = \Sigma(\mu^2) \approx \Sigma(m^2) + (\mu^2 - m^2)\Sigma'(m^2)$  and  $\delta Z \approx -\Sigma'(m^2)$ .
- Insert the new explicit form of the renormalization constants into the renormalized self energy  $\hat{\Sigma}(k^2) = \Sigma(k^2) - \delta m^2 + (k^2 - m^2)\delta Z$  and define  $\delta\mu^2 = \Sigma(m^2)$  and  $\delta Z = -\Sigma'(m^2)$ .

After this procedure, the renormalization constants have the usual on-shell form as in Eq. (2.42), but without taking the real part of the counterterms. Now, we have to calculate the self energies with complex masses, although with real squared momenta.

## 2.3 Infrared divergences

Introducing the parton distribution function  $f_a^h$  in Eq. (2.12) has another important reason. When calculating observables in QFT, quantum corrections lead to divergences in the low energy regime for specific momentum configurations. In Sec. 2.2 we deduced that the general form of the cross-section at NLO can be written as

$$\sigma_{\text{NLO}} = \int d\Phi_n (\mathcal{B}_n + \mathcal{V}_n) + \int d\Phi_{n+1} \mathcal{R}_{n+1}, \quad (2.48)$$

where  $\mathcal{B}_n$  is the Born,  $\mathcal{V}_n$  is the virtual, and  $\mathcal{R}_{n+1}$  is the real matrix element squared.

Infrared *soft* divergences arise in the virtual and in the real matrix element squared if the energy of a massless particle running in a loop approaches zero or if the particle is emitted from an external leg with an energy going to zero. Infrared *collinear* divergences appear if a particle is emitted nearly parallel from an external leg. More technically, the momentum and energy configurations of soft and collinear divergences are:

$$\left. \begin{array}{l} \text{Soft divergence if} \\ \text{Collinear divergence if} \end{array} \right\} \begin{array}{l} E_k \rightarrow 0 \\ \vec{p}_k \parallel \vec{p}_l \end{array} \quad \text{for } k, l = 1, \dots, n+1. \quad (2.49)$$

## Theoretical Background

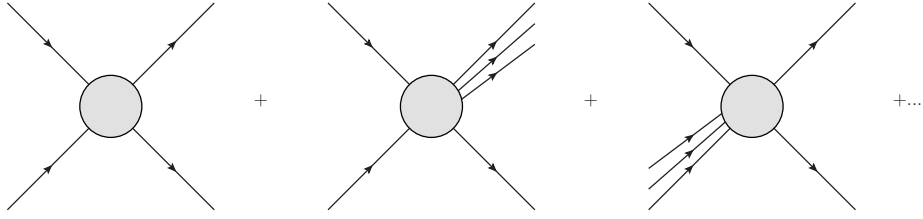


Figure 2.8: By summing over all possible initial and final-state particles that are responsible for IR divergences, the cancellation of IR divergences occurs. This means that not only the emittance of soft particles have to be considered, but also hard massless particles that are emitted nearly parallel to their parent particles have to be included. Therefore, we have to sum over all possible hard jets in the final state. Moreover, all possible initial states have to be included, meaning that we have to sum over processes with incoming jets of nearly parallel particles, too. Technically, these jets of incoming particles are assigned to the parton distribution functions.

The Kinoshita-Lee-Nauenberg (KLN) theorem [106, 107] states that all measurable quantities remain finite, if we sum over processes with all possible initial and final states that can give rise to soft or collinear divergences. We can gain control over the soft infrared divergences by regularization, whereas the remaining collinear divergences can be removed by factorization, which we will discuss to some extent in the following. To remove the remaining collinear divergences, the initial state of the scattering process is redefined in such a way that these divergences can be absorbed into them - at the price of introducing an unphysical factorization scale  $\mu_F$ . This is possible since the factorization of these divergences is universal Ref. [108]. The key idea of factorization is that the amplitude or cross section is a product of two factors which depend only on separate momentum scales. The factorization scale separates the non-perturbative regime (low energy or long distance physics) which is associated with the structure of the hadron, from the perturbative regime (high energy or short distance physics). This factorization ensures that we are able to calculate scattering processes at hadron colliders perturbatively, although the structure of the involved hadrons is not computable with perturbative methods.

Note, that the factorization theorems described in Ref. [108] are understood as a Taylor expansion in powers of the inverse hard scale  $1/Q$ . The separation of the

hadronic cross section into parton distribution functions and a partonic cross section,

$$\begin{aligned} \sigma_{h_A h_B \rightarrow n_f} &= \sum_{a,b} \int_0^1 dx_A \int_0^1 dx_B f_a^{h_A}(x_A, \mu_F^2) f_b^{h_B}(x_B, \mu_F^2) \\ &\sigma_{ab \rightarrow n_f}(s = x_A x_B S) \Theta(s \geq M^2), \end{aligned} \quad (2.50)$$

as deduced in Sec. 2.1.3, is the leading contribution. For certain subleading terms and processes the factorization theorems have been written down (for example for the Drell-Yan process [109, 110] or for deep inelastic scattering (DIS) [111, 112]). However, a proof to all orders in this expansion does not exist.

How PDFs evolve for a given scale  $Q$  to a scale  $\mu_F$  can be determined by the Dokshitzer-Gribov-Lipatov-Altarelli-Parisi (DGLAP) evolution equations [113–115],

$$\frac{\partial}{\partial \ln \mu_F^2} f_a^h(x, \mu_F^2) = \frac{\alpha_s}{2\pi} \sum_b \int_x^1 \frac{dz}{z} f_b^h\left(\frac{x}{z}, \mu_F^2\right) P_{ba}(z), \quad (2.51)$$

where  $P_{ba}(z)$  are the regularized Altarelli-Parisi splitting functions evaluated in four dimensions. More details can be found for example in the Appendix of [116]. The splitting functions will play an important role in Sec. 2.4, where we examine parton-shower Monte Carlo algorithms. It is advisable to choose  $\mu_F$  equal to the characteristic scale  $Q$  of the studied process, since the leading logarithms  $\alpha_s^n \log^n(Q^2/\mu_F^2)$ , which are resummed by the DGLAP equations, are then small.

### 2.3.1 Jets and infrared safety

An important tool of perturbative QFT is infrared safety, which defines a special class of infrared safe observables that are insensitive to long-distance physics [117]. An observable  $\mathcal{O}$  which depends on the momentum  $p_i$  must be invariant under the branching  $p_i \rightarrow p_j + p_k$  in the soft and collinear limit, meaning for the energies of the particles  $E_j \rightarrow 0$  or  $E_k \rightarrow 0$  (soft limit) and  $\vec{p}_j \parallel \vec{p}_k$  (collinear limit) [118]. Or in other words: The value of the observable should not change if any number of infinitely soft particles are added or if an existing particle splits up into two comoving particles. A more technical definition of an infrared safe observable will be given in Sec. 2.3.2 with the introduction of the measurement function  $\mathcal{S}$ . Typically, any correction to an infrared-safe observable is of order  $Q_{\text{IR}}/Q_{\text{UV}}$  [117], where  $Q_{\text{IR}} \approx 1\text{GeV}$  and  $Q_{\text{UV}}$  is the hard scale of the process.

As already discussed in Sec. 2.1.1, the coupling strength of QCD increases with longer distances why it is energetically favorable for two particles that move farther apart to excite two new particles from the vacuum. Due to this fact strongly

## Theoretical Background

charged particles collimate into bunches of particles and the resulting hadrons hit the detector roughly in the same direction as the color-charged particles they came from. These jets leave distinct signatures in the detectors. However, a jet observable must be defined in such a way that it suits both the experimental and theoretical requirements. The experimental requirement is to have a proper definition which particle belongs to which jet, whereas the theoretical concern is to define observables that obey infrared safety.

This definition is obtained by jet algorithms. See for example [119, 120] for an overview of well-established algorithms. The algorithm which we are using in our analysis, is the anti- $k_t$  algorithm [121] which is based on the Cambridge algorithm [122] and is implemented in the FASTJET package. The anti- $k_t$  algorithm uses a distances measure of two particles  $i$  and  $j$ ,

$$d_{ij} = \min(p_{T,i}^{-2}, p_{T,j}^{-2}) \frac{\Delta R_{ij}^2}{R^2}, \quad (2.52)$$

where

$$\Delta R_{ij}^2 = (y_i - y_j)^2 + (\Phi_i - \Phi_j)^2. \quad (2.53)$$

The rapidity  $y_i$  is a measure for the relativistic velocity and  $\Phi_i$  is the azimuthal angle of the particle  $i$ . By sequentially recombining the particles via the relative distance measures  $d_{ij}$  and the distance to the beam  $d_{iB} = (p_{T,i}^{2p})$  the algorithm determines which particle belongs to which cluster. The anti- $k_t$  algorithm favors clustering that involves hard particles rather than clustering of softer particles or energy-independent clusters. The free parameter  $R$  can be viewed as the separation of the two closest jets and is usually between 0.4 - 0.7 [123].

To reconstruct the jets, the algorithm follows the steps:

1. Calculate  $d_{ij}$  and  $d_{iB}$  for all particles.
2. If one of the  $d_{iB}$  is minimal, append the particle index  $i$  to the list of jets.
3. If  $d_{ij}$  is minimal, merge the particle  $i$  and  $j$  and treat them as an „effective“ particle with momentum  $p_{ij} = p_i + p_j$ .
4. Stop, if no particles are left, else start at the beginning.

Since a collinear branching gets clustered automatically at the beginning of the sequence, the grow around a hard seed of the jet is collinear safe. The anti- $k_t$  algorithm is fast and gives circular shaped jets which allows for an intuitive interpretation of physical events. It is implemented by both the ATLAS and CMS collaborations as the default jet algorithm Ref. [120].

### 2.3.2 The FKS subtraction method

In this section we discuss the details of the FKS (Frixione, Kunszt, Signer) subtraction method [124, 125] which is used amongst other methods (Catani-Seymour [116] subtraction, Antenna subtraction [126, 127], phase space slicing [128]) to cancel the infrared singularities of the virtual and real amplitudes numerically. As stated by the KLN theorem and described in Sec. 2.1.2 the IR singularities of the real and virtual amplitudes ultimately cancel if we sum over all possible processes which give rise to IR divergences. However, since these amplitudes are defined on different phase spaces, cancellation is numerically difficult or even impossible for a Monte Carlo generator. To make both the virtual and real amplitudes finite, an appropriate infrared counterterm  $\mathcal{C}_{n+1}$  acting on the  $(n+1)$ -particle phase space is subtracted from the real amplitude and added back again to the virtual amplitude. The counterterm  $\mathcal{C}_{n+1}$  must be chosen such that it cancels the soft and collinear singularities of the real amplitude and that it can be integrated analytically over the one-particle phase space  $d\Phi_1$ :

$$\begin{aligned}\sigma_{\text{NLO}} &= \int d\Phi_n [\mathcal{B}_n + \mathcal{V}_n] + \int d\Phi_{n+1} \mathcal{R}_{n+1} \\ &= \int d\Phi_n \left[ \mathcal{B}_n + \mathcal{V}_n + \int d\Phi_1 \mathcal{C}_{n+1} \right] + \int d\Phi_{n+1} [\mathcal{R}_{n+1} - \mathcal{C}_{n+1}]\end{aligned}\quad (2.54)$$

To determine the counterterm  $\mathcal{C}_{n+1}$  the infrared poles of the real amplitudes have to be extracted. This highly non-trivial task is achieved by the FKS method by splitting the real amplitude into regions with at most one single soft-collinear singular configuration each. The splitting of the phase space is done with a suitable measurement function  $\mathcal{S}$  [129] which has the following infrared behavior

$$\mathcal{S}_{n+1}(p_a, p_b, p_1, \dots, (1-z)p_n, zp_n) = \mathcal{S}_n(p_a, p_b, p_1, \dots, p_n) \quad \text{for } 0 \leq z \leq 1. \quad (2.55)$$

As always,  $p_a$  and  $p_b$  denote the momenta of the initial state and  $p_i$  ( $i = 1, \dots, n+1$ ) are the final-state partons of the real correction. This measurement function is used to relate partonic final-state configurations to experimental observables like jets. The measurement function ensures that the observable is infrared safe, meaning in particular that in the soft or collinear limit the  $n+1$  particle configuration leads to the same physical result as the  $n$  particle configuration where two particles merge or one particle is removed from an external leg. By definition, the simplest example of an infrared safe observable is the total cross section where  $\mathcal{S} = 1$ .

By mapping the  $n$  final-state partons to  $n$  jets, we obtain the partonic cross section

## Theoretical Background

of the Born and virtual part,

$$\sigma_{\mathcal{B}+\mathcal{V}} = \int d\Phi_n \mathcal{M}_n \mathcal{S}_n, \quad (2.56)$$

or similarly for the real part of the cross section

$$\sigma_{\mathcal{R}} = \int d\Phi_{n+1} \mathcal{R}_{n+1} \mathcal{S}_{n+1}. \quad (2.57)$$

For simplicity, we have combined the Born and virtual amplitude into a common matrix element  $\mathcal{M}_n \equiv \mathcal{B}_n + \mathcal{V}_n$ . By a clever decomposition of the measurement function  $\mathcal{S}_{n+1}$  for the  $n+1$  final-state particles of the real contribution and defining its behavior in the vicinity of a singular region, namely

$$\mathcal{S}_{n+1} = \sum_{i=1}^{n+1} \left( \mathcal{S}_i + \sum_{\substack{j=1 \\ j \neq i}}^{n+1} \mathcal{S}_{ij} \Theta(p_{T,i}^2 - p_{T,j}^2) \right) \quad (2.58)$$

and

$$\begin{aligned} \mathcal{S}_i \neq 0 & \quad \text{only if} \quad E_i \rightarrow 0, \quad \vec{p}_a \parallel \vec{p}_i, \quad \vec{p}_b \parallel \vec{p}_i, \\ \mathcal{S}_{ij} \neq 0 & \quad \text{only if} \quad E_i \rightarrow 0, \quad E_j \rightarrow 0, \quad \vec{p}_i \parallel \vec{p}_j, \end{aligned} \quad (2.59)$$

the real contribution  $\sigma_{\mathcal{R}}$  splits into a sum of terms each of which has one soft-collinear singularity at most. Additionally, only the infrared limits of  $\mathcal{S}_i$  and  $\mathcal{S}_{ij}$  are important, meaning that these function can be redefined up to terms which vanish in the infrared limits. By inserting Eq. (2.58) into Eq. (2.56) and Eq. (2.57), and following Ref. [124], we obtain the infrared finite cross section which is now split into a sum of an  $n$  particle and  $n+1$  particle contribution,

$$\sigma_{\text{NLO}} = \sigma_{\text{NLO}}^n + \sigma_{\text{NLO}}^{n+1}. \quad (2.60)$$

This procedure requires no algebraic computation and it can be implemented such that it does not depend on a specific jet algorithm. The FKS subtraction method is perfectly suitable for any Monte Carlo integrator such as the POWHEG-BOX.

## 2.4 Resummation and parton showers

To simulate the final-states of a hadron collision in full detail down to the level of particles with very low energies, a shower Monte Carlo (SMC) generator is used. During the scattering process, color-charged particles like quarks and gluons can radiate further color-charged particles. This radiation is generally suppressed by a order of the strong coupling  $\alpha_s$ . However, for specific kinematic regions the probability of emitting further particles is enhanced by a logarithmic factor which can easily exceed the suppression by the strong coupling constant. By summing up the leading-logarithms (LL) to all orders, parton showers (PS) can give an estimate of higher-order effects and therefore improve the fixed-order calculation. Even if we were able to evaluate Feynman diagrams at arbitrary order, we could not account for exclusive quantities. This is why a PS is not only a handy addition to improve the calculation, but even a necessity when calculating certain observables.

A shower of color-charged particles in the LL picture can be viewed as a sequence of  $1 \rightarrow 2$  branchings  $a \rightarrow bc$ , where  $a$  is the mother particle and  $b, c$  are daughter particles. The SMC algorithm starts from the kinematic configuration of the hard scattering process which is usually an exact  $2 \rightarrow 2$  LO or NLO computation. Then the SMC program increases the final-state multiplicity iteratively by attaching additional partons to the color-charged initial and final-state partons. Since the momenta of all particles, including the initial-state particles, have to be reshuffled (restoration of momentum conservation and applying on-shell conditions  $p_a^2 = 0$  after branching), SMC programs can in principal affect observables of particles that are not even color-charged.

The branching simulated by an SMC algorithm conserves flavor and four momentum locally and it respects unitarity which simply means that a parton may or may not undergo a branching into two new partons. We want to derive the Sudakov form factor in the following which is the basis of every SMC algorithm. The Sudakov form factor  $\Delta_a$  approximates higher-order effects by summing up collinear emissions from external legs. Therefore, the Sudakov form factor improves a fixed-order calculation in the collinear limit.

In the limit of small branching angles of a process  $a \rightarrow bc$ , as depicted in Fig. 2.9, we have for the scale  $Q$  and the branching angle  $\theta$  of the process

$$Q = \theta_1 z E = \theta_2 (1 - z) E, \quad (2.61)$$

$$\theta = \frac{\theta_1}{1 - z} = \frac{\theta_2}{z}. \quad (2.62)$$

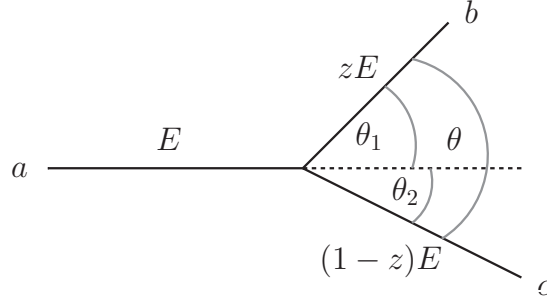


Figure 2.9: The kinematic variables for a branching of a particle with energy  $E$  into two particles with energy fraction  $zE$  and  $(1-z)E$  in the collinear limit.

$E$  is the energy of the (massless) mother particle. We define  $z$  in the collinear limit as the momentum fraction carried away by the parton  $b$  and  $t = E^2\theta^2$  as the energy scaled branching angle squared, although the choice of the kinematic variables  $z$  and  $t$  could differ with different shower algorithms. The variables  $z$  and  $t$  are connected by the condition

$$z(1-z)\sqrt{t} > \frac{\sqrt{t_0}}{4}, \quad (2.63)$$

where  $t_0 = E_0^2\theta^2$  is the minimal energy squared, either defined as the minimal detector resolution or the scale when non-perturbative effects take over.

The probability  $dP$  of a parton branching into two new partons is related to the unregularized Altarelli-Parisi splitting function (kernel)  $\hat{P}$  [130],

$$dP_a \equiv F_a(z, t) dz dt = \sum_b \frac{\alpha_s(Q)}{2\pi} \hat{P}_{ba}(z) \frac{dt}{t} dz. \quad (2.64)$$

The regularized splitting functions can be found for example in the Appendix of Ref. [116].

The splitting kernels have different definitions in regard to the splitting process, and are given by

$$\begin{aligned} \hat{P}_{qq}(z) &= C_F \frac{1+z^2}{1-z}, \\ \hat{P}_{gg}(z) &= N_C \frac{(1-z(1-z))^2}{z(1-z)}, \\ \hat{P}_{qg}(z) &= T_F (z^2 + (1-z)^2), \\ \hat{P}_{gq}(z) &= C_F \frac{1+(1-z)^2}{z}, \end{aligned} \quad (2.65)$$



where  $N_C = 3$ ,  $C_F = 4/3$ ,  $T_F = N_f/2$  and  $N_f$  equals the number of active flavors. Note, that the regularized splitting kernels  $P$  defined in Ref. [116] differ from the unregularized splitting kernels  $\hat{P}$  given here by delta- and „+“ distributions. We have omitted the delta-distributions as energy and flavor conservation are trivially fulfilled at every vertex for any SMC generator. Additionally, the „+“ distributions are not needed since a cutoff in the SMC algorithm on the allowed  $z$  range avoids singular regions where very soft gluons can be produced excessively.

Let  $\Delta_a(t_I, t_0)$  be the probability that no branching of a parton  $a$  into partons  $b, c$  has taken place between the initial scale  $t_I$  and the final scale  $t_0$ . Unitarity requires now that the sum of the probability  $\Delta_a(t_I, t_0)$  and the probability that the parton splits into the partons  $b, c$  if no splitting occurred previously is equal to one, meaning

$$1 = \Delta_a(t_I, t_0) + \int_{t_0}^{t_I} \Delta_a(t_I, t) F(z, t) dt dz \quad (2.66)$$

$$= \Delta_a(t_I, t_0) + \sum_b \int_{t_0}^{t_I} \frac{dt}{t} \int dz \Delta_a(t_I, t) \frac{\alpha_s(t)}{2\pi} \hat{P}_{ba}(z). \quad (2.67)$$

This integral equation can be solved iteratively. We get, after rewriting Eq. (2.66) and inserting the equation  $n$  times into itself

$$\begin{aligned} \Delta_a(t_I, t_0) &= 1 - \int_{t_0}^{t_I} dt \Delta_a(t_I, t) F(z, t) dz \\ &= 1 - \int_{t_0}^{t_I} dt_1 F(z, t_1) dz + \int_{t_0}^{t_I} dt_1 \int_{t_1}^{t_I} dt_2 \Delta_a(t_I, t_2) F(z_2, t_2) dz_2 F(z_1, t_1) dz_1 \\ &= \dots \\ &= 1 - \int_{t_0}^{t_I} dt_1 F(z, t_1) dz + \int_{t_0}^{t_I} dt_1 \int_{t_1}^{t_I} dt_2 F(z_2, t_2) dz_2 F(z_1, t_1) dz_1 + \dots \\ &\quad + (-1)^n \int_{t_0}^{t_I} dt_1 \int_{t_1}^{t_I} dt_2 \dots \int_{t_{n-1}}^{t_I} dt_n F(z_1, t_1) dz_1 F(z_2, t_2) dz_2 \dots F(z_n, t_n) dz_n \\ &\quad + \mathcal{O}(n+1). \end{aligned} \quad (2.68)$$

We then use the relation

$$\int_{t_0}^{t_I} dt_1 \int_{t_1}^{t_I} dt_2 \dots \int_{t_{n-1}}^{t_I} dt_n f(t_1) f(t_2) \dots f(t_n) = \frac{1}{n!} \left[ \int_{t_0}^{t_I} dt f(t) \right]^n \quad (2.69)$$

## Theoretical Background

which simplifies the expression to

$$\begin{aligned}\Delta_a(t_I, t_0) &= \sum_{n=0}^{\infty} \frac{1}{n!} \left[ - \int_{t_0}^{t_I} dt F(z, t) dz \right]^n \\ &= \exp \left[ - \int_{t_0}^{t_I} dt F(z, t) dz \right].\end{aligned}\tag{2.70}$$

This leads to the Sudakov form factor which resums the LL contributions to all orders

$$\Delta_a(t, t_0) = \exp \left[ - \sum_b \int_{t_0}^t \frac{dt'}{t'} \int dz \frac{\alpha_s(t')}{2\pi} \hat{P}_{ba}(z) \right].\tag{2.71}$$

In detail, the SMC generator chooses a random number  $\delta$  between 0 and 1 and solves the equation  $\Delta_a(t, t_0) = \delta$  for  $t$ . Then it randomly chooses an azimuthal angle  $\phi \in [0, 2\pi]$  and generates the variable  $z$  according to the distribution  $F(z, t)$  which determines all kinematical variables of partons  $b$  and  $c$ . This process is repeated for the partons  $b$  and  $c$  with the constraint that the subsequent branching can only take place with a branching angle  $\theta$  less than the previous one. This type of SMC algorithm is called angular ordered shower and is used for example by HERWIG [131].

Since SMC algorithms still rely on perturbation theory, the simulation of PS is only valid above a certain hadronic scale which is usually of order  $E_0 \approx 1\text{GeV}$ . Effects at an energy scale below this hadronic scale, for example hadronization effects, need special treatment. For the phenomenological description of hadronization so-called fragmentation functions (FF) are used which are similar to parton distribution functions, except that they are defined for the final states of the collision. These fragmentation functions have to be parametrized and fitted to data. After the DGLAP equations with time-like kernels are applied [132], the FF can be evaluated at any given scale. Note that the time-like kernels are identical to the space-like splitting kernels (defined in Eqs. (2.65)) at the leading-log level, which is known as the Gribov-Lipatov relation [114].

## 2.5 Combining NLO corrections with PS

Improving a next-to-leading order calculation in association with an SMC program beyond LL accuracy is a difficult endeavor. Not only modifying existing huge and complex SMC codes would be necessary, but several other problems would have to be overcome. For example, the shower would have to be improved to next-to-leading logarithm (NLL) accuracy in the collinear and soft limit. Sticking to the LL approximation of a given SMC program and improving inclusive observables with NLO accuracy is often the easier choice.

The so-called MC@NLO method [133] is based on this idea. A given NLO result has to be carefully prepared to match certain features of the SMC program. In particular, the approximate SMC results have to be subtracted from the NLO result to avoid double counting. At leading-log level an SMC program generates contributions equal to real-emission diagrams in the collinear limit. If we would add an SMC naively to an NLO calculation, these parts would occur twice.

However, the MC@NLO method has additional drawbacks. For example, the method is specific to the particular SMC program used, and different SMC algorithms would require evaluating again the approximate SMC results completely.

A simpler way is provided by the POWHEG method (POsitive Weight Hardest Emission Generator) which was originally described in Ref. [130]. Further discussion can be found in Ref. [134]. The key idea of the POWHEG approach is the following. Instead of using the Altarelli-Parisi splitting kernels, the POWHEG approach aims at generating the hardest emission according to the ratio of the real and the Born amplitude first. The observable obtained by multiplying a modified Sudakov form factor is passed to a PS that is ordered in the transverse momentum  $p_T$ . This ensures that no contribution occurs twice. For completeness of this thesis, we want to give a short overview of the POWHEG method here. The discussion in full detail can be found in Ref. [134].

We want to observe how an NLO observable  $\mathcal{O}$  is influenced by the PS and what has to be done, so that no term contributes twice if the PS is attached. The expectation value of an observable at NLO is given by

$$\begin{aligned} \langle \mathcal{O}_{\text{NLO}} \rangle &= \int d\Phi_n \left[ \mathcal{B}_n + \mathcal{V}_n + \int d\Phi_1 \mathcal{C}_{n+1} \right] \mathcal{O}_n \\ &+ \int d\Phi_{n+1} [\mathcal{R}_{n+1} \mathcal{O}_{n+1} - \mathcal{C}_{n+1} \mathcal{O}_n], \end{aligned} \quad (2.72)$$

## Theoretical Background

where  $d\Phi_n$  and  $d\Phi_{n+1}$  are  $n$ - and  $(n+1)$ -particle phase spaces,  $\mathcal{B}_n$  and  $\mathcal{V}_n$  are the Born and virtual amplitudes that are defined on the  $n$ -particle phase space, and  $\mathcal{R}_{n+1}$  is the real amplitude with  $n+1$  final-state particles.  $\mathcal{C}_{n+1}$  is a counterterm chosen such that the IR singularities are subtracted from the real amplitude. Details on the subtraction scheme used by the POWHEG-BOX can be found in Sec. 2.3.2.

The observables  $\mathcal{O}_n$  and  $\mathcal{O}_{n+1}$  are again defined on the  $n$ - and  $(n+1)$ -particle phase spaces. In particular, we would choose  $\delta$  distributions for  $\mathcal{O}_n$  and  $\mathcal{O}_{n+1}$  if we want to extract a certain expectation value, i.e.  $\mathcal{O}_2 = \delta(m^2 - (p_1 + p_2)^2)$  would lead to the cross section  $d\sigma/dm^2$  differential in the invariant mass of the final-state particles  $p_1$  and  $p_2$ .

Similar to Eq. (2.66) we split the expectation value into a part where no emission up to a given scale  $t_0$  took place and into a part with an additional emission

$$\langle \mathcal{O}^{\text{PS}} \rangle = \int d\mathcal{O}_n \Delta(t_0) + \int d\mathcal{O}_{n+1} \Delta(t_I) F + \mathcal{O}(\alpha_s^2) \quad (2.73)$$

Applied to the NLO observable and expanding in  $\alpha_s$  yields

$$\begin{aligned} \langle \mathcal{O}_{\text{NLO}}^{\text{PS}} \rangle &= \int d\Phi_n \left[ \mathcal{B}_n + \mathcal{V}_n + \int d\Phi_1 \mathcal{C}_{n+1} \right] \mathcal{O}_n \\ &\quad - \int d\Phi_{n+1} \mathcal{B}_n F \mathcal{O}_n + \int d\Phi_{n+1} \mathcal{B}_n F \mathcal{O}_{n+1} \\ &\quad + \int d\Phi_{n+1} [\mathcal{R}_{n+1} \mathcal{O}_{n+1} - \mathcal{C}_{n+1} \mathcal{O}_n]. \end{aligned} \quad (2.74)$$

This naive matching of the PS to the formula for the NLO observable leads at the leading-log level to collinear terms that are already described by the real amplitude. In order to avoid this problem we define a subtracted NLO expectation value

$$\begin{aligned} \langle \mathcal{O}_{\text{NLO}}^{\text{sub}} \rangle &= \int d\Phi_n \left[ \mathcal{B}_n + \mathcal{V}_n + \int d\Phi_1 \mathcal{C}_{n+1} \right] \mathcal{O}_n \\ &\quad + \int d\Phi_{n+1} [\mathcal{B}_n F - \mathcal{C}_{n+1}] \mathcal{O}_n \\ &\quad + \int d\Phi_{n+1} [\mathcal{R}_{n+1} - \mathcal{B}_n F] \mathcal{O}_{n+1}. \end{aligned} \quad (2.75)$$

The above formula can be simplified for the first emission if for the splitting function  $F = \mathcal{R}_{n+1}/\mathcal{B}_n$  instead of the Altarelli-Parisi splitting kernels of Eqs. (2.65) are chosen. Then the subtracted NLO observable reads

$$\langle \mathcal{O}_{\text{NLO}}^{\text{sub}} \rangle = \int d\Phi_n \left[ \mathcal{B}_n + \mathcal{V}_n + \int d\Phi_1 \mathcal{C}_{n+1} \right] \mathcal{O}_n + \int d\Phi_{n+1} [\mathcal{R}_{n+1} - \mathcal{C}_{n+1}] \mathcal{O}_n \quad (2.76)$$

which is used to match the PS with. Eq. (2.76) is similar to Eq. (2.72). However, the hardest emission is now generated with the  $p_T$  ordered Sudakov factor where

the splitting function is replaced by  $F = \mathcal{R}_{n+1}/\mathcal{B}_n$

$$\Delta(p_T) = \exp \left[ - \int d\Phi_1 \frac{\mathcal{R}_{n+1}}{\mathcal{B}_n} \Theta(p_T^n - p_T^{n+1}) \right]. \quad (2.77)$$

We obtain the POWHEG master formula from Eq. (2.73) and Eq. (2.76) together with the  $p_T$  ordered Sudakov factor:

$$\sigma = \int d\Phi_n \tilde{\mathcal{B}}_n \Delta(p_T^{\min}) + \int d\Phi_{n+1} \tilde{\mathcal{B}}_n \Delta(p_T) \frac{\mathcal{R}_{n+1}}{\mathcal{B}_n} \Theta(p_T^n - p_T^{n+1}), \quad (2.78)$$

where

$$\tilde{\mathcal{B}}_n = \left[ \mathcal{B}_n + \mathcal{V}_n + \int d\Phi_1 \mathcal{C}_{n+1} \right] + \int d\Phi_1 [\mathcal{R}_{n+1} - \mathcal{C}_{n+1}] \quad (2.79)$$

comprises all the elements of a calculation at NLO accuracy.

### 2.5.1 The POWHEG-BOX

The simplest way to implement the POWHEG-method for an fixed-order calculation is to use the POWHEG-BOX<sup>9</sup>. Besides many other SM and SUSY processes, the code for weakino-pair and weakino-pair plus jet can be found in the publicly available repository. A lot of the features described above, including the POWHEG master formula, are process independent and therefore can be combined in an easy-to-use common FORTRAN framework. The developer of processes of the POWHEG-BOX is responsible for providing a phase space parametrization, the flavor structure, parameter handling, color matrix elements and the process dependent Born, virtual and real matrix elements squared [104]. If the process is more advanced, as for the case of weakino-pair production, additional modifications and matrix elements are necessary, which will be discussed in the next chapter. The FORTRAN routines for the phase space parametrization are built similarly to Sec. 2.2.1. Dedicated phase spaces of high multiplicity can be obtained easily by the subroutines defined there. Examples for a two, three and four-particle phase space are shown in App. D.

### 2.5.2 Parallelization of the POWHEG-BOX

The POWHEG-BOX is capable of running several computations of the same integral in parallel, thus reducing the overall evaluation time by the cost of using multiple CPU cores. This feature comes in handy when the serial computation of complicated processes on only one core needs too much time. The event generation with the POWHEG-BOX in parallel mode is divided into four stages [135]:

---

<sup>9</sup><http://powhegbox.mib.infn.it>

## Theoretical Background

- Stage 1: The importance sampling grids for the calculation of the  $\tilde{B}$  function and remnant contributions<sup>10</sup> are set up. To obtain smoother grids, it is sometimes necessary to iterate this stage several times.
- Stage 2: The NLO cross section is computed, and upper bounding envelopes of the  $\tilde{B}$  function, as well as remnants contributions are set up, to be used for the unweighted generation of underlying Born and remnant configurations.
- Stage 3: The bounding envelopes for the generation of the hardest radiation from given underlying Born events are set up.
- Stage 4: Events in the Les Houches standard format [136] are generated.

Additionally, the POWHEG-BOX features a reweighting mechanism which could be used to adapt the events generated in stage 4 to different parameter setups, i.e. different PDF or renormalization/factorization scale sets, hence reducing the time consuming computation of the NLO cross section. If the execution time is also dominated by the virtual amplitudes events can be generated without them at first. The virtual amplitudes can be added back later by reweighting at the end of stage 4.

To simplify the setup and initialization of parallel jobs a script can be used. The `runparallel.sh` script can be found in the publicly available repository of the POWHEG-BOX, in the subdirectories of weakino-pair and jet production. The script is capable of setting up all needed parameters of all single stages, including the integration and reweighting parameters. Before continuing with the next stage, all the jobs of the previous stage have to be completed. Therefore, the script waits until the previous stage has finished and then follows to submit the jobs of the subsequent stage. Examples of how to set up and run the POWHEG-BOX, and how to use the `runparallel.sh` script can be found in App. A, App. B and App. C, respectively.

---

<sup>10</sup>Remnant contributions are the real matrix element without the singular contributions.

### 3 Weakino-pair and weakino-pair plus jet production at hadron colliders

In this chapter, we focus on the calculation of weakino-pair and weakino-pair plus jet production and the setup of these processes in the framework of the POWHEG-BOX<sup>1</sup> [130, 134]. The FORTRAN code of the weakino-pair and weakino-pair plus jet projects can be directly downloaded from the website of the POWHEG-BOX or from <https://github.com/MKesenheimer/weakinos> or <https://github.com/MKesenheimer/weakinos-jet>, respectively. The details of the code structure will be discussed in App. A.

The following discussions and results are based on two publications, Refs. [137, 138]. Although the general outline of our calculations is sketched there, we want to give a more detailed overview here. We discuss the relevant Born, virtual and real diagrams and how to obtain these diagrams with the help of computer algebra programs such as FORMCALC [139] and FEYNARTS [140]. We also show the diagrams for the renormalization conditions which are necessary to render the virtual contributions ultraviolet finite.

Furthermore, an important part of the calculation is the treatment of single and double on-shell resonances which occur in the real matrix elements (see Sec. 2.2) for both weakino-pair and weakino-pair plus jet production. These resonances are responsible for a bad convergence of the perturbative expansion and thus have to be subtracted in a sophisticated way. The counterterms for the on-shell subtraction and the requirement for the matrix elements that have to be met are given in the following sections.

Finally, we give the phenomenological results of weakino-pair and weakino-pair plus jet production. We examine different MSSM parameter points with conserved  $R$ -parity (c.f. Sec. 1.4.5) which implies that SUSY particles are produced in pairs and that decays will always result in at least one stable LSP. The most relevant phe-

---

<sup>1</sup><http://powhegbox.mib.infn.it>

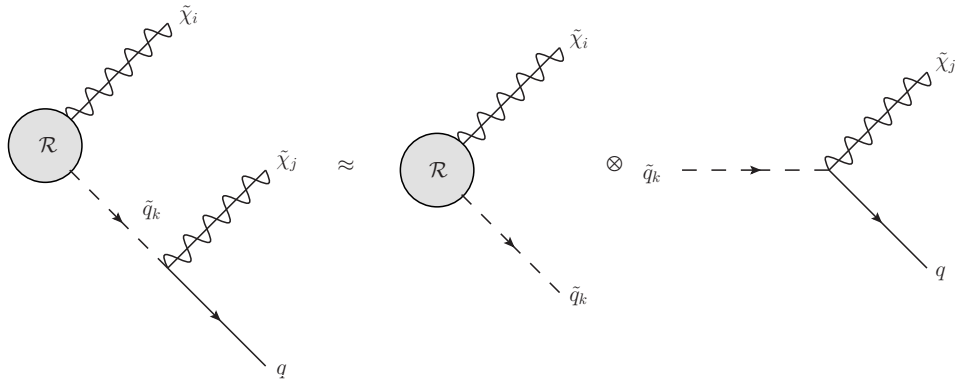


Figure 3.1: In the narrow width approximation (NWA) the production of the final states  $\tilde{\chi}_i \tilde{\chi}_j q$  via an intermediate squark being on its mass shell with natural width  $\Gamma_{\tilde{q}}$  can be interpreted as the production of  $\tilde{\chi}_i \tilde{q}_k$  followed by the squark decay  $\tilde{q}_k \rightarrow q \tilde{\chi}_j$ .

nomenological observables are mono-jet and missing-energy signatures. Therefore, our phenomenological analysis is focused on these observables.

### 3.1 On-shell resonances - overview

In the following we will discuss common features of weakino-pair and weakino-pair plus jet production. As it turns out, subtleties arise in the calculation of physically meaningful observables of these two processes by the occurrence of on-shell resonant diagrams in the real-emission corrections. These resonances appear because new channels open up in the real corrections which vastly dominate the real contributions for certain phase space regions. The new channels do not occur at Born level. Therefore, they can be seen as a subset of a complete (and different) tree-level calculation rather than the genuine perturbative corrections to the weakino-pair production and weakino+jet production processes we are considering. For the processes  $pp \rightarrow \tilde{\chi}_i \tilde{\chi}_j$  and  $pp \rightarrow \tilde{\chi}_i \tilde{\chi}_j + \text{jet}$  different channels with potential on-shell resonances contribute. We only have to deal with single on-shell resonances for the simpler pair-production process of two weakinos. However, for weakino-pair plus jet production singly and doubly resonant structures have to be regularized. The relevant channels are subprocesses of the type  $qg \rightarrow \tilde{\chi}_i \tilde{\chi}_j q'$  for weakino-pair and of the type  $q\bar{q}' \rightarrow \tilde{\chi}_i \tilde{\chi}_j q\bar{q}'$  or  $gg \rightarrow \tilde{\chi}_i \tilde{\chi}_j q\bar{q}'$  for weakino-pair plus jet production.



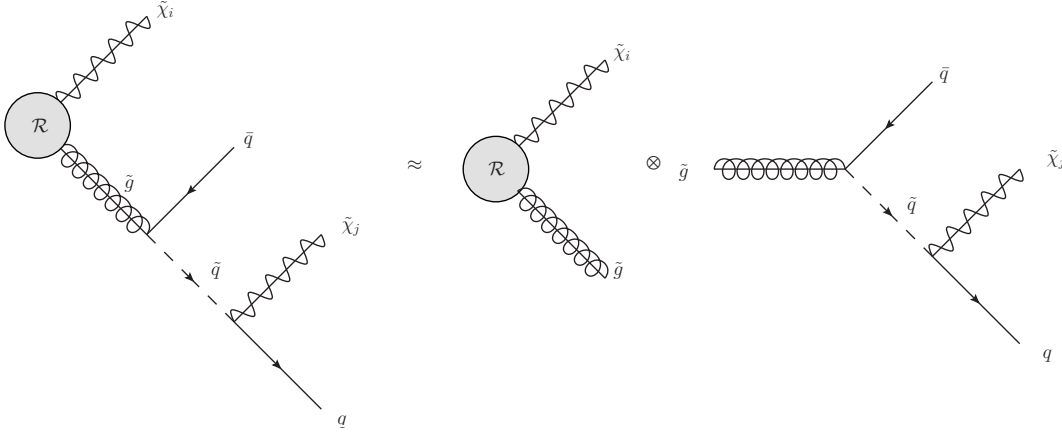


Figure 3.2: For the process  $pp \rightarrow \tilde{\chi}_i \tilde{\chi}_j + \text{jet}$  additional gluino resonances can contribute to the real matrix element. Note that the first diagram includes a further squark on-shell single resonance that must not be subtracted for weakino-pair plus jet production since this resonance occurs already at Born level. Diagrams which contain a singly resonant squark are regulated by the complex mass scheme (c.f. Sec. 2.2.7) and are therefore not problematic.

Fortunately, the problematic contribution of these new channels can be seen as the tree-level contribution of an on-shell particle production followed by a decay. The (quasi) on-shell decay into the respective daughter particles is allowed if the mother particle is sufficiently heavy. See Fig. 3.1 and Fig. 3.2 for the interpretation of these contributions in the narrow width approximation (NWA).

Since the cross section of the tree-level contribution with subsequent decay of a final-state particle can be accounted to a different production process, we can remove the on-shell contributions which renders our result finite and well-defined. If we would sum over all possible production processes at NLO and no on-shell subtraction would be applied, these contribution would occur both in the tree-level production of  $\tilde{q}_k \tilde{\chi}_i$  and in the real-emission contributions of  $\tilde{\chi}_i \tilde{\chi}_j$  production, thus leading to the double counting of these contributions. Therefore, we have to remove them from the continuum  $pp \rightarrow \tilde{\chi}_i \tilde{\chi}_j (+j)$  ensemble in our calculation.

As an additional remark, albeit being relatively uncommon, problematic on-shell resonances are not solely a property of supersymmetric pair-production processes. On-shell resonance can also occur in processes of the Standard Model. They are, for

example, discussed in  $tW$  and  $tWH$  [141, 142], and  $tH$  production [143].

### 3.1.1 Subtraction of on-shell resonances

To get rid of the troublesome on-shell resonances many strategies can be applied. Consider the matrix element  $\mathcal{M}$  (including on-shell resonant diagrams) which can be split into a non-resonant (regular)  $\mathcal{M}_{\text{reg}}$  and a resonant part  $\mathcal{M}_{\text{res}}$ , meaning  $\mathcal{M} = \mathcal{M}_{\text{reg}} + \mathcal{M}_{\text{res}}$ . The matrix element squared is then given by

$$|\mathcal{M}|^2 = |\mathcal{M}_{\text{reg}}|^2 + |\mathcal{M}_{\text{res}}|^2 + 2\text{Re} \left[ \mathcal{M}_{\text{reg}}^* \mathcal{M}_{\text{res}} \right]. \quad (3.1)$$

The simplest method to remove the resonant contributions is to neglect all potentially dangerous diagrams which is known as *diagram removal type I* (DRI). Thus, the matrix element is reduced to

$$|\mathcal{M}^{\text{DRI}}|^2 = |\mathcal{M}_{\text{reg}}|^2. \quad (3.2)$$

If only the matrix element squared of the resonant diagrams is removed and the interference contribution with non-resonant diagrams is kept, the method is called *diagram removal type II* (DRII) and the matrix element is then given by

$$|\mathcal{M}^{\text{DRII}}|^2 = |\mathcal{M}_{\text{reg}}|^2 + 2\text{Re} \left[ \mathcal{M}_{\text{reg}}^* \mathcal{M}_{\text{res}} \right]. \quad (3.3)$$

Although the effects could be small, removing diagrams from a gauge-invariant set of diagrams breaks gauge invariance and is therefore not suitable for the most general case. Additionally, removing interference and off-shell contributions is the least preferable choice one should make when calculating physically meaningful results. A better solution is the diagram subtraction scheme (DSUB), where a counterterm is introduced to subtract only the on-shell contributions of the resonant diagrams locally.

We note that the on-shell subtraction procedure has the advantage of numerical stability, but may also violate gauge invariance in its most general form. In order to overcome this drawback alternative methods have been explored in the literature, see for instance Ref. [144], but were found to exhibit other disadvantages such as the requirement of artificial cuts, and also being quite involved in a MADGRAPH-based implementation of the real corrections. As we will see in Sec. 3.2.3 and Sec. 3.3.4 gauge-invariance violating contributions of the DSUB methods are not only small but also under control with a single parameter as in the case of weakino-pair production. For weakino-pair plus jet production gauge invariance is already preserved by the counterterm for double on-shell contributions.

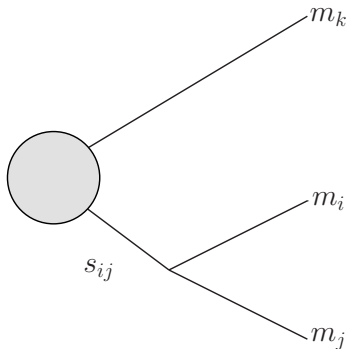


Figure 3.3: Three particle kinematics of the single on-shell resonances for the process  $pp \rightarrow \tilde{\chi}_i \tilde{\chi}_j$ .

The DSUB scheme is more involved to implement than DRI or DRII and additional hurdles have to be overcome. For example, the subtracted on-shell contributions have to be integrated over a separate phase space and no sophisticated scheme for the subtraction of double resonances, as in the case of  $pp \rightarrow \tilde{\chi}_i \tilde{\chi}_j + \text{jet}$ , has been formulated yet. However, these few drawbacks are more than compensated by the advantages of the DSUB scheme. The interference terms and the off-shell contributions of  $\mathcal{M}_{\text{res}}$  are retained and, by construction, the DSUB scheme allows for a pointwise subtraction which is perfectly suitable for a Monte Carlo implementation.

The DSUB method was first applied in PROSPINO [101], and more recently has been adapted for the code structure of the POWHEG-BOX [141, 144]. More specifically, we extend the procedure developed for the related case of squark-pair production in the POWHEG-BOX [144, 145] to the richer resonance structure of weakino-pair production and weakino-pair plus jet processes, as more diagrams are involved in these cases.

A counterterm that mimics the correct on-shell behavior of the matrix element have to be formulated and subtracted from the real matrix element. To this end, we define a general particle production process with spectators  $k$  and intermediate particles  $(ij)$  that can cause on-shell resonances. This particle production can be divided into two distinct processes. First, the spectators  $k$  and the intermediate particles are produced. Thus, we have for the momenta of the first process:  $p \rightarrow \sum_{(ij)} p_{ij} + \sum_k p_k$ , where  $p$  is the incoming momentum of the initial-state particles. Second, the (on-shell) intermediate particles split up into the particle pairs  $i$  and  $j$  which means for the momenta  $p_{ij} \rightarrow p_i + p_j$ . More information about the relevant

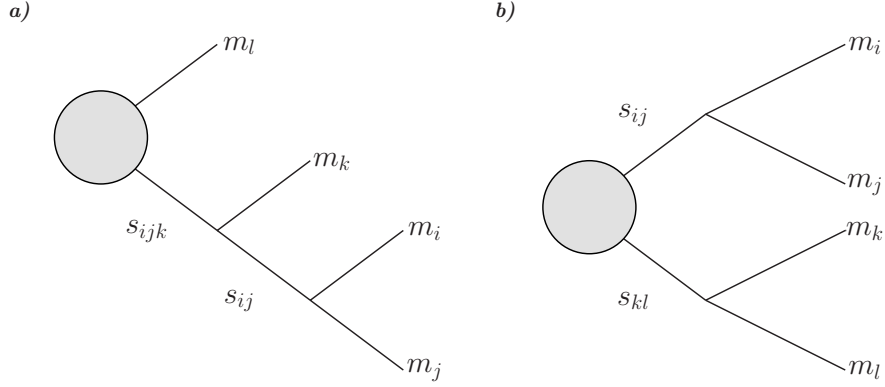


Figure 3.4: Kinematic of the resonant structures for  $2 \rightarrow 4$  processes. For the process  $pp \rightarrow \tilde{\chi}_i \tilde{\chi}_j + \text{jet}$  the topology (a) gives rise to gluino singly resonant and topology (b) to squark doubly resonant contributions.

topologies in Fig. 3.3 and Fig. 3.4.

The general on-shell counterterm is formulated in such a way that the resonances generated by the intermediate particle ( $ij$ ) are subtracted. Generalizing the on-shell counterterm for DSUB introduced in Ref. [146], we obtain

$$\begin{aligned} \left| \mathcal{M}_{\text{res}}^{\text{CT}}(\Gamma_{\text{reg}}) \right|^2 &= \prod_{(ij)} \Theta(s - (m_{ij} + \sum_{k,\text{spec.}} m_k)^2) \Theta(m_{ij} - m_i - m_j) \\ &\times \text{BW} |\mathcal{M}_{\text{res}}(\Gamma_{\text{reg}})|_{\text{remapped}}^2, \end{aligned} \quad (3.4)$$

where the first theta-function guarantees that the partonic energy  $\sqrt{s}$  is higher than the production threshold ( $m_{ij} + \sum_{k,\text{spec.}} m_k$ ) of the on-shell intermediate particle plus further spectator particles. The second product of theta-functions ensures that the intermediate particle has a mass  $m_{ij}$  larger than the sum of the masses of the two particles  $i, j$ . This condition follows directly from the requirement that the particle ( $ij$ ) has to decay on-shell into the particles  $i$  and  $j$ . The Breit-Wigner factor BW approaches 1 for the resonant region and is responsible for suppressing the counterterm in the off-shell case. Furthermore, the Breit-Wigner factor ensures that in the narrow-width approximation for the width of the intermediate particle  $\Gamma_{\text{reg}} \rightarrow 0$  the counterterm reduces to the tree level production of the on-shell particle with a subsequent decay, for instance  $\sigma(pp \rightarrow \tilde{\chi}_a \tilde{\chi}_b q) \approx \sigma(pp \rightarrow \tilde{q}_k \tilde{\chi}_a) \times \text{BR}(\tilde{q}_k \rightarrow q \tilde{\chi}_b)$  for the process  $pp \rightarrow \tilde{\chi}_i \tilde{\chi}_j$ . Further details for the Breit-Wigner factor can be found in Sec. 3.1.2.

The on-shell resonant matrix element squared  $|\mathcal{M}_{\text{res}}(\Gamma_{\text{reg}})|_{\text{remapped}}^2$  has to be eval-

uated with the on-shell kinematics (for instance, requiring  $s_{ij} = m_{ij}^2$  for the intermediate particle  $ij$  decaying into particles  $i$  and  $j$ ). Usually this is achieved by reshuffling the momenta of the final-state particles with an algorithm similar to the momentum reshuffling used by the Catani-Seymour subtraction. See Sec. 3.1.3 for more details.

The technical regulator  $\Gamma_{\text{reg}}$  is introduced in the propagator of the intermediate particle,  $1/(s_{ij} - m_{ij}^2) \rightarrow 1/(s_{ij} - m_{ij}^2 - i\Gamma_{\text{reg}}m_{ij})$ , to regularize the divergent propagator at the on-shell pole  $s_{ij} = m_{ij}^2$ . Here, we define  $s_{ij} = (p_i + p_j)^2$  as the Mandelstam variable that describes the momentum flow through the intermediate particle. We will look into more specific representations of the counterterm in the next sections.

### 3.1.2 Breit-Wigner factor

In the following we will deduce the Breit-Wigner factors which are necessary for the subtraction terms defined in Eq. (3.4) for singly and doubly resonant contributions. The Breit-Wigner factor BW is able to extract only the on-shell resonant contributions from the resonant matrix element  $\mathcal{M}_{\text{res}}$ . Other contributions such as regular or off-shell parts are suppressed by construction.

Let us consider the singly resonant case first. The most general singly resonant on-shell matrix element as sketched in Fig. 3.3 is given by

$$\mathcal{M}_{\text{res}} = \frac{A_0}{\bar{s}_{ij}}, \quad (3.5)$$

where  $A_0$  is regular in regard to the Mandelstam variable  $s_{ij} = (p_i + p_j)^2$  of the intermediate particle. We define  $\bar{s}_{ij} \equiv s_{ij} - m_{ij}^2$  as the reduced Mandelstam variable. The matrix element diverges if  $\bar{s}_{ij} \rightarrow 0$ , or similarly,  $s_{ij} \rightarrow m_{ij}^2$ . To tame the on-shell resonance, the DSUB scheme requires the introduction of a technical regulator  $\Gamma_{\text{reg}}$  which acts as a particle width. By inserting the regulator into the on-shell matrix element, we obtain

$$\mathcal{M}_{\text{res}} = \frac{A_0}{\bar{s}_{ij} + im_{ij}\Gamma_{\text{reg}}}. \quad (3.6)$$

The Breit-Wigner factor can be built by dividing the squared matrix element itself by the squared matrix element taken on-shell, where the resonant propagators  $\bar{s}_{ij} \rightarrow 0$ ,  $\bar{s}_{kl} \rightarrow 0$ :

$$\text{BW} = \frac{|\mathcal{M}_{\text{res}}|^2}{|\mathcal{M}_{\text{res}}|_{\bar{s}_{ij} \rightarrow 0}^2}, \quad (3.7)$$

which results in the Breit-Wigner factor for the singly resonant case,

$$\text{BW} = \frac{m_{ij}^2 \Gamma_{\text{reg}}^2}{\bar{s}_{ij}^2 + m_{ij}^2 \Gamma_{\text{reg}}^2}. \quad (3.8)$$

To generalize this method to the doubly resonant part of a matrix element for the production of particle pairs  $(i, j)$  and  $(k, l)$  as sketched in Fig. 3.4, we examine the resonant matrix element

$$\mathcal{M}_{\text{res}} = B_0 \frac{1}{\bar{s}_{ij}} \times \frac{1}{\bar{s}_{kl}}, \quad (3.9)$$

where  $B_0$  denotes the finite part of the amplitude, and the  $1/\bar{s}_{ab}$  terms represent propagators that can go on-shell. For each pair of external particles  $(a, b)$  we introduce the invariants  $s_{ab} = (p_a + p_b)^2$  and  $\bar{s}_{ab} \equiv s_{ab} - m_{ab}^2$ , where  $m_{ab}$  is the mass of the resonant particle and  $p_a, p_b$  are the four-momenta of the considered external particles. The amplitude  $\mathcal{M}_{\text{res}}$  obviously diverges, if  $\bar{s}_{ij}$  or  $\bar{s}_{kl}$  approach zero.

The first natural attempt to introduce a regulator width for this matrix element would be equivalent to the singly resonant case where we would replace  $\bar{s}_{ij}$  with  $\bar{s}_{ij} + im_{ij}\Gamma_{\text{reg}}$  resulting in the regulated matrix element

$$\mathcal{M}_{\text{res}} = B_0 \frac{1}{\bar{s}_{ij} + im_{ij}\Gamma_{\text{reg}}} \times \frac{1}{\bar{s}_{kl} + im_{kl}\Gamma_{\text{reg}}}. \quad (3.10)$$

Next, a counterterm equivalent to the one in Eq. (3.4) has to be formulated where the BW-factor can be obtained similar to the singly resonant case. Unfortunately, it turns out that the on-shell contribution to the cross section  $\sigma_{\text{real}}^{\text{OS}}$  naively obtained from Eq. (3.10) depends heavily on  $\Gamma_{\text{reg}}$  which should not be the case for a proper regulator insertion. However, one can use the partial fraction decomposition identity  $1/(xy) = 1/(x+y)(1/x + 1/y)$  to rewrite the resonant matrix element as

$$\mathcal{M}_{\text{res}} = \frac{B_0}{\bar{s}_{ij} + \bar{s}_{kl}} \times \left( \frac{1}{\bar{s}_{ij}} + \frac{1}{\bar{s}_{kl}} \right), \quad (3.11)$$

effectively dividing the resonance structure into two single resonances which can be treated separately. Since the resonance structure of the second factor appears already at Born level and problematic resonances are tamed by the complex mass scheme in the Born amplitudes (for details see Sec. 2.2.7 and the discussion in Sec. 3.3), we need to insert a regulator width only for the first term, using the same regulator for  $(i, j)$  and  $(k, l)$ . The regulated matrix element after inserting the on-shell regulator  $\Gamma_{\text{reg}}$  reads:

$$\mathcal{M}_{\text{res}} = \frac{B_0}{\bar{s}_{ij} + \bar{s}_{kl} + im_{ij}\Gamma_{\text{reg}} + im_{kl}\Gamma_{\text{reg}}} \times \left( \frac{1}{\bar{s}_{ij}} + \frac{1}{\bar{s}_{kl}} \right). \quad (3.12)$$

In order to comply with the treatment of single resonances that already occur at Born level, additionally the physical decay widths  $\Gamma_{ij}$  and  $\Gamma_{kl}$  of the resonant particles have to be taken into account. The regulated matrix element can then be written as

$$\mathcal{M}_{\text{res}} \equiv \mathcal{P}(\bar{s}_{ij}, \bar{s}_{kl}) B_0, \quad (3.13)$$

where  $\mathcal{P}$  is the regulated propagator structure of the amplitude and is given by

$$\begin{aligned} \mathcal{P}(\bar{s}_{ij}, \bar{s}_{kl}) &= \frac{1}{\bar{s}_{ij} + \bar{s}_{kl} + im_{ij}(\Gamma_{\text{reg}} + \Gamma_{ij}) + im_{kl}(\Gamma_{\text{reg}} + \Gamma_{kl})} \\ &\times \left( \frac{1}{\bar{s}_{ij} + im_{ij}\Gamma_{ij}} + \frac{1}{\bar{s}_{kl} + im_{kl}\Gamma_{kl}} \right). \end{aligned} \quad (3.14)$$

Following the procedure of Ref. [137], the calculation of a suitable counter-term for a resonant matrix element requires the determination of a Breit-Wigner factor that can be built by dividing the squared propagator structure itself by the squared propagator structure taken on-shell, where  $\bar{s}_{ij} \rightarrow 0$ ,  $\bar{s}_{kl} \rightarrow 0$ :

$$\text{BW} = \frac{|\mathcal{P}(\bar{s}_{ij}, \bar{s}_{kl})|^2}{|\mathcal{P}(0, 0)|^2}. \quad (3.15)$$

Applying this procedure to the regulated doubly resonant matrix element leads to the Breit-Wigner factor of the doubly resonant case,

$$\begin{aligned} \text{BW} &= \left[ m_{ij}^2 m_{kl}^2 \Gamma_{ij}^2 \Gamma_{kl}^2 (m_{ij}(\Gamma_{ij} + \Gamma_{\text{reg}}) + m_{kl}(\Gamma_{kl} + \Gamma_{\text{reg}}))^2 \right. \\ &\times \left. \left( (s_{ij} + s_{kl} - m_{ij}^2 - m_{kl}^2)^2 + (m_{ij}\Gamma_{ij} + m_{kl}\Gamma_{kl})^2 \right) \right] / \\ &\left[ \left( (s_{ij} - m_{ij}^2)^2 + m_{ij}^2 \Gamma_{ij}^2 \right) \left( (s_{kl} - m_{kl}^2)^2 + m_{kl}^2 \Gamma_{kl}^2 \right) (m_{ij}\Gamma_{ij} + m_{kl}\Gamma_{kl})^2 \right. \\ &\times \left. \left( (s_{ij} + s_{kl} - m_{ij}^2 - m_{kl}^2)^2 + (m_{ij}(\Gamma_{ij} + \Gamma_{\text{reg}}) + m_{kl}(\Gamma_{kl} + \Gamma_{\text{reg}}))^2 \right) \right]. \end{aligned} \quad (3.16)$$

### 3.1.3 Off-to-on-shell momentum reshuffling

Subtracting the on-shell resonances makes a reshuffling of the external particle momenta necessary (c.f. Ref. [146]). The counterterms have to be evaluated at on-shell kinematics, which means that the intermediate particles have to satisfy the on-shell condition  $p_{ij}^2 = m_{ij}^2$ . Besides putting the intermediate particles on their mass shell, reshuffling the momenta has to preserve four-momentum conservation. To get the momenta of the external particles remapped to on-shell kinematics, we use a method

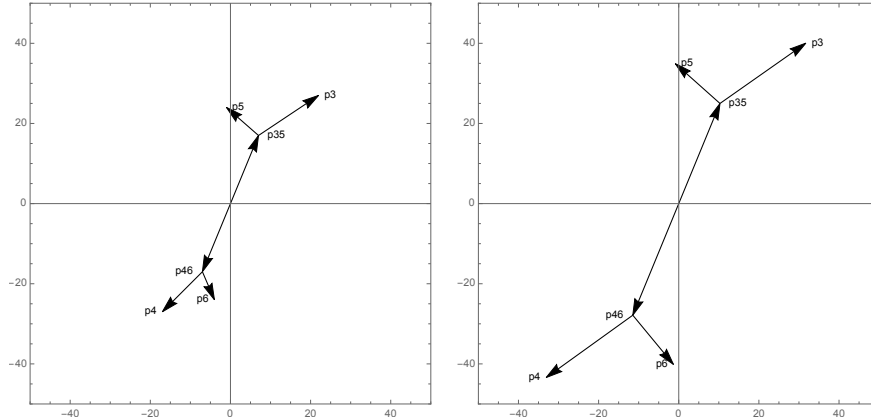


Figure 3.5: Example of an on-shell mapping of a  $2 \rightarrow 4$  scattering process with momenta  $p_i$  and masses  $m_i$  ( $i = 1, \dots, 6$ ) calculated with MATHEMATICA for the parameters  $m_3 = 1$ ,  $m_4 = 0$ ,  $m_5 = 5$ ,  $m_6 = 0$ ,  $m_{35} = 32$  and  $m_{46} = 30$  (in arbitrary units). The off-shell momenta (l.h.s.) are chosen to be  $\vec{p}_3 = (15, 10, 0)$ ,  $\vec{p}_4 = (-10, -10, 0)$  and  $\vec{p}_5 = (-8, 7, 0)$ , while the initial-state particles are massless and their momenta are calculated in their rest frame,  $\vec{p}_1 = (0, 0, E_1)$ ,  $\vec{p}_2 = (0, 0, -E_1)$ . The energies of the particles are given by  $E_i = \sqrt{\vec{p}_i^2 + m_i^2}$ . The remaining kinematical variables are fixed by four-momentum conservation,  $p_1 + p_2 = \sum_{i=3}^6 p_i$ . After applying the reshuffling algorithm, the on-shell momenta follow (r.h.s).

similar to the reshuffling algorithm used in the Catani-Seymour subtraction for IR divergences of real-emission diagrams [147]. Additionally, an analog reshuffling algorithm has been described earlier in Ref. [148] for the pair production of a squark and a neutralino.

Let us consider a  $2 \rightarrow 4$  particle production process with the incoming momenta  $p_1, p_2$  and the outgoing momenta  $p_i, p_j, p_k$  and  $p_l$ . The kinematics of the relevant resonant processes is given in Fig. 3.3 and Fig. 3.4. Reshuffling the momenta for the simpler  $2 \rightarrow 3$  process is a special case of the  $2 \rightarrow 4$  process and is therefore straightforward. We use the abbreviations  $p_{12} \equiv p_1 + p_2$ ,  $p_{ij} \equiv p_i + p_j$  and  $p_{kl} \equiv p_k + p_l$ . Similarly, we define  $s \equiv p_{12}^2$ ,  $s_{ij} \equiv p_{ij}^2$  and  $s_{kl} \equiv p_{kl}^2$ . The reshuffled momentum  $\tilde{p}_{ab}$  for the particle pairs  $a, b$ , which fulfills the on-shell conditions  $\tilde{s}_{ab} = p_{ab}^2 = m_{ab}^2$ , is



defined in terms of the original momenta  $p_{ab}$ :

$$\tilde{p}_{kl}^\mu = \frac{\lambda^{1/2}(s, m_{ij}^2, m_{kl}^2)}{\lambda^{1/2}(s, s_{ij}, s_{kl})} \left( p_{kl}^\mu - \frac{p_{12} \cdot p_{kl}}{s} p_{12}^\mu \right) + \frac{s + m_{kl}^2 - m_{ij}^2}{2s} p_{12}^\mu, \quad (3.17)$$

$$\tilde{p}_{ij}^\mu = p_{12}^\mu - \tilde{p}_{kl}^\mu, \quad (3.18)$$

where the Kaellen triangle function is given by

$$\lambda(x, y, z) = x^2 + y^2 + z^2 - 2(xy + yz + zx). \quad (3.19)$$

It is easy to show that from the definition of  $\tilde{p}_{ab}$  the correct on-shell conditions  $\tilde{p}_{ij}^2 = m_{ij}^2$  and  $\tilde{p}_{kl}^2 = m_{kl}^2$  follow. The three-particle case is retrieved by replacing  $(kl) \rightarrow k$  in the above formulas.

Now that the momenta  $\tilde{p}_{ij}$  and  $\tilde{p}_{kl}$  are fixed, the new outgoing momenta  $\tilde{p}_i, \tilde{p}_j, \tilde{p}_k$  and  $\tilde{p}_l$  can be calculated. The exact definition of the external momenta is arbitrary as long as the on-shell condition is not violated. One possibility is to keep the direction of one particle of a pair the same, say particles  $i$  and  $k$ , and use these conditions together with the on-shell condition to fix the remaining degrees of freedom. More specifically, for the case of reshuffling the momenta of particles  $i$  and  $j$ , we follow the steps:

1. Calculate  $\tilde{p}_{ij}$ .
2. Boost  $p_i$  and  $p_j$  into their rest frame, e.g.  $p_i \rightarrow p_i^{\text{cms}}$ , and extract the solid angle  $\Omega_i = (\phi_i, \theta_i)$  of particle  $i$ .
3. Construct the momenta  $\tilde{p}_i^{\text{cms}}$  and  $\tilde{p}_j^{\text{cms}}$  in their rest frame with condition  $m_{ij}^2 = (\tilde{p}_i^{\text{cms}} + \tilde{p}_j^{\text{cms}})^2$  and with the solid angle  $\Omega_i$  for particle  $i$ . In particular:

$$\tilde{p}_i^{\text{cms}, \mu} = \begin{pmatrix} \tilde{E}_i \\ \tilde{P}_i \sin \theta_i \cos \phi_i \\ \tilde{P}_i \sin \theta_i \sin \phi_i \\ \tilde{P}_i \cos \theta_i \end{pmatrix}, \quad (3.20)$$

$$\text{where } \tilde{E}_i = \frac{m_{ij}^2 + m_i^2 - m_j^2}{2m_{ij}^2} \text{ and } \tilde{P}_i = \frac{\lambda^{1/2}(m_{ij}^2, m_i^2, m_j^2)}{2m_{ij}^2}.$$

4. Boost back along  $\tilde{p}_{ij}$  which gives the momenta  $\tilde{p}_i$  and  $\tilde{p}_j$ .

Reshuffling the particle pairs  $k$  and  $l$  is equivalent to reshuffling particles  $i$  and  $j$ .

The whole procedure of computing the on-shell remapped momenta is conveniently collected in the subroutines `off_to_on_ijk` and `off_to_on_ijkl` which apply the on-shell conditions for the three particle and four particle case, respectively. All necessary routines can be found in the file `off_to_on.f` inside the project directories of `weakino-pair`<sup>2</sup> and `weakino-pair plus jet`<sup>3</sup> production. The routines we have developed are general and can be easily adapted to any other process of interest.

### 3.1.4 Jacobian correction factor

Since the matrix element  $|\mathcal{M}_{\text{res}}|_{\text{remapped}}^2$  has to be evaluated for on-shell kinematics in order to build the counterterm, it has to be integrated over a separate phase space that meets the on-shell condition, too. The counterterm is supposed to subtract the on-shell contributions only. However, an arbitrary real phase space point usually does not fulfill the on-shell condition. Evaluating the on-shell resonant matrix element only at on-shell kinematics could be achieved by applying the on-shell condition to the limits of the phase space integration or by introducing a ratio of the physical phase space Jacobian factor that corrects for integrating over the entire phase space where no on-shell condition is applied. If the limits of the phase space integration would not be adapted appropriately, an integration over the entire real phase space would combine on-shell and off-shell contributions inconsistently and off-shell contributions would be subtracted from the real matrix element.

In the following we use the same kinematical description of the variables  $s_{ij} = (p_i + p_j)^2$  and  $s_{ik} = (p_i + p_k)^2$  as introduced in Fig. 3.3. A general  $n$ -particle phase space integral according to Sec. 2.2.1 is given by

$$\int d\Phi_n = \frac{1}{(2\pi)^{3n-4}} R_n(s), \quad (3.21)$$

where the decomposition of  $R_n$  is defined in Eq. (2.19). Applying the general phase space decomposition to the three-particle case leads to

$$\int d\Phi_3 = \frac{1}{128\pi^3 s} \int_{(m_i+m_j)^2}^{(\sqrt{s}-m_k)^2} ds_{ij} \int_{s_{ik}^-}^{s_{ik}^+} ds_{ik}, \quad (3.22)$$

---

<sup>2</sup>`weakinos/Tools/functions/off_to_on.f`

<sup>3</sup>`weakinos+jet/Tools/functions/off_to_on.f`

where the limits of the  $s_{ik}$  integration are given by

$$s_{ik}^{\pm} = m_i^2 + m_k^2 + \frac{1}{2s_{ij}} \left[ (s + s_{ij} - m_k^2)(s_{ij} + m_i^2 - m_j^2) \pm \lambda^{1/2}(s, s_{ij}, m_k^2) \lambda^{1/2}(s_{ij}, m_i^2, m_j^2) \right]. \quad (3.23)$$

If the integration over  $s_{ik}$  is rescaled to a dimensionless integral over  $t \equiv (s_{ik} - s_{ik}^-)/(s_{ik}^+ - s_{ik}^-)$  a new Jacobian factor is introduced:

$$\int d\Phi_3 = \frac{1}{128\pi^3 s} \int_{(m_i+m_j)^2}^{(\sqrt{s}-m_k)^2} ds_{ij} \int_0^1 dt \frac{\lambda^{1/2}(s, s_{ij}, m_k^2) \lambda^{1/2}(s_{ij}, m_i^2, m_j^2)}{s_{ij}}. \quad (3.24)$$

For the phase space  $d\tilde{\Phi}_3$  of the remapped momenta, we have to apply the on-shell condition to the integration over  $s_{ij}$ . Therefore, we replace  $s_{ij}$  with  $m_{ij}^2$  in the Jacobian factor of Eq. (3.24), which results in

$$d\tilde{\Phi}_3 \propto \frac{\lambda^{1/2}(s, m_{ij}^2, m_k^2) \lambda^{1/2}(m_{ij}^2, m_i^2, m_j^2)}{m_{ij}^2} dt. \quad (3.25)$$

To build the on-shell counterterm, we integrate the on-shell matrix element over the restricted phase space  $d\tilde{\Phi}_3$ . Or similarly, the on-shell matrix element can be integrated over the entire phase space  $d\Phi_3$  where an additional Jacobian correction factor  $\mathcal{J}_3$  is used. This simplifies the implementation of the counterterm into the existing framework of the Monte Carlo program since the real matrix element and the counterterm can be integrated over the same phase space. The Jacobian correction factor reads

$$\mathcal{J}_3 = \frac{s_{ij} \lambda^{1/2}(s, m_{ij}^2, m_k^2) \lambda^{1/2}(m_{ij}^2, m_i^2, m_j^2)}{m_{ij}^2 \lambda^{1/2}(s, s_{ij}, m_k^2) \lambda^{1/2}(s_{ij}, m_i^2, m_j^2)}, \quad (3.26)$$

and it corrects for the incomplete phase space integration of the remapped matrix elements over the entire phase space, where no on-shell condition is applied, thus

$$d\tilde{\Phi}_3 = \mathcal{J}_3 d\Phi_3. \quad (3.27)$$

Similar to the Jacobian correction factor of the three-particle phase space, a correction factor for the four-particle phase space could be derived, too. One possible four-particle phase space parametrization is given by

$$\begin{aligned} \int d\Phi_4 &= \frac{1}{2^{15}\pi^7 s} \int_{(m_i+m_j)^2}^{(\sqrt{s}-m_k-m_l)^2} \frac{ds_{ij}}{s_{ij}} \int d\Omega_{ij} \int_{(m_k+m_l)^2}^{(\sqrt{s}-\sqrt{s_{ij}})^2} \frac{ds_{kl}}{s_{kl}} \int d\Omega_{kl} \\ &\times \lambda^{1/2}(s, s_{ij}, s_{kl}) \lambda^{1/2}(s_{ij}, m_i^2, m_j^2) \lambda^{1/2}(s_{kl}, m_k^2, m_l^2), \end{aligned} \quad (3.28)$$

where the kinematical description of Fig. 3.4 (b) is used. The integration measure over the solid angles are given by  $d\Omega_{ij} = d\phi_{ij}d\cos\theta_{ij}$  and  $d\Omega_{kl} = d\phi_{kl}d\cos\theta_{kl}$ , where  $\phi_{ij}$ ,  $\theta_{ij}$  and  $\phi_{kl}$ ,  $\theta_{kl}$  describe the azimuthal and polar angles between the particles  $i, j$  and  $k, l$ , respectively.

Following the same procedure as for the three-particle phase space, we obtain the Jacobian correction factor

$$\begin{aligned} \mathcal{J}_4 &= \frac{s_{ij}s_{kl}}{m_{ij}^2 m_{kl}^2} \frac{\lambda^{1/2}(s, m_{ij}^2, m_{kl}^2) \lambda^{1/2}(m_{ij}^2, m_i^2, m_j^2) \lambda^{1/2}(m_{kl}^2, m_k^2, m_l^2)}{\lambda^{1/2}(s, s_{ij}, s_{kl}) \lambda^{1/2}(s_{ij}, m_i^2, m_j^2) \lambda^{1/2}(s_{kl}, m_k^2, m_l^2)} \\ &\times \frac{(\sqrt{s} - m_{ij})^2 - (m_k + m_l)^2}{(\sqrt{s} - \sqrt{s_{ij}})^2 - (m_k + m_l)^2}. \end{aligned} \quad (3.29)$$

Thus, the restricted four-particle phase space with  $s_{ij} = m_{ij}^2$  and  $s_{kl} = m_{kl}^2$  is given by

$$d\tilde{\Phi}_4 = \mathcal{J}_4 d\Phi_4. \quad (3.30)$$

The similarities of the Jacobian correction factor for the three-particle and the four-particle case can easily be seen. However, an additional factor due to the nested limits of the  $s_{kl}$  integration occurs. This additional factor depends on the parametrization of the phase space and must be adapted accordingly.

### 3.1.5 Putting it all together

Finally, we are able to formulate the counterterms for the real matrix elements of weakino-pair and weakino-pair plus jet production. We split the real contribution to the cross section into a regular and an on-shell part. This allows us to perform the phase space integration separately for the regular and the on-shell subtracted resonant contributions,

$$\sigma_{\text{real}} = \sigma_{\text{real}}^{\text{reg}} + \sigma_{\text{real}}^{\text{OS}}, \quad (3.31)$$

with

$$\sigma_{\text{real}}^{\text{reg}} = \int d\Phi_{n+1} |M_{\text{reg}}|^2, \quad (3.32)$$

$$\sigma_{\text{real}}^{\text{OS}} = \sum_{\text{res}} \int d\Phi_{n+1} \left[ |M_{\text{res}}(\Gamma_{\text{reg}})|^2 - \mathcal{J}_{n+1} |M_{\text{res}}^{\text{CT}}(\Gamma_{\text{reg}})|^2 \right]. \quad (3.33)$$

The regular matrix element squared  $|M_{\text{reg}}|^2$  is given by the total real matrix element minus the resonant matrix element squared,

$$|M_{\text{reg}}|^2 = |M_{\text{real}}|^2 - \sum_{\text{res}} |M_{\text{res}}|^2. \quad (3.34)$$

Additionally, we take into account all possible particle combination which lead to an on-shell resonance by summing over all possible on-shell channels. Note that interference terms between resonant and regular contributions are not subtracted. Usually these contributions are not problematic since they are numerically small.

For the actual evaluation of  $\sigma_{\text{real}}^{\text{OS}}$  in the POWHEG-BOX, we have devised a routine allowing for a mapping of the phase space according to a specific resonance structure. Following this procedure, we can in principle handle an arbitrary number of resonance structures. The routine we have developed can thus be used for future POWHEG-BOX implementations of other processes requiring an on-shell resonance subtraction up to  $2 \rightarrow 4$  real matrix elements. We stress that this is the first implementation of a  $2 \rightarrow 4$  on-shell resonance subtraction to date.

## 3.2 Weakino-pair production

In the following we will discuss the details of our implementation of weakino-pair production processes in the framework of the POWHEG-BOX. We build on experience gained for related supersymmetric reactions, in particular slepton- and squark-pair production processes [144, 145, 149, 150]. Rather than going into general features required for the implementation of a new process in the POWHEG-BOX repository, we here will focus on aspects that are specific to weakino-pair production. The discussions and the results presented in the next sections are adopted from Ref. [137].

### 3.2.1 Born and virtual corrections

At leading order the production of a pair of weakinos proceeds via the tree level diagrams presented in Fig. 3.6 (a). In all channels the  $s$ -channel topology comprises Drell-Yan production,  $q\bar{q}' \rightarrow V^*$ , followed by the splitting  $V^* \rightarrow \tilde{\chi}_i\tilde{\chi}_j$ , where  $\tilde{\chi}_i$  stands for either a neutralino  $\tilde{\chi}_i^0$  ( $i = 1 \cdots 4$ ), or a chargino  $\tilde{\chi}_i^\pm$  ( $i = 1, 2$ ), depending on the process of interest. The vector boson  $V$  denotes a  $Z$  boson in the case of neutralino-pair production,  $V = W^\pm$  for the production of a neutralino and a chargino, and  $V = \gamma/Z$  for the production of a pair of charginos. In addition, diagrams with a squark being exchanged in the  $t$ - or  $u$ -channel occur. In the case of the production of a chargino and a neutralino only either  $t$ - or  $u$ -channel contributions arise, while for the other considered production processes both types of topologies contribute. We work in a scheme with five massless quark flavors in the initial state, i.e.  $q/q' = u, d, s, c, b$ . Numerically small bottom-mass effects are disregarded

### Weakino-pair production at hadron colliders

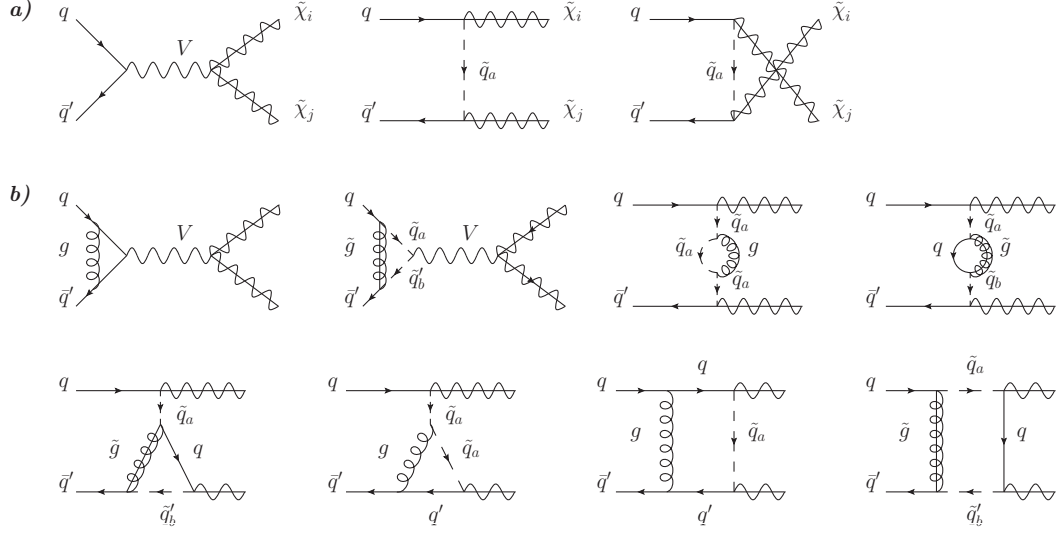


Figure 3.6: Representative (a) tree-level and (b) one-loop diagrams for the production of a pair of weakinos at a hadron collider. Depending on the type of the produced weakinos,  $V$  stands for  $W^\pm/Z/\gamma$ , and  $a, b = 1, 2$ .

throughout. This allows us to treat the scalar partners of these left- and right-chiral fermions as mass eigenstates. The CKM matrix is taken to be diagonal. We use FEYNARTS 3.9 [140] to generate the virtual diagrams and FORMCALC 8.4 [139] to calculate the amplitudes using the MSSM-CT model file of Ref. [151]. Representative Feynman diagrams for the virtual corrections are shown in Fig. 3.6 (b). They include vertex and box corrections with gluon, gluino, quark, or squark exchange, as well as self-energy corrections in the case of the  $t$ - and  $u$ -channel diagrams with squark exchange. Since the virtual diagrams are ultraviolet (UV) divergent, we have to define suitable counterterms to subtract the UV divergences in a well-defined way. The introduction of counterterms is done automatically by FEYNARTS. However, we have to select the relevant counterterm diagrams and self energies of the particles, that are necessary to fix the renormalization constants, by hand. Each counterterm diagram is proportional to a renormalization constant which is calculated from the self energies by the respective renormalization condition, see Eq. (2.42). The on-shell scheme introduced in Sec. 2.2.4 is used to fix the renormalization constants. The only self-energy diagrams needed for  $pp \rightarrow \tilde{\chi}_i \tilde{\chi}_j$  are given in Fig. 3.8. Finally, the scalar loop integrals [152] are numerically calculated with LOOPTOOLS 2.12 [139, 153].

We note that the dimensional reduction scheme we have used to regularize UV-

### 3.2 Weakino-pair production

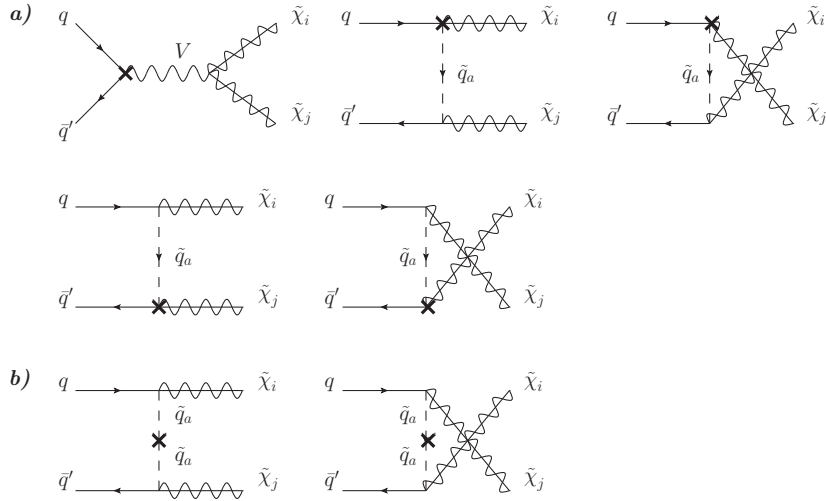


Figure 3.7: Vertex (a) and self-energy (b) counterterms for the pair production of weakinos.  $V$  stands for either  $W^\pm, Z$  or  $\gamma$  depending on the process of interest. The chirality indices  $a, b$  of the squarks can take the values 1, 2.

divergent diagrams breaks supersymmetry at the level of the gauge interactions by introducing a mismatch in the  $(D - 2)$  transverse degrees of freedom of the gauge bosons and the two degrees of freedom of the gauginos. To restore SUSY, a finite counterterm at NLO has to be inserted in the strong coupling constant  $\alpha_s$ . See Sec. 2.2.6 for more details.

### Weakino-pair production at hadron colliders

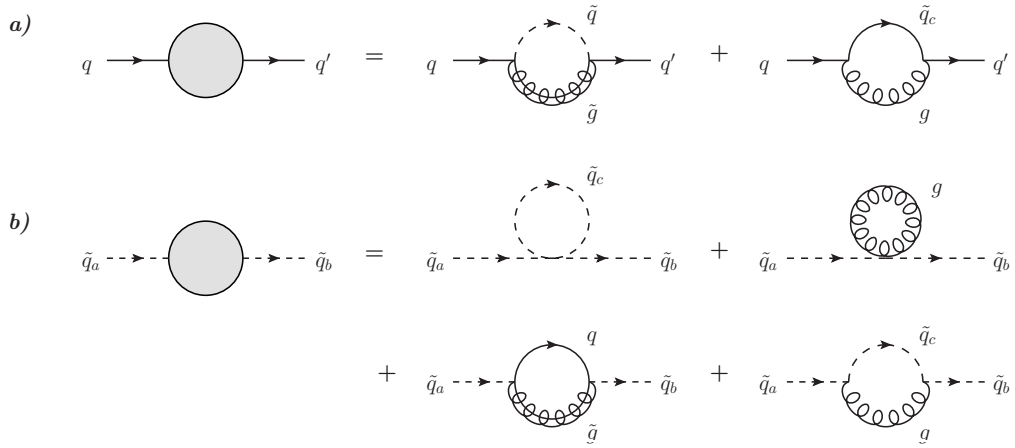


Figure 3.8: Self-energy diagrams for weakino-pair production used for determining the renormalization conditions. These self-energy diagrams are not process dependent and therefore relevant for weakino-pair production plus jet, too.

### 3.2.2 Real corrections

The NLO-QCD and SUSY-QCD corrections comprise real corrections with an extra parton in the final state. Only the sum of real and virtual corrections is infrared (IR) finite, see Sec. 2.3 for more details. In order to calculate the real-emission contributions and provide the ingredients necessary for the construction of IR subtraction terms by the POWHEG-BOX, we make use of a build tool based on MADGRAPH 4 [154–156]. It can be used to generate the Born, the color- and spin-correlated Born and the real-emission amplitudes in a format that can be easily processed by the POWHEG-BOX. The IR divergences are canceled separately in the virtual and in the real parts by using the Frixione-Kunszt-Signer (FKS) algorithm [124] that is implemented in the POWHEG-BOX, see Sec. 2.3.2 for more details. Representative real-emission diagrams are displayed in Fig. 3.9.



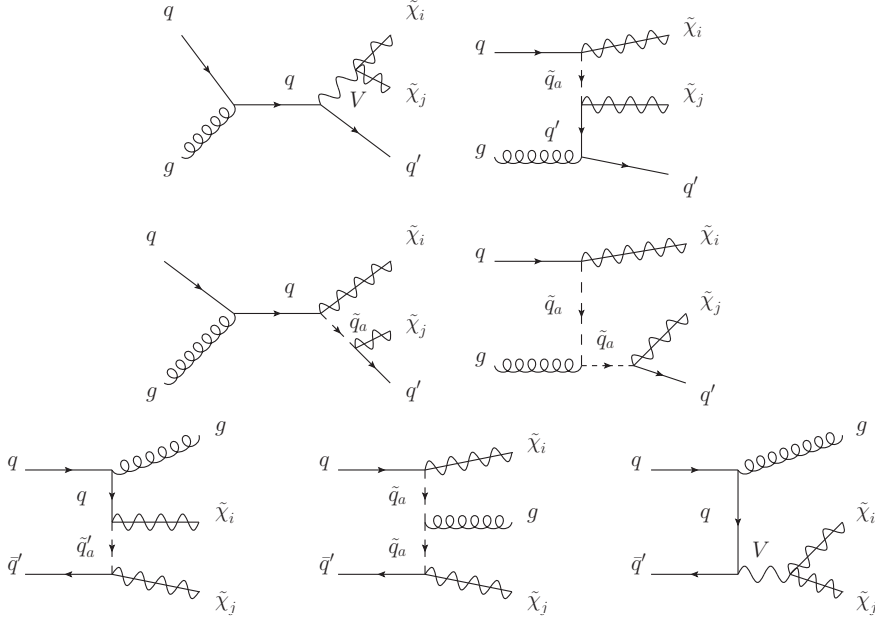


Figure 3.9: Representative real-emission diagrams for the production of a pair of weakinos.

### 3.2.3 On-Shell resonances

As mentioned earlier in Sec. 3.1 the real corrections of  $pp \rightarrow \tilde{\chi}_i \tilde{\chi}_j$  may be dominated for certain SUSY-parameter points by on-shell resonant diagrams. Each resonant diagram occurring in a subprocess of type  $qg \rightarrow \tilde{\chi}_i \tilde{\chi}_j q'$  exhibits a propagator that diverges when the intermediate squark is on its mass-shell. For instance, in the case of a  $\tilde{q} \rightarrow \tilde{\chi}_j q'$  decay, this implies  $(p_{\tilde{\chi}_j} + p_{q'})^2 \rightarrow m_{\tilde{q}}^2$  in terms of the momenta of the external particles. Following Sections 3.1.1 to 3.1.4 and using the same kinematics as depicted by Fig. 3.10 we introduce a counterterm of the form

$$\begin{aligned}
 \left| \mathcal{M}_{\text{res}}^{\text{CT}}(\Gamma_{\text{reg}}) \right|^2 &= \Theta \left( s - (m_{ij} + m_k)^2 \right) \Theta (m_{ij} - m_i - m_j) \\
 &\quad \times \frac{m_{ij}^2 \Gamma_{\text{reg}}^2}{(s_{ij} - m_{ij}^2)^2 + m_{ij}^2 \Gamma_{\text{reg}}^2} \left| \mathcal{M}_{\text{res}}(\Gamma_{\text{reg}}) \right|_{\text{remapped}}^2, \quad (3.35)
 \end{aligned}$$

where the momenta entering  $\mathcal{M}_{\text{res}}$  are to be remapped to the on-shell kinematics (c.f. Sec. 3.1.3). The dependence on the final-state momenta and masses gets more

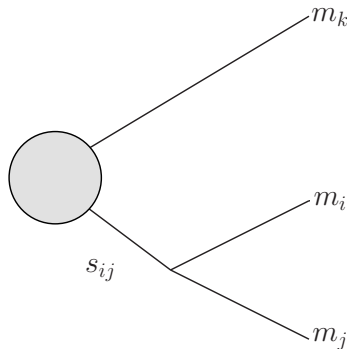


Figure 3.10: Final-state topology of a singly resonant diagram for the production of the particles  $i, j$  and  $k$ .

obvious if we rewrite the counterterm as

$$\left| \mathcal{M}_{\text{res}}^{\text{CT}}(\Gamma_{\text{reg}}) \right|^2 = \Theta \left( s - (m_{q'} + m_{\tilde{\chi}_i})^2 \right) \Theta \left( m_{\tilde{q}_a} - m_{q'} - m_{\tilde{\chi}_j} \right) \quad (3.36)$$

$$\times \frac{m_{\tilde{q}_a}^2 \Gamma_{\text{reg}}^2}{((p_{\tilde{\chi}_j} + p_{q'})^2 - m_{\tilde{q}_a}^2)^2 + m_{\tilde{q}_a}^2 \Gamma_{\text{reg}}^2} \left| \mathcal{M}_{\text{res}}(\Gamma_{\text{reg}}) \right|_{\text{remapped}}^2. \quad (3.37)$$

Since we only consider massless quarks we set  $m_{q'} = 0$  GeV in our calculation. We also stress that the decay width  $\Gamma_{\text{reg}}$  introduced in Eq. (3.37) is to be viewed as a technical regulator in the on-shell subtraction procedure. It may, but not necessarily has to, be identified with the actual physical decay width for the resonant squark. Since after the on-shell subtraction results should not depend on the resonant contributions, final results must be independent of  $\Gamma_{\text{reg}}$ .

As mentioned earlier, the DSUB method violates gauge invariance as  $\Gamma_{\text{reg}} \neq 0$ . However, gauge invariance violating contributions in the approach we are using are numerically negligible, as demonstrated by the independence of our results on the technical parameter  $\Gamma_{\text{reg}}$  discussed below.

### 3.2.4 Numerical checks

In order to verify the validity of our implementation, we have performed a number of checks. First, we have numerically compared the Born and real amplitudes generated by MADGRAPH and FORMCALC and found agreement up to double precision. The virtual amplitudes are UV finite, which have been tested by setting  $\Delta_{\text{UV}}$ , the numerical parameter of FORMCALC which controls the  $1/\varepsilon$  poles, to a large

number<sup>4</sup>. Next, we have tested that, after the subtraction of on-shell resonances, for collinear momentum configurations real-emission and IR subtraction terms approach each other.

We have found that the dependence of our predictions for weakino-pair production cross sections on the technical regulator  $\Gamma_{\text{reg}}$  is negligible. Figure 3.11 illustrates the regulator dependence of the neutralino-pair production cross section for a SUSY benchmark point that features squarks heavy enough to on-shell decay into a neutralino and a quark. We consider the mSUGRA spectrum SPS 1a [157] with  $m_0 = 100$  GeV,  $m_{1/2} = 250$  GeV,  $A_0 = -100$  GeV,  $\text{sgn}(\mu) = +1$ , and  $\tan\beta = 10$  at the GUT scale, resulting in the lightest neutralino mass  $m_{\tilde{\chi}_1^0} = 96.69$  GeV and the first-generation squark masses  $m_{\tilde{u}_L/\tilde{u}_R/\tilde{d}_L/\tilde{d}_R} = 561.1/549.3/568.4/545.2$  GeV. Although this benchmark point is already excluded by experiment, see, for example, Ref. [59], we use it in order to illustrate the technical details of the regulator dependence as it easily provides a spectrum for which the squark masses induce resonances to be regulated. We do not use this benchmark point for phenomenological studies. In the range  $\Gamma_{\text{reg}}/\bar{m}_{\tilde{q}} = 10^{-5}$  to  $10^{-1}$ , where  $\bar{m}_{\tilde{q}} = 556$  GeV is the average of the four squark masses of the first generation, the dependence of the cross section on the regulator is entirely negligible, thus confirming the stability of the applied on-shell subtraction procedure.

Finally, we have computed total cross sections at LO and NLO accuracy in the setup of Ref. [158] and found agreement with the published results.

### 3.2.5 Phenomenological setup and results

A collection of electroweakino-pair production processes was made publicly available in the framework of the POWHEG-BOX via the project website <http://powhegbox.mib.infn.it/><sup>5</sup>. Since the public code can be used for specific user applications, we refrain from presenting an extensive numerical analysis here, but only intend to highlight some representative phenomenological results.

For our numerical studies, we consider proton-proton collisions at the LHC with a center-of-mass energy of  $\sqrt{s} = 14$  TeV. For the parton distribution functions (PDFs) of the proton we use the PDF4LHC15 NLO set [159] as implemented in the LHAPDF library [160]. Since no LO set is provided by the PDF4LHC15 working group, we

<sup>4</sup>We have tested UV-finiteness up to  $\Delta_{\text{UV}} = 10^7$  and found no dependence on the parameter  $\Delta_{\text{UV}}$  within double precision.

<sup>5</sup>Additional useful programs and scripts that were used to generate the calculation of weakino-pair production can be found on <https://github.com/MKesenheimer/weakinos>.

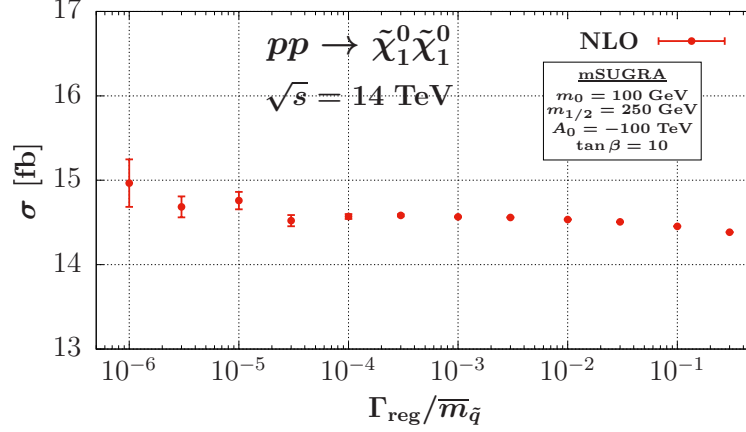


Figure 3.11: Dependence of the total cross section for the process  $pp \rightarrow \tilde{\chi}_1^0 \tilde{\chi}_1^0$  with  $\sqrt{s} = 14$  TeV on the regulator  $\Gamma_{\text{reg}}$  normalized to the average squark mass of  $\overline{m}_{\tilde{q}} = 556$  GeV.

use the NLO set also for the computation of LO results.

Unless explicitly specified otherwise, we choose fixed values for the renormalization and factorization scales,  $\mu_R$  and  $\mu_F$ , proportional to the sum of the masses of the weakinos  $\tilde{\chi}_i$  and  $\tilde{\chi}_j$  produced in the specific process under consideration,  $\mu_R = \mu_F = \xi \mu_0$  with  $\mu_0 = m_{\tilde{\chi}_i} + m_{\tilde{\chi}_j}$ . The scale parameter  $\xi$  is set to one by default. When combining fixed-order results with a parton-shower program, we use PYTHIA 6.4.25 [161]. QED radiation, underlying event, and hadronization effects are switched off throughout. Partons arising from the real-emission contributions of the NLO-QCD calculation or from the parton shower are recombined into jets according to the anti- $k_T$  algorithm [121] as implemented in the FASTJET 3.13 package [162] with  $R = 0.4$  and  $|\eta^{\text{jet}}| < 4.5$  which is found to describe jet recombination well.

As electroweak input parameters we choose the  $Z$  boson mass,  $m_Z = 91.1876$  GeV, the electromagnetic coupling,  $\alpha^{-1}(m_Z) = 127.934$ , and the Fermi constant,  $G_F = 1.16638 \times 10^{-5}$  GeV $^{-2}$ . The other SM and MSSM parameters required for our calculations are provided in the form of a file complying with the SUSY Les Houches Accord (SLHA) [163, 164] that can be computed with an independent external spectrum calculator. We have used the SUSPECT 2.43 program [165] for the calculation of the spectrum and the SDECAY program [166] for the decay widths and branching fractions to obtain such an SLHA file. Specifically, we consider a minimal supergravity (mSUGRA) benchmark point suggested in Ref. [167] that is consistent with a Higgs mass of about 126 GeV as well as further collider and dark matter

constraints. This benchmark point is characterized by the following SUSY input parameters:  $m_{1/2} = 470$  GeV,  $m_0 = 6183$  GeV,  $A_0 = -4469$  GeV,  $\tan\beta = 52.1$ ,  $\text{sgn}(\mu) = +1$ . These are resulting in neutralino masses of

$$m_{\tilde{\chi}_1^0} = 207.0 \text{ GeV}, \quad m_{\tilde{\chi}_2^0} = 405.9 \text{ GeV}, \quad (3.38)$$

$$m_{\tilde{\chi}_3^0} = 598.1 \text{ GeV}, \quad m_{\tilde{\chi}_4^0} = 612.9 \text{ GeV}, \quad (3.39)$$

and chargino masses of

$$m_{\tilde{\chi}_1^\pm} = 405.8 \text{ GeV}, \quad m_{\tilde{\chi}_2^\pm} = 613.2 \text{ GeV}. \quad (3.40)$$

The squark masses are equal for the first and second generation, but different for the third generation. The numerical values are as follows:

$$m_{\tilde{d}_L/\tilde{s}_L} = 6.172 \text{ TeV}, \quad m_{\tilde{d}_R/\tilde{s}_R} = 6.193 \text{ TeV}, \quad (3.41)$$

$$m_{\tilde{u}_L/\tilde{c}_L} = 6.172 \text{ TeV}, \quad m_{\tilde{u}_R/\tilde{c}_R} = 6.190 \text{ TeV},$$

$$m_{\tilde{b}_1} = 4.132 \text{ TeV}, \quad m_{\tilde{b}_2} = 4.591 \text{ TeV}, \quad (3.42)$$

$$m_{\tilde{t}_1} = 3.577 \text{ TeV}, \quad m_{\tilde{t}_2} = 4.112 \text{ TeV}. \quad (3.43)$$

For this benchmark point, we first consider the neutralino-pair production process  $pp \rightarrow \tilde{\chi}_1^0 \tilde{\chi}_1^0$ . We find a total cross section of  $\sigma^{\text{LO}} = 4.780$  ab at LO and of  $\sigma^{\text{NLO}} = 5.595$  ab at NLO. The NLO SUSY-QCD corrections thus enhance the production rate by more than 15%. In order to quantify the dependence of these results on the unphysical renormalization and factorization scales, we have varied  $\mu_R$  and  $\mu_F$  in the range  $0.1\mu_0$  to  $10\mu_0$  around our default choice  $\mu_R = \mu_F = \mu_0 = 2m_{\tilde{\chi}_1^0}$ , c.f. Fig. 3.12. At LO, neutralino-pair production is a purely electroweak process and thus only depends on  $\mu_F$  via the parton distribution functions of the scattering protons. The scale behavior of the LO results directly reflects the  $\mu_F$  dependence of the (anti-)quark distribution functions in the probed kinematic regime. At NLO, additionally  $\mu_R$  enters and, in contrast to  $\mu_F$  being effectively accounted for only at lowest order, dominates the scale uncertainty of  $\sigma^{\text{NLO}}$ . However, in the typically considered range  $\mu_0/2$  to  $2\mu_0$  the NLO cross section changes by only about 3%, indicating that the perturbative expansion is rather stable, and the scale uncertainty is reduced compared to the LO predictions.

In order to assess the impact of the higher-order corrections and parton shower effects on kinematic features of weakino-pair production, we consider the representative chargino-pair production process  $pp \rightarrow \tilde{\chi}_1^+ \tilde{\chi}_1^-$ . Numerical uncertainties are at the permille level and not shown in the plots that follow.

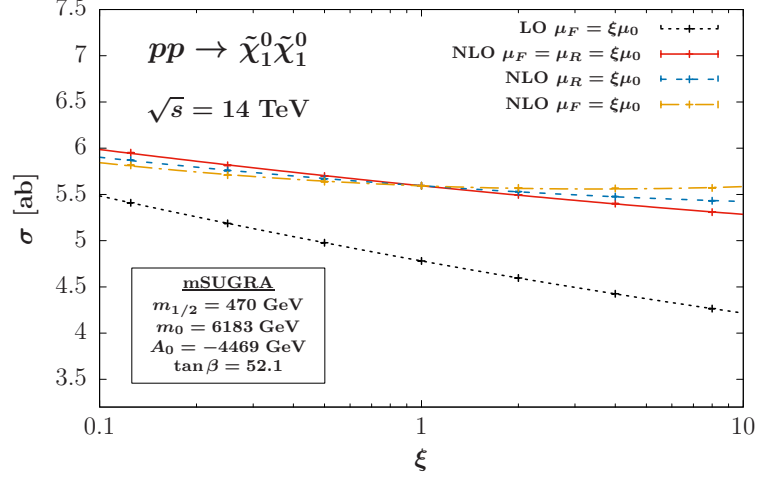


Figure 3.12: Dependence of the total cross section for the process  $pp \rightarrow \tilde{\chi}_1^0 \tilde{\chi}_1^0$  with  $\sqrt{s} = 14$  TeV on the factorization and renormalization scales. The NLO curves show the cross section as a function of the scale parameter  $\xi$  for three different cases:  $\mu_R = \mu_F = \xi\mu_0$  (solid red line),  $\mu_R = \xi\mu_0, \mu_F = \mu_0$  (dashed blue line), and  $\mu_R = \mu_0, \mu_F = \xi\mu_0$  (dot-dashed yellow line). The LO cross section only depends on  $\mu_F = \xi\mu_0$  (dotted black line). In each case,  $\mu_0 = 2m_{\tilde{\chi}_1^0}$ .

Figure 3.13 illustrates the transverse-momentum and pseudo-rapidity distributions of the  $\tilde{\chi}_1^+$  at fixed order, and after the matching of the NLO result to the parton shower (NLO+PS). Analogous results are obtained for the other chargino,  $\tilde{\chi}_1^-$ . In Fig. 3.14 (left) we depict the invariant-mass distribution of the chargino pair. As expected from the above discussion of total cross sections for the related case of neutralino-pair production, we notice that the normalization of these distributions changes significantly when going from LO to NLO. On the other hand, their shapes are only slightly affected by the NLO corrections, as illustrated by the dynamical  $K$ -factors,

$$K = \frac{d\sigma^{\text{NLO}}}{d\sigma^{\text{LO}}}, \quad (3.44)$$

which turn out to be mostly flat.

Obviously, parton-shower effects on the massive final state are very small for all considered distributions, which is largely due to the large mass and color-neutral nature of the supersymmetric final state. Details of the parton-shower settings will thus barely affect predictions for observables related to the charginos at NLO+PS

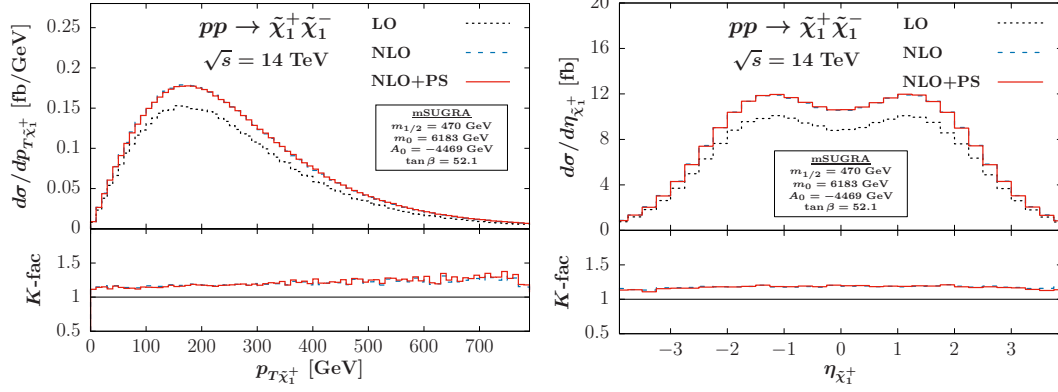


Figure 3.13: Transverse-momentum (left) and pseudorapidity distribution (right) of the  $\tilde{\chi}_1^+$  in the process  $pp \rightarrow \tilde{\chi}_1^+ \tilde{\chi}_1^-$  at LO (dotted black lines), NLO (dashed blue lines), and NLO+PS (solid red lines) for our default setup.

level. Because of the small impact parton shower effects have on NLO results, in the figures the NLO and NLO+PS curves are almost indistinguishable.

More pronounced effects of the parton shower emerge in jet observables, such as the transverse-momentum distribution of the hardest jet shown in Fig. 3.14 (right). For the reaction  $pp \rightarrow \tilde{\chi}_1^+ \tilde{\chi}_1^-$ , at NLO, jets can only result from a hard parton of the real-emission contributions. After matching with a parton shower, additional jets can occur that will, however, be mostly soft or collinear. From the displayed figure it is apparent that while in the fixed-order calculation the transverse-momentum distribution of the jet diverges towards small values of  $p_T^{\text{jet}}$ , the Sudakov form factor of the NLO+PS calculation tames this would-be divergence. We note, however, that a precise description of jet observables in weakino-pair production processes would require considering the related reactions with an associated jet being present at LO already. Only a full NLO calculation for the  $\tilde{\chi}_1^+ \tilde{\chi}_1^- + \text{jet}$  production process would yield NLO-accurate predictions for jet distributions, which is the content of the next section. In our calculation of  $pp \rightarrow \tilde{\chi}_1^+ \tilde{\chi}_1^-$ , jet observables are described effectively only at LO accuracy and thus associated with significant theoretical uncertainties.

Our results confirm the findings obtained in the context of a jet veto resummation formalism [168] for the related case of slepton-pair production, which revealed that theoretical uncertainties at the lowest resummation order are large enough to weaken current exclusion limits relying on searches making use of jet vetoes.

In many SUSY scenarios, the  $\tilde{\chi}_1^0$  represents the LSP that, due to the requirement

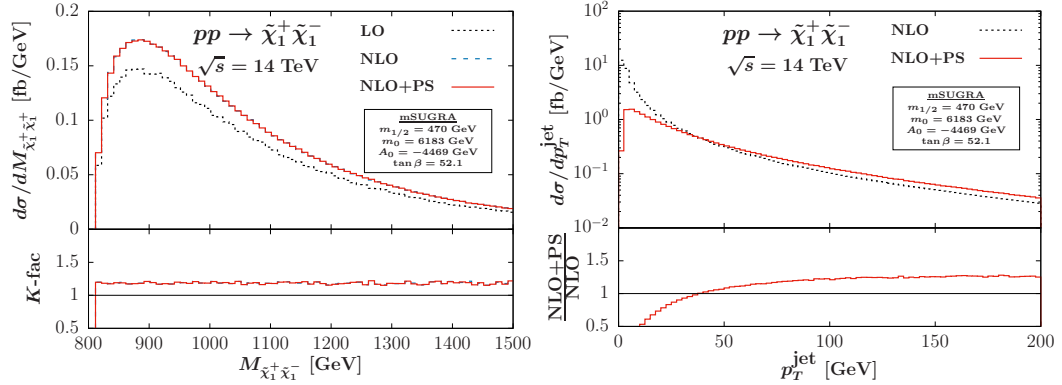


Figure 3.14: Invariant-mass distribution of the chargino-pair (left) and transverse-momentum distribution of the hardest jet (right) for the process  $pp \rightarrow \tilde{\chi}_1^+ \tilde{\chi}_1^-$  at LO (dotted black lines), NLO (dashed blue lines), and NLO+PS (solid red lines) for our default setup.

of R-parity conservation, does not decay. Being electrically neutral, such an LSP cannot be observed directly in the detector, but only via its imprint on the missing transverse-energy spectrum. Depending on the mass hierarchy of a SUSY parameter point, heavier neutralinos and charginos decay via chains into a combination of stable particles, such as partons, leptons, neutrinos, and the LSP. Particularly clean experimental signatures emerge from final states with charged leptons that are rare in the context of the Standard Model. A prime example is provided by the leptonic decay chain of the process  $pp \rightarrow \tilde{\chi}_2^0 \tilde{\chi}_1^+$  that gives rise to a three-lepton final state as depicted in Fig. 3.15. Having full access to supersymmetric decay chains in a Monte Carlo simulation is thus of great phenomenological relevance.

The codes we developed for weakino-pair production processes offer such an option by an interface to the SUSY decay feature of PYTHIA. We can thus provide predictions that are at the same time NLO accurate for the hard weakino-pair production process, include parton-shower emission effects, and give full access to the kinematic properties of the stable particles in specific decay chains using the narrow-width approximation.

To illustrate this feature, we focus on final states with three charged leptons plus missing transverse energy arising from the  $\tilde{\chi}_2^0 \tilde{\chi}_1^+$  production process. For the setup of this simulation, we follow closely the strategy of the ATLAS analysis reported in Ref. [169]. We only consider events with an electron, a positron, a muon, and a large amount of missing transverse energy in the final state. Each charged



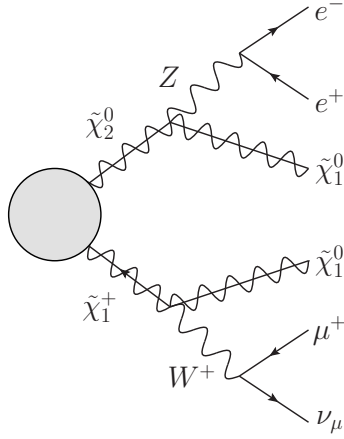


Figure 3.15: Leptonic decay chain for the process  $pp \rightarrow \tilde{\chi}_2^0 \tilde{\chi}_1^+$ , giving rise to an  $e^- e^+ \mu^+ + E_T^{\text{miss}}$  final state.

lepton is required to exhibit non-vanishing transverse momentum, be located in the central-rapidity region and sufficiently well separated from each other in the rapidity-azimuthal angle plane,

$$p_T^\ell > 10 \text{ GeV}, \quad |\eta^\ell| < 2.5, \quad \Delta R(\ell, \ell') > 0.05. \quad (3.45)$$

In addition, the missing transverse momentum is required to be large,

$$p_T^{\text{miss}} > 100 \text{ GeV}. \quad (3.46)$$

This latter observable is computed from the negative sum of the final-state particles that are detected, i.e. the electron, positron, muon, and jets with a transverse momentum  $p_T^j \geq 20 \text{ GeV}$ , similar to what is done in the experimental analyses.

As the sum of the transverse momenta of the final-state particles should add to zero, this is effectively similar to the sum over the non-detected particles, i.e. the LSP, the neutrinos emerging in the decay chain, and the softer jets. Figure 3.16 (left) shows the missing transverse momentum distribution obtained with our POWHEG+PYTHIA simulation after the cuts listed above are applied.

Here and in the following, results are presented for the default NLO+PS setup obtained by matching the NLO result via the POWHEG formalism with PYTHIA, and for reference also for a LO sample matched with PYTHIA using the same parton-shower settings, referred to as LO+PS. The ratios

$$R = \frac{d\sigma^{\text{NLO+PS}}}{d\sigma^{\text{LO+PS}}} \quad (3.47)$$

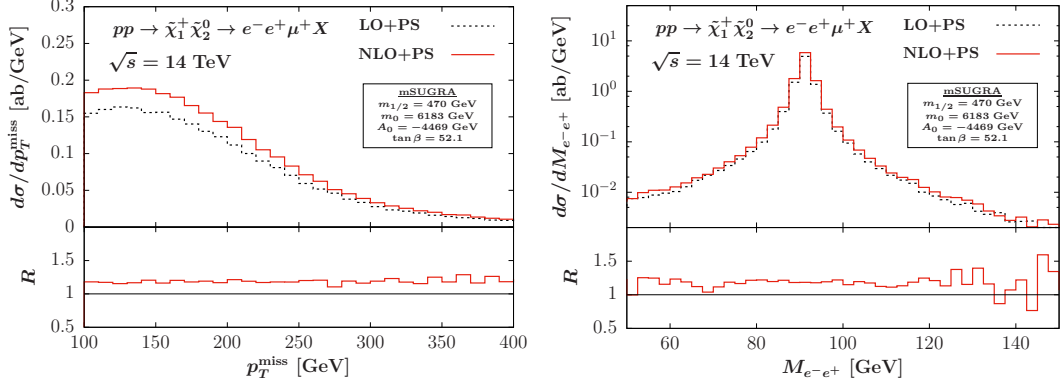


Figure 3.16: Missing transverse momentum (left) and invariant mass distribution of the  $e^+e^-$  system (right) emerging in the  $e^+e^-\mu^+ + E_T^{\text{miss}}$  decay mode of the process  $pp \rightarrow \tilde{\chi}_2^0 \tilde{\chi}_1^-$  at LO (dotted black lines) and NLO (solid red lines) matched with PYTHIA, after the leptonic cuts of Eqs. (3.45) and (3.46) are applied.

help to quantify the impact of the NLO corrections in the presence of parton-shower effects on distributions of the decay products encountered in the considered reaction. We find that the general features of the NLO corrections are very similar for distributions of the decay particles as for the weakinos produced in the primary hard scattering process,  $pp \rightarrow \tilde{\chi}_2^0 \tilde{\chi}_1^-$ . In particular, the  $R$  ratio is flat over the entire range of missing transverse momentum, with a size of about 1.2 resembling the ratio of the integrated NLO and LO cross sections.

Figure 3.16 (right) illustrates the invariant mass distribution of the  $e^+e^-$  system in the considered process. Apparently, the decay of the  $\tilde{\chi}_2^0$  into a lepton pair and the  $\tilde{\chi}_1^0$  LSP is dominated by  $e^+e^-$  pairs with an invariant mass close to the  $Z$  pole. Similarly, the decay of the  $\tilde{\chi}_1^+$  into a  $\mu^+\nu_\mu$  pair and an LSP features a lepton-neutrino pair dominated by the  $W$  resonance. Since the invariant mass of the  $\mu^+\nu_\mu$  pair cannot be fully reconstructed because of the non-detectable neutrino we refrain from showing that distribution here. Similar to the case of missing transverse momentum, the  $R$  ratio turns out to be flat for the invariant mass distribution of the  $e^+e^-$  system, with slightly more statistical fluctuations far away from the resonance region at around  $M_{e^+e^-} \sim M_Z$  than in the peak region.

The transverse-momentum distribution of the electron is depicted in Fig. 3.17. Because of the selection cuts of Eq. (3.45) that we impose, no events with a transverse momentum smaller than 10 GeV occur. Over the entire plot range, the  $R$  ratio

### 3.2 Weakino-pair production

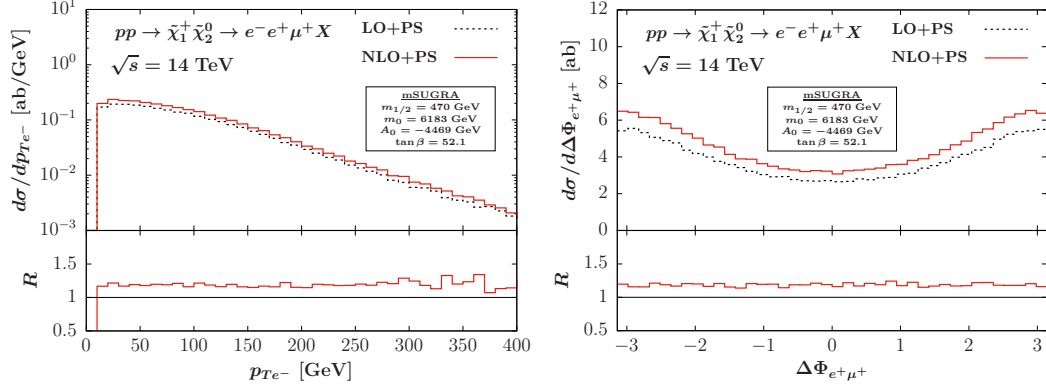


Figure 3.17: Transverse momentum distribution of the electron (left) and azimuthal-angle separation of the positron and the muon (right) emerging in the  $e^+e^-\mu^+ + E_T^{\text{miss}}$  decay mode of the process  $pp \rightarrow \tilde{\chi}_1^0 \tilde{\chi}_1^+$  at LO (dotted black lines) and NLO (solid red lines) matched with PYTHIA, after the leptonic cuts of Eqs. (3.45) and (3.46) are applied.

amounts to about 1.2, i.e. the NLO corrections are distributed rather uniformly for this distribution.

The r.h.s. of Fig. 3.17 shows the azimuthal-angle separation  $\Delta\Phi_{e^+\mu^+}$  of the two positively charged leptons occurring in the  $e^+e^-\mu^+ + E_T^{\text{miss}}$  final state. We note that the azimuthal-angle separation of the positron and the muon peaks at  $\pm\pi$ . Also for this distribution, the impact of NLO corrections is flat over the entire range considered.

## Weakino-pair production at hadron colliders

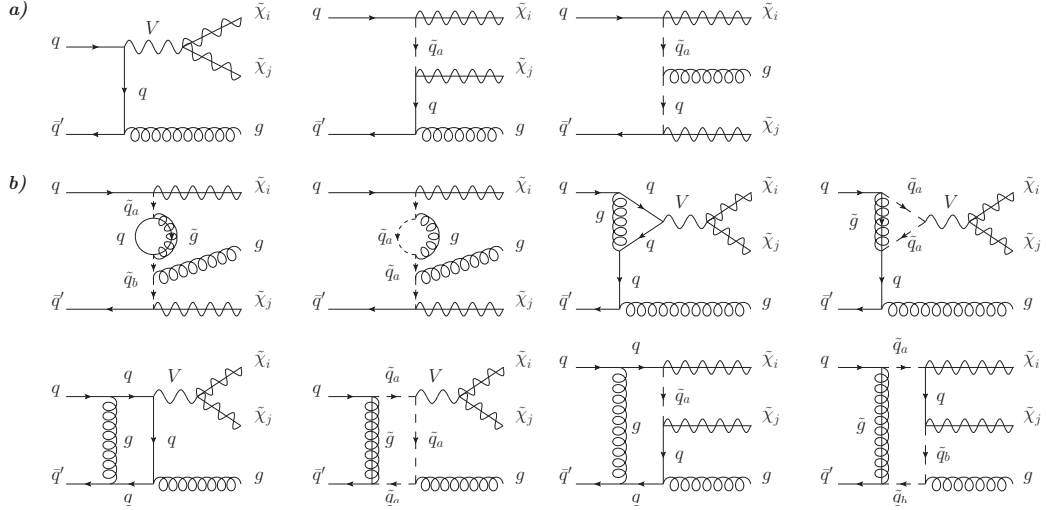


Figure 3.18: Representative (a) tree-level and (b) one-loop diagrams for the production of a pair of weakinos,  $\tilde{\chi}_i \tilde{\chi}_j$ , with a jet. Depending on the types  $i, j$  of the produced weakinos,  $V$  stands for  $W^\pm/Z/\gamma$ , and  $a, b = 1, 2$ .

## 3.3 Weakino-pair plus jet production

The succeeding sections will focus on the implementation of weakino-pair plus jet production processes in the framework of the POWHEG-BOX. We observe that additional subtleties with respect to weakino-pair production processes occur, such as doubly on-shell resonant diagrams in the real corrections and the problem of the consistent treatment of particle widths that already have to be used in the Born and virtual diagrams. However, the general framework stays the same and we can build on the previous and simpler weakino-pair production process. The discussions and the results presented in the next sections are adopted from Ref. [138].

### 3.3.1 Born and virtual corrections

The Real-emission diagrams of weakino-pair production become the Born diagrams for weakino-pair plus jet production. Representative diagrams at Born level are shown in Fig. 3.18 (a). As in the case for weakino-pair production, the diagrams can be divided into  $s$ -channel topologies with a SM Drell-Yan structure,  $q\bar{q}' \rightarrow V^*$ , followed by the splitting  $V^* \rightarrow \tilde{\chi}_i \tilde{\chi}_j$ , where  $\tilde{\chi}_i$  stands for either a neutralino  $\tilde{\chi}_i^0$  ( $i = 1 \dots 4$ ), or a chargino  $\tilde{\chi}_i^\pm$  ( $i = 1, 2$ ), depending on the process of interest and

### 3.3 Weakino-pair plus jet production

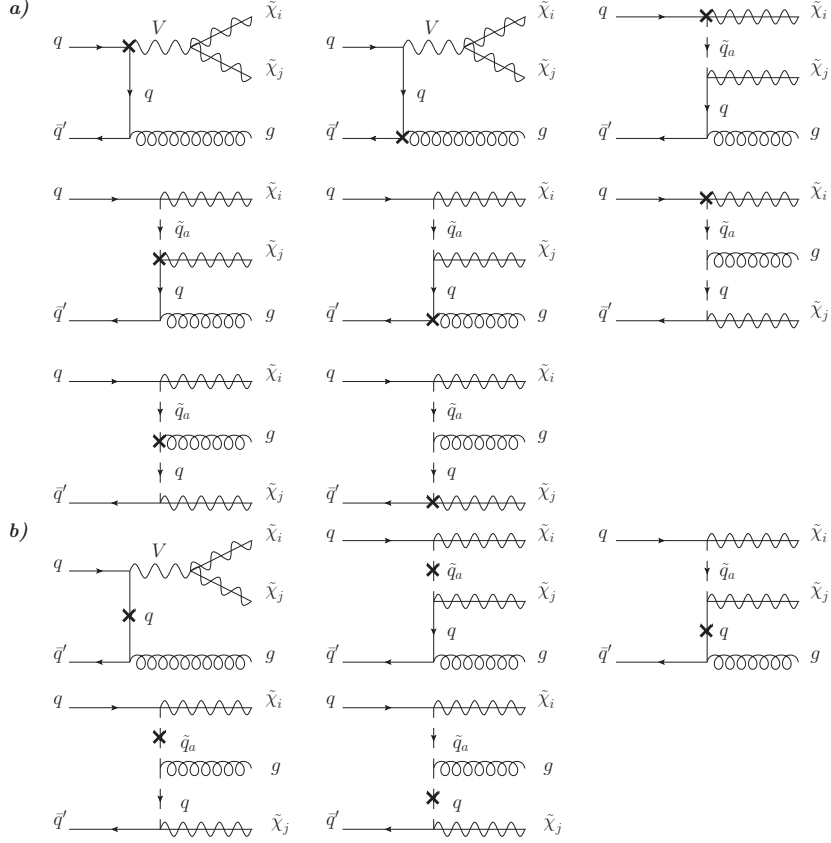


Figure 3.19: Vertex (a) and self-energy (b) counterterms for the pair production of weakinos plus jet.  $V$  stands for either  $W^\pm, Z$  or  $\gamma$  depending on the process of interest. The chirality indices  $a, b$  of the squarks can take the values 1, 2.

into diagrams with a squark being exchanged in the  $t$ - or  $u$ -channel. We assume four massless active quark flavors in the running of the strong coupling constant and take finite bottom-quark and top-quark mass effects emerging in loop diagrams into account in the calculation. The Cabibbo-Kobayashi-Maskawa matrix is taken diagonal and we also use four-flavor-scheme parton distribution functions with no bottom-quark initial states.

In the gluon-induced channels  $q(\bar{q})g \rightarrow \tilde{\chi}_i \tilde{\chi}_j q(\bar{q})$ , single resonances can already occur at the lowest order when an intermediate squark happens to be on-shell in an  $s$ -channel diagram. These resonance effects are regulated by using the complex-mass scheme (c.f. Sec. 2.2.7). We replace the mass of the squark,  $m_{\tilde{q}_k}$ , with a complex

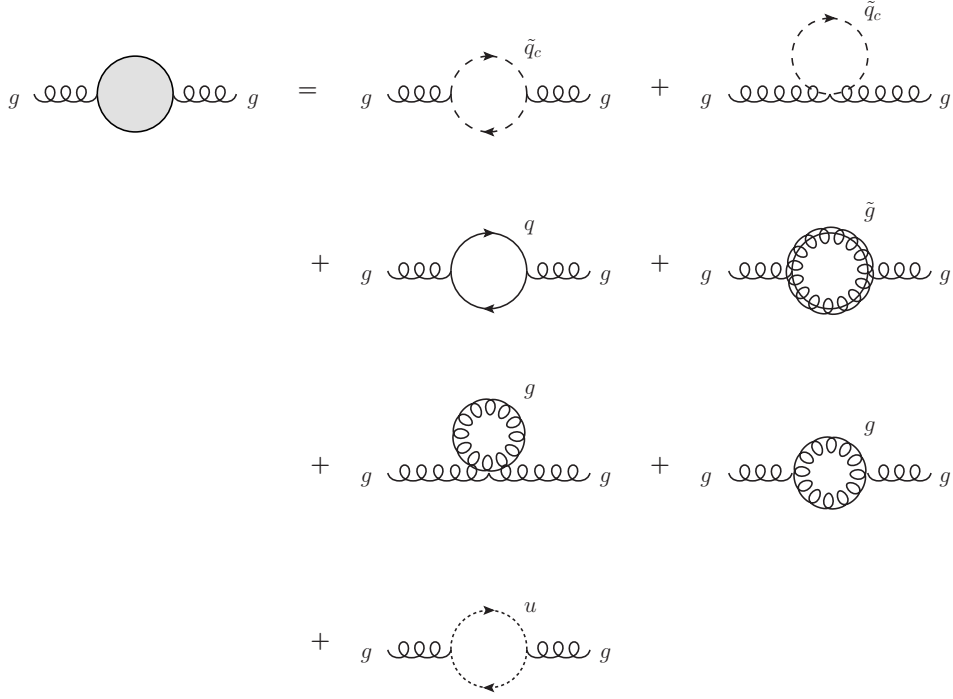


Figure 3.20: Self-energy diagrams for weakino-pair plus jet production used for determining the renormalization conditions. Additional self-energy diagrams are given in Fig. 3.8.

mass  $\mu_{\tilde{q}_k}$  such that  $\mu_{\tilde{q}_k}^2 = m_{\tilde{q}_k}^2 - i\Gamma_{\tilde{q}_k} m_{\tilde{q}_k}$ , where  $\Gamma_{\tilde{q}_k}$  denotes the physical decay width of the squark. We stress that this procedure is gauge invariant.

The virtual corrections to the three parton-level processes  $q\bar{q}' \rightarrow \tilde{\chi}_i\tilde{\chi}_jg$ ,  $qg \rightarrow \tilde{\chi}_i\tilde{\chi}_jq$ , and  $\bar{q}g \rightarrow \tilde{\chi}_i\tilde{\chi}_j\bar{q}$  are classified as self-energy, triangle, box, and pentagons corrections, with gluon, gluino, quark, or squark exchange, see Fig. 3.18 (b) for some representative diagrams. In our calculation, diagrams containing a neutral Higgs boson coupling to top-quark and squark loops and decaying to a pair of weakinos are included. Resonance effects of these Higgs particles in  $s$ -channel diagrams are regulated by a finite Higgs width. We have used FEYNARTS 3.9 [140] to generate the virtual diagrams and FORMCALC 9.4 [139] to calculate the amplitudes in the Feynman-'t Hooft gauge using the MSSM-CT model file of Ref. [151].

For the regularization of ultraviolet (UV) divergences we follow the procedure described in Sec. 2.2.2. We note that the entire calculation is done in  $D = 4 - 2\epsilon$  dimensions, which is known to break supersymmetry at the level of the gauge inter-

actions. Therefore, a finite SUSY restoring counterterm at NLO has to be inserted, see Sec. 2.2.6. In order to cancel the UV divergences we perform a renormalization procedure and calculate the suitable counterterms necessary to define finite physical input parameters. Representative counterterm diagrams are given in Fig. 3.19. Self-energy diagrams that are necessary to fix the renormalization constants are depicted in Fig. 3.8 and Fig. 3.20.

Since we have to use the complex mass scheme (c.f. Sec. 2.2.7) to regularize the single resonance that are already present at Born level, arguments of loop integrals are complex. Therefore, loop integrals can no longer be evaluated by LOOPTOOLS, but the more sophisticated library COLLIER [170] has to be used to numerically evaluate scalar and tensor one-loop integrals. To this end, we have devised a FORTRAN code<sup>6</sup> which provides the interface between the COLLIER library and the FORMCALC matrix elements.

### 3.3.2 Additional renormalization constants

When calculating renormalization constants for the process  $pp \rightarrow \tilde{\chi}_i \tilde{\chi}_j + \text{jet}$  with FEYNARTS, renormalizing the strong coupling constant  $g_s$  needs additional attention. Originally FEYNARTS was developed only for electroweak corrections, so the model files provided with FEYNARTS are in some cases not suitable to generate the correctly renormalized and UV-finite amplitudes. Let us consider in the following how to determine the renormalization constant  $Z_{g_s}$  of the strong coupling constant  $g_s$  which is related to the bare coupling constant  $g_{s,0}$  via

$$g_{s,0} \equiv Z_{g_s} g_s, \quad (3.48)$$

or similarly in the leading divergences expansion (c.f. Eq. (2.35))

$$g_{s,0} = (1 + \delta Z_{g_s}) g_s, \quad (3.49)$$

where  $\delta Z_{g_s}$  is a new renormalization constant. The renormalization of the strong coupling constant is done in the  $\overline{\text{MS}}$ -scheme (c.f. Sec. 2.2.5). The general renormalization procedure was earlier described in Sec. 2.2.2. To find an expression for the renormalization constant  $Z_{g_s}$ , it is sufficient to focus only on incoming SM particles<sup>7</sup>. Each tree-level vertex where a gluon is involved leads to a different representation

<sup>6</sup>`weakinos-jet/Tools/collier/lt_collier_interface_complex.F90`

<sup>7</sup>It is possible to calculate  $Z_{g_s}$  also with external SUSY particles. However, since the Feynman rules for SUSY interactions are usually more complicated, this would unnecessarily complicate the calculation.

of  $Z_{g_s}$ . We can therefore choose the expansion of  $Z_{g_s}$  which is the easiest one to calculate. The different representations of the renormalization constant  $Z_{g_s}$  can be put into relationship by the Slavnov-Taylor identities [171–173].

For completeness, we here give the different representations of the renormalization constant  $Z_{g_s}$  in the Feynman-'t Hooft gauge<sup>8</sup> in regard to the QCD vertices where a gluon is involved:

$$\begin{aligned}
 g_{s,0} &\equiv Z_{g_s} g_s \\
 &= Z_{1g,a} (Z_\psi^L)^{-1/2} (Z_\psi^R)^{-1/2} Z_{gg}^{-1/2} g_s && \text{(gluon-quark vertex)} \\
 &= Z_{1g,b} Z_\xi^{-1} Z_{gg}^{-1/2} g_s && \text{(gluon-ghost vertex)} \\
 &= Z_{3g} Z_{gg}^{-3/2} g_s && \text{(three-gluon vertex)} \\
 &= Z_{4g}^{1/2} Z_{gg}^{-2} g_s && \text{(four-gluon vertex)}. \tag{3.50}
 \end{aligned}$$

$Z_{gg}$  and  $Z_\psi$  are the field renormalization constants of the gluon and quark, respectively, and  $Z_\xi$  belongs to the field renormalization constant of the QCD ghost. We define  $Z_{1g,a/b}$ ,  $Z_{3g}$  and  $Z_{4g}$  as the renormalization constants of the vertex where one, three, or four gluons are incoming.

These relations are called Slavnov-Taylor identities and they basically hold due to color charge conservation. The Slavnov-Taylor identities are similar to the Ward identities of quantum electrodynamics (QED). After an expansion by leading divergences, that is using  $Z_i = 1 + \delta Z_i$ , where  $Z_i$  comprises all possible renormalization constants, we obtain:

$$\begin{aligned}
 \delta Z_{g_s} &= \delta Z_{1g,a} - \frac{1}{2} \delta Z_\psi^L - \frac{1}{2} \delta Z_\psi^R - \frac{1}{2} \delta Z_{gg} \\
 &= \delta Z_{1g,b} - \delta Z_\xi - \frac{1}{2} \delta Z_{gg} \\
 &= \delta Z_{3g} - \frac{3}{2} \delta Z_{gg} \\
 &= \frac{1}{2} \delta Z_{4g} - 2 \delta Z_{gg}. \tag{3.51}
 \end{aligned}$$

In QED, the Ward identity can be used to simplify the relation between the field renormalization constant of the photon  $Z_\gamma$  and the field renormalization constant of the electron  $Z_\psi$ . We may think that the identity  $Z_\gamma (Z_\psi^L)^{-1/2} (Z_\psi^R)^{-1/2} = 1$ , which is true for QED, applies also to the case of QCD. If we would apply the equivalent

---

<sup>8</sup>Note that the renormalization constants introduced in the identities are in principle gauge-dependent.



### 3.3 Weakino-pair plus jet production

identity  $Z_{1g,a}(Z_\psi^L)^{-1/2}(Z_\psi^R)^{-1/2} = 1$  to Eq. (3.51), we would obtain

$$\delta Z_{g_s} = -\frac{1}{2}\delta Z_{gg}, \quad (3.52)$$

which is the renormalization constant of the strong coupling parameter originally used in the SMQCD model file by FEYNARTS. However, this relation is not true for QCD anymore. Instead we use the third Slavnov-Taylor identity of Eq. (3.51), since the individual terms are easy to calculate. Thus, the correct representation of  $\delta Z_{g_s}$  in the  $\overline{\text{MS}}$ -scheme is

$$\delta Z_{g_s} = -\frac{3}{2}\delta Z_{gg}|_{\text{div}} + \delta Z_{3g}, \quad (3.53)$$

with  $\delta Z_{gg}|_{\text{div}}$  being the divergent part of the gluon field renormalization constant. The gluon field renormalization constant is calculated automatically by FEYNARTS and it is given in the MSSM by

$$Z_{gg}|_{\text{div}} = -\frac{3}{4\pi}\alpha_s\Delta. \quad (3.54)$$

In the  $\overline{\text{MS}}$  scheme,  $\Delta$  is equal to  $1/\varepsilon - \gamma_E + \ln 4\pi$ . The quantity  $\gamma_E$  is the Euler-Mascheroni constant.

The counterterm of the three-gluon vertex  $\delta Z_{3g}$  is model-dependent and have to be calculated by hand. The result can be inserted globally into the respective FEYNARTS model file. In order to calculate the counterterm of the three-gluon vertex  $\delta Z_{3g}$ , we define the strong coupling constant as the full three-gluon coupling for on-shell external particles in the Thomson limit. In the Thomson limit all corrections vanish for momentum transfer  $q = p_1 - p_2$  equal to zero, where  $p_1$  and  $p_2$  are the incoming and outgoing momenta of the gluons, respectively. We get the condition

$$\Gamma^{\mu\nu\rho}(q=0) = -\delta Z_{3g} g_s f^{abc} (p_1^\mu g^{\nu\rho} + p_1^\nu g^{\mu\rho} - 2p_1^\rho g^{\mu\nu}), \quad (3.55)$$

where  $\Gamma^{\mu\nu\rho}$  is the three-gluon vertex including all possible loops and  $f^{abc}$  is the  $\text{SU}(3)_C$  structure constant. More details on the Thomson limit are given in Fig. 3.21. The loop corrections  $\Gamma^{\mu\nu\rho}$  can be calculated by hand for the simple SM-QCD case or by FEYNARTS and FORMCALC if supersymmetric particles have to be considered. Finally, the renormalization constant of the three-gluon vertex in the MSSM reads

$$\delta Z_{3g} = -\frac{3}{2\pi}\alpha_s\Delta. \quad (3.56)$$

To account for the decoupling of heavy particles in the running of the strong coupling constant  $\alpha_s$ , an additional finite shift in Eq. (3.53) has to be made. The

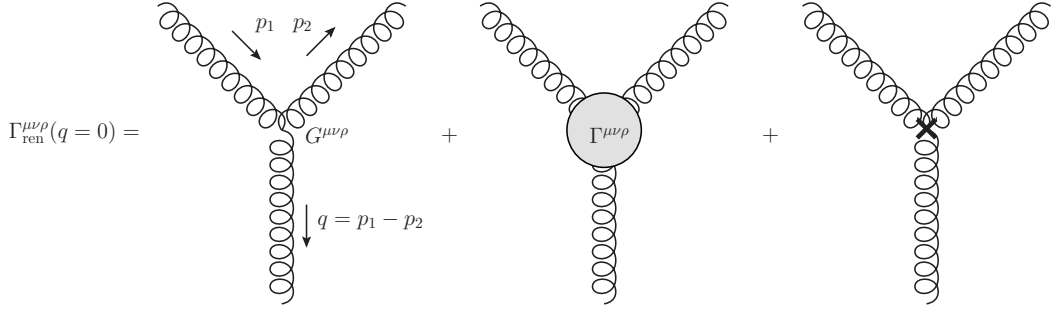


Figure 3.21: The renormalized three-gluon vertex. It decomposes into the tree-level contribution  $G^{\mu\nu\rho}$ , the loop corrections  $\Gamma^{\mu\nu\rho}$  and the counterterm  $\delta Z_{3g}\Gamma^{\mu\nu\rho}$ . We set the external momentum on-shell and the momentum transfer  $q = p_1 - p_2$  equal to zero in the Thomson limit.

decoupling of heavy particles has first been discussed in Ref. [174]. We define the renormalization constant of the strong coupling constant with the additional finite shift as

$$\delta Z_{g_s} = -\frac{3}{2}\delta Z_{gg}|_{\text{div}} + \delta Z_{3g} + \delta Z_{\text{log}}. \quad (3.57)$$

This finite shift by  $\delta Z_{\text{log}}$  can be understood as follows.

The renormalization counterterm for the strong coupling constant can be associated with the  $\beta$ -function, defined by the renormalization group equation of QCD introduced in Eq. (2.1),

$$\mu_R^2 \frac{d}{d\mu_R^2} \alpha_s = \beta(\alpha_s) = -\alpha_s^2 \sum_n \beta_n \alpha_s^n, \quad (3.58)$$

where  $\mu_R$  is the renormalization scale. At the one-loop order we have (see, for example, Refs. [101, 175])  $\delta Z_{g_s} = -\alpha_s \Delta\beta_0/2$ . With Eq. (3.53) and (3.56), this means  $\beta_0 = 3/4\pi$ , and all particles, including the heavy states, are contributing to the running of  $\alpha_s$ , leading to potentially large logarithms, if the scale  $\mu_R$  is significantly different from the masses of the various heavy states of the theory. In the SM with only four active flavors contributing to the running of  $\alpha_s$ , we have  $\beta_0^{\text{light}} = 25/12\pi$ . Following Refs. [101, 175, 176], the heavier states can be subtracted by rescaling  $\alpha_s$  so that only the light four active quark flavors contribute to the running of  $\alpha_s$  as in the SM, with the bottom and top quarks taken as massive, decoupled particles. This can be achieved in our calculation by adding the finite term  $\delta Z_{\text{log}}$  to the strong coupling constant counterterm, to subtract the logarithms that arise from the masses

of squarks ( $m_{\tilde{q}_i}$ ), gluino ( $m_{\tilde{g}}$ ), top quark ( $m_t$ ) and bottom quark ( $m_b$ ),

$$\delta Z_{\log} = -\frac{\alpha_s}{8\pi} \left[ 2 \ln \frac{m_{\tilde{g}}^2}{\mu_R^2} + \frac{1}{6} \sum_{i=1}^{12} \ln \frac{m_{\tilde{q}_i}^2}{\mu_R^2} + \frac{2}{3} \ln \frac{m_t^2}{\mu_R^2} + \frac{2}{3} \ln \frac{m_b^2}{\mu_R^2} \right]. \quad (3.59)$$

With this shift the one-loop running of  $\alpha_s$  with four light degrees of freedom is recovered:

$$\begin{aligned} \mu_R^2 \frac{d}{d\mu_R^2} \alpha_s &= -\alpha_s \left[ \beta_0 - \frac{1}{4\pi} \left( -2 - 2 - \frac{2}{3} - \frac{2}{3} \right) \right] \\ &= -\alpha_s \beta_0^{\text{light}}. \end{aligned} \quad (3.60)$$

Other fundamental parameters emerging in our calculation, such as the electroweak coupling constant, do not require renormalization at NLO in QCD.

### 3.3.3 Real corrections

The calculation of the real-emission corrections to weakino-pair production in association with a jet requires the evaluation of all partonic subprocesses contributing to the reaction  $pp \rightarrow \tilde{\chi}_i \tilde{\chi}_j jj$ . This includes quark–anti-quark annihilation processes with two gluons in the final state and all possible crossed modes, as well as the additional class of processes with two (anti-)quarks in the initial and in the final state.

Matrix elements for all of these subprocesses can in principle be generated with the help of automated tools, such as the generator provided by the POWHEG-BOX based on MADGRAPH 4, or the FEYNARTS/FORMCALC packages. However, as in the case of the simpler weakino-pair production process, problematic on-shell resonances occur in the real matrix elements. Thus, automated tools can only be used up to a certain degree. Representative diagrams contributing to the real-emission corrections are given in Fig. 3.22.

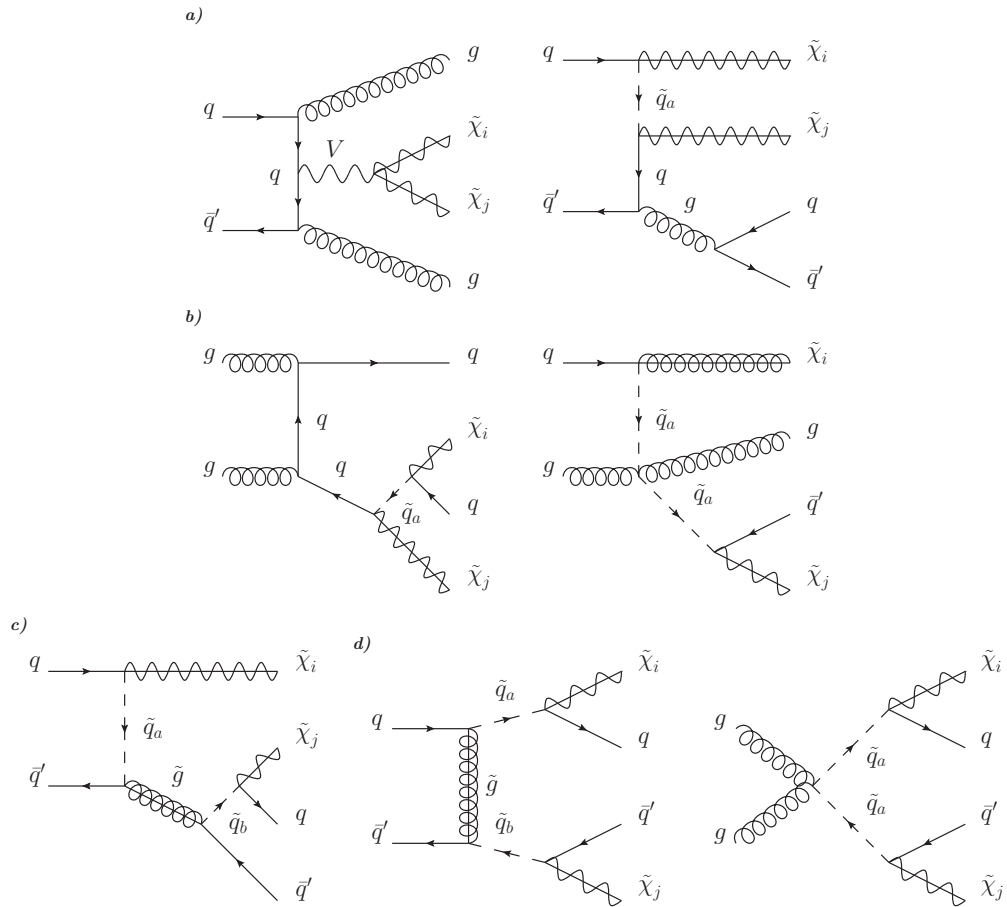


Figure 3.22: Representative (a) non-resonant, (b) squark singly-resonant, (c) gluino singly-resonant, and (d) squark doubly resonant real-emission diagrams for the production of a pair of weakinos with a jet.

### 3.3.4 On-shell resonances

For weakino-pair plus jet production, on-shell resonant structures occur already at Born level. However, these resonances are not problematic since we are using the complex mass scheme. Thus, particle widths are introduced into the propagators by means of complex mass parameters. Although on-shell resonances are a genuine part of the Born and virtual diagrams that contribute to the cross section, new singly and doubly on-shell resonant channels open up and may dominate the real-emission contributions. In particular, this includes the associated production of gluinos or squarks that subsequently decay into a weakino and a parton. Examples of diagrams

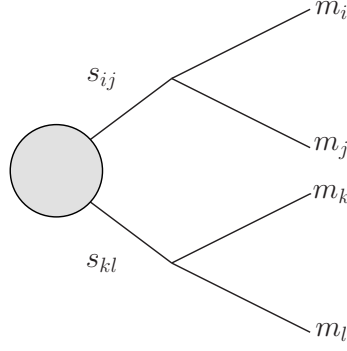


Figure 3.23: Final-state topology of a doubly resonant diagram for the production of the particle pairs  $(i, j)$  and  $(k, l)$ .

that can become singly or doubly resonant in specific regions of the SUSY parameter space are shown in Fig. 3.22 (b,c) and Fig. 3.22 (d), respectively.

The perturbatively meaningful and numerically stable evaluation of these contributions that are associated with Born processes different from  $pp \rightarrow \tilde{\chi}_i \tilde{\chi}_j j$  requires the design of a well-defined subtraction procedure similar to the method used for weakino-pair production. For the treatment of single resonances the subtraction scheme developed for weakino-pair production (c.f. Sec. 3.2.3) can be used without significant changes in the procedure, while double resonances require a more sophisticated scheme for which we use the results of Sections 3.1.1 to 3.1.4.

We want to recap the basic formulas that are needed for the subtraction of double on-shell resonances in the following. The counterterm for double on-shell resonances is of the form

$$\begin{aligned} \left| \mathcal{M}_{\text{res}}^{\text{CT}}(\Gamma_{\text{reg}}) \right|^2 &= \Theta \left( s - (m_{ij} + m_{kl})^2 \right) \Theta (m_{ij} - m_i - m_j) \Theta (m_{kl} - m_k - m_l) \\ &\quad \times \text{BW} \times \left| \mathcal{M}_{\text{res}}(\Gamma_{\text{reg}}) \right|_{\text{remapped}}^2, \end{aligned} \quad (3.61)$$

where the Breit-Wigner factor is given by

$$\begin{aligned} \text{BW} &= \left[ m_{ij}^2 m_{kl}^2 \Gamma_{ij}^2 \Gamma_{kl}^2 (m_{ij}(\Gamma_{ij} + \Gamma_{\text{reg}}) + m_{kl}(\Gamma_{kl} + \Gamma_{\text{reg}}))^2 \right. \\ &\quad \times \left. \left( (s_{ij} + s_{kl} - m_{ij}^2 - m_{kl}^2)^2 + (m_{ij}\Gamma_{ij} + m_{kl}\Gamma_{kl})^2 \right) \right] / \\ &\quad \left[ \left( (s_{ij} - m_{ij}^2)^2 + m_{ij}^2 \Gamma_{ij}^2 \right) \left( (s_{kl} - m_{kl}^2)^2 + m_{kl}^2 \Gamma_{kl}^2 \right) (m_{ij}\Gamma_{ij} + m_{kl}\Gamma_{kl})^2 \right. \\ &\quad \times \left. \left. \left( (s_{ij} + s_{kl} - m_{ij}^2 - m_{kl}^2)^2 + (m_{ij}(\Gamma_{ij} + \Gamma_{\text{reg}}) + m_{kl}(\Gamma_{kl} + \Gamma_{\text{reg}}))^2 \right) \right] \right]. \end{aligned} \quad (3.62)$$

Here,  $s$  denotes the partonic center-of mass energy, and  $m_a$  ( $a = (ij), (kl)$ ) the mass of an on-shell particle. The momenta entering  $\mathcal{M}_{\text{res}}$  in the on-shell counterterm are to be remapped to the on-shell kinematics of the resonant particles, c.f. Sec. 3.1.3.

Inserting the regulator  $\Gamma_{\text{reg}}$  into the real matrix element needs special care. To comply with the requirements of the doubly on-shell resonant counterterm, the resonant part of the real matrix element has to be rewritten according to Eq. (3.13) and Eq. (3.14),

$$\mathcal{M}_{\text{res}} = \frac{B_0}{s_{ij} - m_{ij} + s_{kl} - m_{kl} + im_{ij}(\Gamma_{\text{reg}} + \Gamma_{ij}) + im_{kl}(\Gamma_{\text{reg}} + \Gamma_{kl})} \quad (3.63)$$

$$\times \left( \frac{1}{s_{ij} - m_{ij} + im_{ij}\Gamma_{ij}} + \frac{1}{s_{kl} - m_{kl} + im_{kl}\Gamma_{kl}} \right),$$

which is achieved by editing the analytic expressions of the matrix elements by a suitable replacement rule<sup>9</sup> in FORMCALC.

Similar to the singly resonant case, the cross section corresponding to the on-shell subtracted resonant terms in the doubly resonant case is obtained by subtracting the counterterm from the resonant matrix element and summing over all possible resonant channels:

$$\sigma_{\text{real}}^{\text{OS}} = \sum_{\text{res}} \int d\Phi_4 \left[ |\mathcal{M}_{\text{res}}(\Gamma_{\text{reg}})|^2 - \mathcal{J}_{\text{res}} \left| \mathcal{M}_{\text{res}}^{\text{CT}}(\Gamma_{\text{reg}}) \right|^2 \right], \quad (3.64)$$

where the Jacobian factor  $\mathcal{J}_{\text{res}}$  derived in Sec. 3.1.4 reads

$$\mathcal{J}_{\text{res}} = \frac{s_{ij}s_{kl}}{m_{ij}^2 m_{kl}^2} \frac{\lambda^{1/2}(s, m_{ij}^2, m_{kl}^2)}{\lambda^{1/2}(s, s_{ij}, s_{kl})} \frac{\lambda^{1/2}(m_{ij}^2, m_i^2, m_j^2)}{\lambda^{1/2}(s_{ij}, m_i^2, m_j^2)} \frac{\lambda^{1/2}(m_{kl}^2, m_k^2, m_l^2)}{\lambda^{1/2}(s_{kl}, m_k^2, m_l^2)}$$

$$\times \frac{(\sqrt{s} - m_{ij})^2 - (m_k + m_l)^2}{(\sqrt{s} - \sqrt{s_{ij}})^2 - (m_k + m_l)^2}. \quad (3.65)$$

Here,  $\lambda$  denotes the usual Kaellen-function  $\lambda(x, y, z) = x^2 + y^2 + z^2 - 2(xy + yz + zx)$ , and  $d\Phi_4$  is the full  $2 \rightarrow 4$  phase-space measure. Since the real-emission amplitudes require a special treatment for the removal of the doubly on-shell resonant contributions, obtaining them with the POWHEG-BOX built-in tool based on MADGRAPH 4 was not possible. We thus have used a modified version of FEYNARTS and FORMCALC for the generation of the real-emission amplitudes and the identification of their resonance structure. The technical details of these modifications, along with a simple example, are given in the App. E.

<sup>9</sup>The replacement rule is defined as  $\text{Den}(s_{ij}, m_{ij}^2 - im_{ij}\Gamma_{ij})\text{Den}(s_{kl}, m_{kl}^2 - im_{kl}\Gamma_{kl}) \rightarrow \left[ \text{Den}(s_{ij}, m_{ij}^2 - im_{ij}(\Gamma_{ij} + \Gamma_{\text{reg}}))^{-1} + \text{Den}(s_{kl}, m_{kl}^2 - im_{kl}(\Gamma_{kl} + \Gamma_{\text{reg}}))^{-1} \right]^{-1} \times \left[ \text{Den}(s_{ij}, m_{ij}^2 - im_{ij}\Gamma_{ij}) + \text{Den}(s_{kl}, m_{kl}^2 - im_{kl}\Gamma_{kl}) \right]$ , where  $\text{Den}(x, y) \equiv 1/(x - y)$  is the internal representation of the propagator in FORMCALC.

### 3.3 Weakino-pair plus jet production

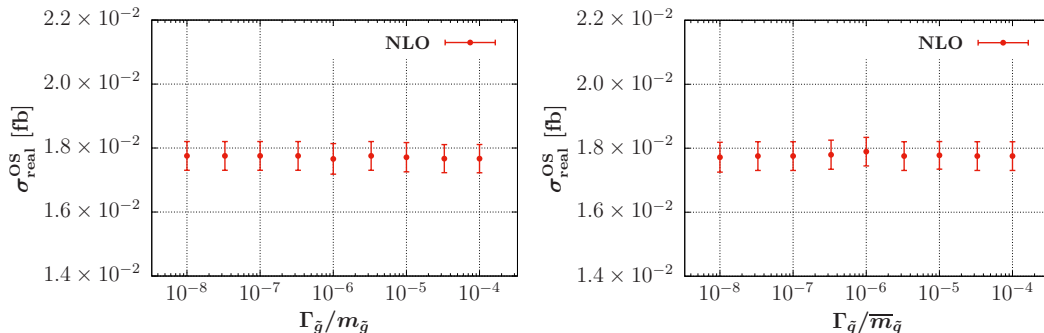


Figure 3.24: Dependence of the real on-shell contribution  $\sigma_{\text{real}}^{\text{OS}}$  to the cross section for the process  $pp \rightarrow \tilde{\chi}_1^0 \tilde{\chi}_1^+ j$  with  $\sqrt{s} = 14$  TeV on the technical regulator  $\Gamma_{\tilde{g}}$  (left) and  $\Gamma_{\text{reg}}$  (right).

#### 3.3.5 Numerical checks

To verify the validity of our calculation, we have performed a number of numerical checks. As in the case of weakino-pair production, we numerically compared the Born and real amplitudes generated by the independent programs MADGRAPH and FORMCALC. We found perfect agreement up to double precision which indicates that the amplitudes were set up correctly. We have tested that real-emission and IR subtraction terms approach each other for collinear momentum configurations which is a requirement for the cancellation of IR divergences (c.f. Sec. 2.3.2).

The dependence of our predictions for weakino-pair plus jet production cross sections on the technical regulator  $\Gamma_{\text{reg}}$  is negligible. Figure 3.24 illustrates the regulator dependence of the on-shell resonant part of neutralino-pair production in association with a jet for a SUSY benchmark point that features squarks heavy enough to on-shell decay into a neutralino and a quark. Using the average of the four squark masses of the first generation,  $\overline{m}_{\tilde{q}} = 1.67$  TeV, and the gluino mass  $m_{\tilde{g}} = 1.78$  TeV, we find that in the range  $\Gamma_{\text{reg}}/\overline{m}_{\tilde{q}} = 10^{-8}$  to  $10^{-4}$  and  $\Gamma_{\tilde{g}}/m_{\tilde{g}} = 10^{-8}$  to  $10^{-4}$ , the dependence of the cross section on the regulator is entirely negligible, thus confirming the stability of the applied on-shell subtraction procedure. Since the BW-factor of the double resonant counterterm does not vanish for  $\Gamma_{\text{reg}} \rightarrow 0$  as in the case of single resonances, gauge invariance is in principle not restored for small regulator widths. Fortunately, the doubly resonant diagrams of the real corrections of weakino-pair plus jet productions are gauge invariant by themselves as we have checked analytically. Thus, the on-shell counterterm which is based on the doubly resonant diagrams is gauge invariant and therefore the proposed on-shell subtraction

method preserves gauge invariance for the processes under consideration.

Finally, we have computed inclusive cross sections at LO and NLO accuracy for the pair production of the lightest neutralino in association with a jet in the setup of Ref. [177] and found good agreement with the published results within the range of one percent. It is important to mention that the calculation described in Ref. [177] does not include on-shell resonances, which we accounted for when comparing the results. Contributions of on-shell diagrams may be small for many SUSY parameter points and can be neglected in such cases, but they are essential for a consistent calculation in the most general case, as some allowed corners of the SUSY spectrum may lead to on-shell resonances.

### 3.3.6 Phenomenological setup and results

A public release of the code for the production of a weakino pair with an additional identified jet was made available in the framework of the POWHEG-BOX via the project website <http://powhegbox.mib.infn.it><sup>10</sup>. In this section we intend to highlight representative phenomenological results in order to demonstrate the capabilities of our code.

### 3.3.7 Choice of the spectrum and input parameters

In order to calculate the physical SUSY spectrum and to obtain a SUSY Les Houches Accord (SLHA) file [163, 164] as input to our code, we chose a parameter point in the framework of the pMSSM10 [68] that is still allowed by current experimental limits on SUSY. The pMSSM10 is defined at the SUSY scale  $M_{\text{SUSY}} = \sqrt{m_{\tilde{t}_1} m_{\tilde{t}_2}}$ , where  $\tilde{t}_1$  and  $\tilde{t}_2$  are the two stop mass-eigenstates, with ten soft SUSY breaking parameters, namely: the gaugino masses  $M_1, M_2, M_3$ , the first- and second-generation squark masses that are taken to be equal,  $m_{\tilde{q}_1} = m_{\tilde{q}_2}$ , the third-generation squark mass  $m_{\tilde{q}_3}$ , a common slepton mass for the three generations  $m_{\tilde{\ell}}$ , a common trilinear mixing parameter  $A$  for the three generations, the Higgsino mass parameter  $\mu$ , the pseudo-scalar mass  $M_A$ , and  $\tan\beta$ , the ratio between the two vacuum expectation values of the Higgs fields. Left- and right-handed sfermion soft breaking masses are taken to be equal.

We have chosen a scenario in which the LSP is the lightest neutralino, with a reasonably low mass so that the production cross section is not too low. This has

---

<sup>10</sup>Additional useful programs and scripts that were used to generate the calculation of weakino-pair plus jet production can be found on <https://github.com/MKesenheimer/weakinos-jet>.



### 3.3 Weakino-pair plus jet production

in particular lead to the following values of the ten parameters highlighted above,

$$\begin{aligned}
M_1 &= -120 \text{ GeV}, & M_2 &= 160 \text{ GeV}, & M_3 &= 1.70 \text{ TeV}, \\
m_{\tilde{q}_1} &= 1.79 \text{ TeV}, & m_{\tilde{q}_3} &= 1.30 \text{ TeV}, & m_{\tilde{\ell}} &= 740 \text{ GeV}, & A &= 1.863 \text{ TeV}, \\
\mu &= 190 \text{ GeV}, & M_A &= 1.35 \text{ TeV}, & \tan \beta &= 35.
\end{aligned}
\tag{3.66}$$

We have used the `SoftSUSY 4.0` program [70] for the calculation of the spectrum, and the `SDECAY 1.3` program [166] for the calculation of the relevant decay widths and branching fractions to obtain the SLHA input file for our code in the POWHEG-BOX. Our electroweak input parameters are the  $Z$  boson mass,  $m_Z = 91.1876 \text{ GeV}$ , the electromagnetic coupling constant  $\alpha^{-1}(M_Z) = 127.934$ , and the Fermi constant,  $G_F = 1.16637 \times 10^{-5} \text{ GeV}^{-2}$ . The resulting neutralino masses are

$$m_{\tilde{\chi}_1^0} = 111.9 \text{ GeV}, \quad m_{\tilde{\chi}_2^0} = 129.3 \text{ GeV}, \quad m_{\tilde{\chi}_3^0} = 211.7 \text{ GeV}, \quad m_{\tilde{\chi}_4^0} = 245.6 \text{ GeV},
\tag{3.67}$$

and the chargino masses are

$$m_{\tilde{\chi}_1^\pm} = 130.9 \text{ GeV}, \quad m_{\tilde{\chi}_2^\pm} = 249.1 \text{ GeV}.
\tag{3.68}$$

The squark masses are equal for the first and second generation (and for up- and down-type squarks), but different for the third generation. They read

$$\begin{aligned}
m_{\tilde{d}_L/\tilde{s}_L} &= m_{\tilde{u}_L/\tilde{c}_L} = 1.836 \text{ TeV}, & m_{\tilde{d}_R/\tilde{s}_R} &= m_{\tilde{u}_R/\tilde{c}_R} = 1.833 \text{ TeV}, \\
m_{\tilde{b}_1} &= 1.330 \text{ TeV}, & m_{\tilde{b}_2} &= 1.346 \text{ TeV}, & m_{\tilde{t}_1} &= 1.229 \text{ TeV}, & m_{\tilde{t}_2} &= 1.423 \text{ TeV}.
\end{aligned}
\tag{3.69}$$

#### 3.3.8 Cross sections and distributions at the LHC

We consider proton-proton collisions at the LHC with a center-of-mass energy of  $\sqrt{s} = 14 \text{ TeV}$ . For the parton distribution functions (PDFs) of the proton we use for both the LO and NLO calculation the 'PDF4LHC15\_nlo\_nf4\_30' PDF set [159] with four active flavors as implemented in the LHAPDF library [160] with ID = 92000. We set the renormalization and factorizations scales,  $\mu_R$  and  $\mu_F$ , to be proportional to the sum of the masses of the weakinos  $\tilde{\chi}_A$  and  $\tilde{\chi}_B$  produced in the specific process under consideration,  $\mu_R = \mu_F = \xi\mu_0$  with  $\mu_0 = m_{\tilde{\chi}_A} + m_{\tilde{\chi}_B}$ , while the

scale parameter  $\xi$  is chosen to be one unless specifically stated otherwise. The fixed-order results are combined with the parton-shower program PYTHIA 6.4.25 [161] in which QED radiation, underlying event, and hadronization effects are switched off throughout. Partons arising from the real-emission contributions of the NLO-QCD calculation or from the parton shower are recombined into jets according to the anti- $k_T$  algorithm [121] as implemented in the FASTJET package [162] with  $R = 0.4$  and  $|\eta^{\text{jet}}| < 4.5$ .

In the following we discuss phenomenological results for neutralino-pair production in association with a hard jet,  $pp \rightarrow \tilde{\chi}_1^0 \tilde{\chi}_1^0 j$ , in two different setups. For the first one only basic jet selection cuts are applied on the transverse momentum  $p_T^{\text{jet}_1}$  and rapidity  $\eta^{\text{jet}_1}$  of the hardest identified jet,

$$p_T^{\text{jet}_1} > 20 \text{ GeV}, \quad |\eta^{\text{jet}_1}| < 4.5, \quad (3.70)$$

which results in a cross section of 1.37 fb at NLO accuracy. The second set of cuts is inspired by experimental mono-jet searches [178–180]. Here, in addition to a severe cut on the hardest jet, an additional cut on the missing transverse momentum  $p_T^{\text{miss}}$  is imposed,

$$p_T^{\text{miss}} > 100 \text{ GeV}, \quad p_T^{\text{jet}_1} > 80 \text{ GeV}, \quad |\eta^{\text{jet}_1}| < 2.8. \quad (3.71)$$

The missing transverse momentum is computed from the negative sum of detectable jets with a transverse momentum  $p_T^{\text{jet}} \geq 30 \text{ GeV}$  and  $|\eta^{\text{jet}}| < 2.8$ , similar to what is done in the experimental analyses. As the sum of the transverse momenta of the final-state particles needs to add to zero, this is effectively equivalent to the sum over the non-detected particles, more specifically the LSP and the softer jets.

Figure 3.25 illustrates the dependence of the LO and NLO cross sections within the cuts of Eq. (3.70) on the scale parameter  $\xi$ . To quantify the theoretical uncertainties which emerge from the unphysical renormalization and factorization scales, we have varied  $\mu_R$  and  $\mu_F$  in the range  $0.5\mu_0$  to  $2\mu_0$  around the default choice  $\mu_0 \equiv 2m_{\tilde{\chi}_1^0}$ . Since the LO cross section is already dependent on the strong coupling constant  $\alpha_s$ , neutralino-pair production in association with a jet depends not only on  $\mu_F$  via the parton distribution functions of the scattering protons, but also on the renormalization scale  $\mu_R$  entering the running of the strong coupling constant  $\alpha_s$ . At NLO, additional  $\mu_R$  dependence occurs in the form of loop diagrams. However, in the considered range  $0.5\mu_0$  to  $2\mu_0$  the NLO cross section changes by only about 3%, whereas the LO cross section changes by up to 14%. This indicates that the perturbative expansion is stable, and the scale uncertainty at NLO is reduced remarkably compared to the LO calculation.

### 3.3 Weakino-pair plus jet production

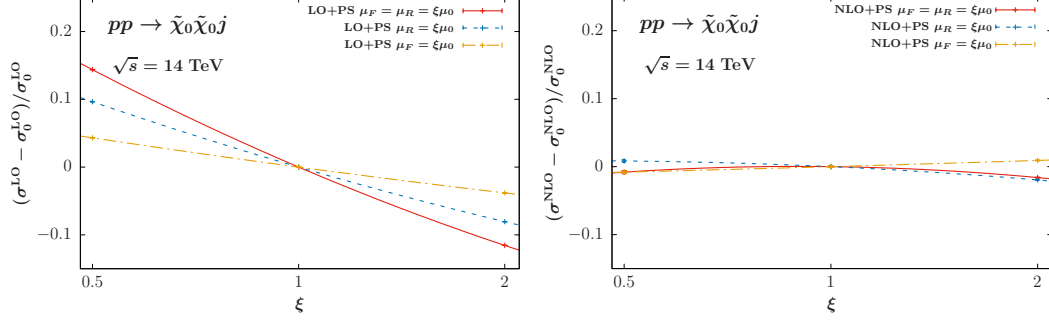


Figure 3.25: Dependence of the inclusive cross section for the process  $pp \rightarrow \tilde{\chi}_1^0 \tilde{\chi}_1^0 j$  with  $\sqrt{s} = 14$  TeV within the cuts of Eq. (3.70) on the factorization and renormalization scales. The curves show the deviation,  $(\sigma - \sigma_0)/\sigma_0$ , from the respective LO (left) or NLO (right) cross section,  $\sigma_0 = \sigma(\mu_R = \mu_F = \mu_0)$ , as a function of the scale parameter  $\xi$ , for three different cases:  $\mu_R = \mu_F = \xi\mu_0$  (solid red line),  $\mu_R = \xi\mu_0$ ,  $\mu_F = \mu_0$  (dashed blue line), and  $\mu_R = \mu_0$ ,  $\mu_F = \xi\mu_0$  (dot-dashed yellow line). In each case,  $\mu_0 = 2m_{\tilde{\chi}_1^0}$ .

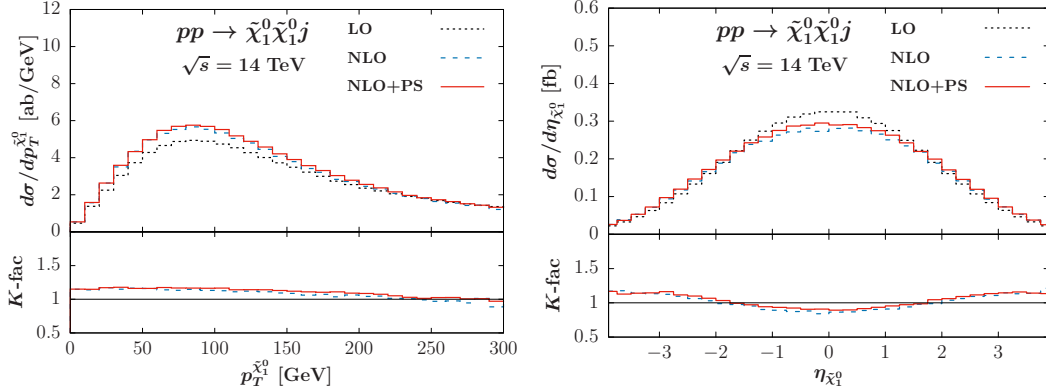


Figure 3.26: Average transverse momentum  $p_T^{\tilde{\chi}_1^0}$  (left) and pseudo-rapidity  $\eta_{\tilde{\chi}_1^0}$  distributions (right) of the two neutralinos in the process  $pp \rightarrow \tilde{\chi}_1^0 \tilde{\chi}_1^0 j$  at LO (dotted black lines), NLO (dashed blue lines), and NLO+PS (solid red lines) within the cuts of Eq. (3.70) for our default setup.

In Fig. 3.26 characteristic distributions of the two neutralinos for the inclusive setup of Eq. (3.70) are shown. In each case, the NLO prediction is significantly different from the respective LO curve. Adding the parton shower results in a small

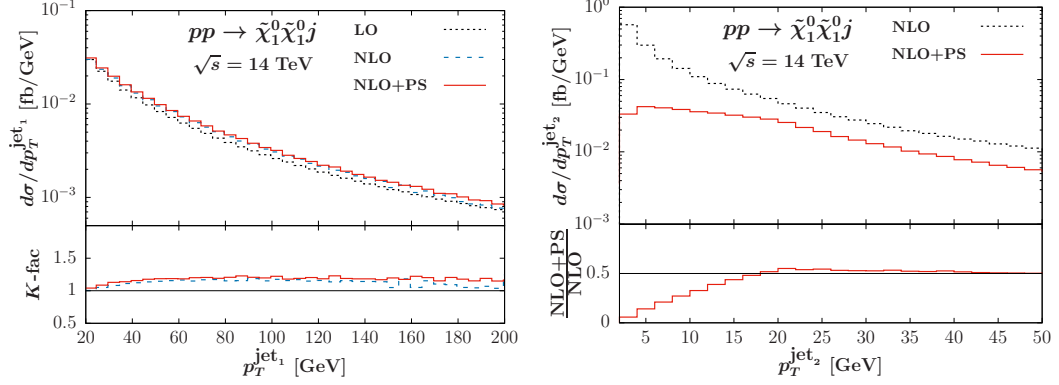


Figure 3.27: Transverse-momentum distribution of the hardest jet (left) and the second hardest jet (right) for the process  $pp \rightarrow \tilde{\chi}_1^0 \tilde{\chi}_1^0 j$  at LO (dotted black lines), NLO (dashed blue lines), and NLO+PS (solid red lines) for our default setup, after the cuts of Eq. (3.70) are applied.

increase of the associated cross section. In the transverse-momentum distribution of the two neutralinos the NLO corrections are largest in the low- $p_T$  range, amounting to almost 15% while they decrease to less than 5% in the tail of the distribution. The parton shower increases the distribution uniformly over the entire range by about 5%. In the average pseudo-rapidity distribution of the neutralinos, the corrections are negative in the central rapidity region, amounting to  $-15\%$ . Towards larger values of  $\eta_{\tilde{\chi}_1^0}$ , the corrections are positive and increase the LO result by 15%. Similar to the transverse-momentum distribution of the two neutralinos, the parton shower increases the  $\eta_{\tilde{\chi}_1^0}$ -distribution by 5% over the entire range. The transverse-momentum distribution of the hardest jet, depicted in Fig. 3.27, exhibits a behavior slightly different than of the neutralinos. NLO corrections are small in the bulk, but increase up to 15% in the tail of the distribution. Parton-shower effects modify the fixed-order NLO results by an additional 5%. Obviously, a constant  $K$ -factor would not account for these effects in each of these distributions.

While the distributions of the hardest jet can be described with full NLO accuracy by our calculation, the second-hardest jet is accounted for only by the real-emission contributions of the NLO-QCD corrections, and thus effectively only described with LO accuracy. Since no cuts are imposed on sub-leading jets in the setup we consider, it would be expected that the soft and collinear configurations dominate the behavior of such jets. This expectation is nicely confirmed for the transverse-momentum distribution of the second-hardest jet in Fig. 3.27. The curve associated with the

### 3.3 Weakino-pair plus jet production

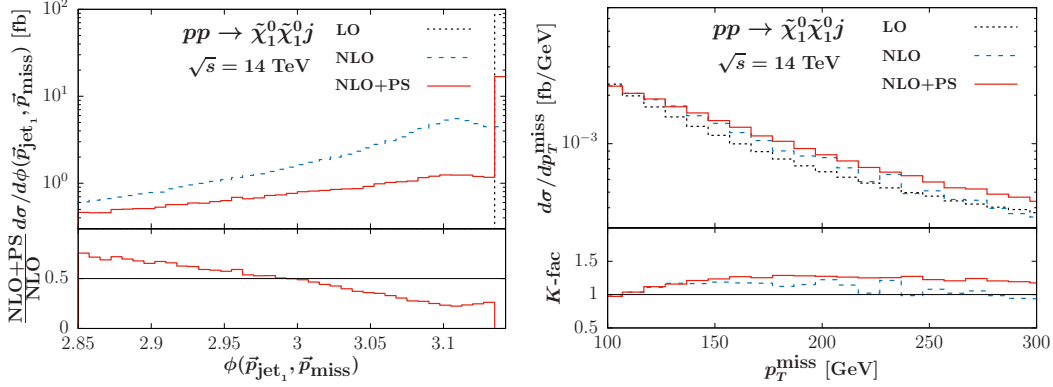


Figure 3.28: Angular separation  $\phi$  between the missing momentum  $\vec{p}_{\text{miss}}$  and the hardest jet momentum  $\vec{p}_{\text{jet}_1}$  vectors (left) and missing transverse momentum  $p_T^{\text{miss}}$  (right) for the process  $pp \rightarrow \tilde{\chi}_1^0 \tilde{\chi}_1^0 j$  at LO (dotted black lines), NLO (dashed blue lines) and NLO+PS (solid red lines), after the cuts of Eqs. (3.71) are applied.

NLO calculation increases rapidly towards small values of  $p_T^{\text{jet}_2}$  and exhibits a large negative entry in the lowest bin. The Sudakov factor of the NLO+PS implementation tames this increase.

Experimental searches for particles that cannot be directly identified in a default detector, such as neutralinos or, more generically, massive DM candidate particles, often rely on mono-jets. The tell-tale signature of such events consists in a hard jet that recoils off the system comprised by the heavy particles, accompanied by large missing transverse energy. To quantitatively account for such signatures an accurate description of the hard jet accompanying the heavy-particle system is of paramount importance. For the production of a neutralino pair in association with a hard jet that can give rise to a mono-jet signature we consider a scenario inspired by experimental searches with the cuts of Eq. (3.71). Figure 3.28 illustrates the features of two characteristic distributions for such a scenario: The angular separation  $\phi(\vec{p}_{\text{jet}_1}, \vec{p}_{\text{miss}})$  of the hardest jet and of the missing momentum  $\vec{p}_{\text{miss}}$ ; and the transverse component of the missing momentum,  $p_T^{\text{miss}}$ . At LO, the hard jet is produced back-to-back with the heavy neutralino system, resulting in an angular separation of  $180^\circ$ . At NLO, this back-to-back configuration can be altered by radiation effects due to real parton emission. Even more radiation occurs at the NLO+PS level, resulting in an additional smearing of the LO distribution and affecting in particular the last bin corresponding to  $\phi = 180^\circ$ . The  $p_T^{\text{miss}}$  distribution experiences a

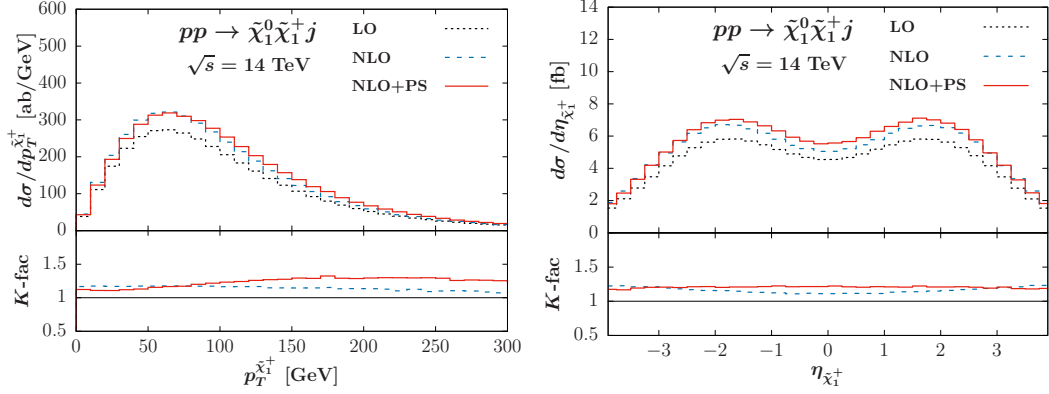


Figure 3.29: Transverse-momentum (left) and pseudo-rapidity distribution (right) of the chargino in the process  $pp \rightarrow \tilde{\chi}_1^0 \tilde{\chi}_1^+ j$  at LO (dotted black lines), NLO (dashed blue lines), and NLO+PS (solid red lines) within the cuts of Eq. (3.70) for our default setup.

pronounced increase from LO to NLO and NLO+PS. While the NLO corrections are moderate in the bulk, they amount to more than 15% beyond about 150 GeV. A description of this behavior by a constant K factor would clearly fail. The  $p_T^{\text{miss}}$  distribution is increased uniformly by another 10% from NLO to NLO+PS by the parton-shower.

While a major motivation for the investigation of weakino-pair production processes at hadron colliders is the search for Dark Matter, this class of reactions is interesting also per se for the study of SUSY interactions. The code package we have developed thus not only allows for simulations of neutralino-pair production in association with a hard jet, but also for production processes involving various combinations of charginos and neutralinos. To demonstrate this feature of our work, we present in Fig. 3.29 representative distributions of the chargino produced in the reaction  $pp \rightarrow \tilde{\chi}_1^0 \tilde{\chi}_1^+ j$  after the inclusive selection cuts of Eq. (3.70) are applied. We find that the NLO (SUSY-)QCD corrections to the transverse-momentum and pseudo-rapidity distributions of the chargino are similar in size to those for the related distributions in the case of neutralino-pair production (c.f. Fig. 3.26). While we refrain from such a study in this work, we would like to point out that event files produced with our code in the default Les Houches format can easily be processed with public Monte Carlo generators such as PYTHIA to simulate decays of the supersymmetric particles. In that case, not only distributions of the charginos, but also of their decay products can be simulated.

## 4 Conclusion and outlook

In this work, we have presented a new set of implementations for weakino-pair and weakino-pair plus jet production processes in the framework of the POWHEG-BOX. The newly developed codes allow for the calculation of the NLO SUSY-QCD corrections for the hard production processes, and provide an interface to parton-shower programs such as PYTHIA via the POWHEG method. The programs can process SLHA files obtained by an external spectrum calculator for the computation of a specific SUSY parameter point in the context of the MSSM. If desired, decay chains of the weakinos can be simulated with a dedicated option in PYTHIA.

We have described the technical aspects of the implementation specific to weakino-pair and weakino-pair plus jet production processes. In particular, a new method to subtract doubly on-shell resonant contributions appearing in the real matrix element of weakino-pair plus jet production has been developed. The subtraction method, and especially the FORTRAN routines necessary for the subtraction procedure, is process independent and can be applied with little to no changes to other pair-production processes with problematic double on-shell resonances in the real contributions.

Additional useful software packages and scripts have been extended or newly developed, for instance, a script to control the parallel execution of the POWHEG-BOX on a high-performance computer, a software package to generate phase space parametrizations with arbitrary multiplicity, and general FORTRAN routines to remap the momenta of the real matrix elements to on-shell conditions. Additionally, we have developed several scripts to set up the matrix elements of arbitrary processes within the POWHEG-BOX more easily. The computer code and the scripts were all made available on the website of the POWHEG-BOX<sup>1</sup> or on github<sup>2,3</sup>.

To illustrate the capabilities of the code packages, we have discussed phenomeno-

---

<sup>1</sup><http://powhegbox.mib.infn.it>

<sup>2</sup><https://github.com/MKesenheimer/weakinos>

<sup>3</sup><https://github.com/MKesenheimer/weakinos-jet>

#### 4 Conclusion and outlook

logical features of a few selected processes focusing on theoretical uncertainties and the impact of parton-shower effects on experimentally accessible observables for different SUSY parameter points. Any user of the code, however, is free to consider a SUSY spectrum of their own choice and obtain NLO+PS results for any set of observables within arbitrary selection cuts.

We have found that, in accordance with previous results reported in the literature, generally NLO corrections have a significant impact on production rates. Scale uncertainties of the NLO results are moderate, however. Parton-shower effects are small for weakino distributions, but are significant for jet observables, as expected. Thus, our work is of immediate relevance for mono-jet searches for dark matter at the LHC in the framework of the MSSM. Since the NLO+PS corrections have influence on distributions and productions rates, the current exclusion limits that rely mainly on LO calculations and flat  $K$ -factors may have to be adjusted. We therefore encourage everybody who is doing data analysis on the basis of Monte Carlo simulations to use the computer code we have developed.

Furthermore, there are a few possibilities to extend and improve our predictions. For instance, it would be interesting to take the electroweak corrections into account which would lead to corrections of order  $\alpha^3$  for weakino-pair, and  $\alpha^3\alpha_s$  for weakino-pair plus jet production. To account for newer experimental bounds on SUSY parameters, the analysis routines and the input parameters of our calculation might be adapted. An extensive analysis of weakino-pair plus jet production with the subsequent decay of the supersymmetric final-state particles would be another possibility to compute observables which are experimentally accessible. To this end, the Monte Carlo generators PYTHIA or HERWIG<sup>4</sup> might be used to simulate the decays of supersymmetric particles by processing the event files produced by our code. Moreover, it would be valuable to calculate the processes of weakino-pair and weakino-pair plus jet production in a model with currently less experimental restrictions. For example, in the next-to-minimal Supersymmetric Standard Model (NMSSM) [181, 182].

In addition to that, the performance of our code for weakino-pair and weakino-pair plus jet production could be improved by optimizing the evaluation of the amplitudes. This might be achieved by preprocessing the amplitudes analytically or by rearranging the code structure. What is more, unnecessary parts of the automatically generated code could be sorted out to save execution time.

---

<sup>4</sup><https://herwig.hepforge.org>



# Acknowledgement

First of all, I would like to thank Prof. Dr. Barbara Jäger for giving me the opportunity to compose my PhD thesis on this interesting topic. I appreciate her encouragement in providing me support in every regard. I am grateful for the good working atmosphere and for all the helpful advices she had in regard to technical issues, during the preparation of multiple talks and, of course, for the help with various administrative matters. I am very thankful for all the useful discussions.

Furthermore, I want to express my gratitude to Apl. Prof. Dr. Thomas Gutsche. He was amenable to questions that were not only technical nature. During my period as PhD student he cared a lot that I was able to follow my desire to teach and to pass my experience to younger students. He always had an anecdote handy, especially, when I had to clear my mind from an exhausting calculation.

I want to thank Dr. Julien Baglio who was not only the co-supervisor and a very helpful colleague, but also a secure climbing assistance. He was the expert who I could ask many theoretical and technical questions.

A special thanks goes out to the German Academic Scholarship Foundation (Studienstiftung des deutschen Volkes) for supporting my work and to the Institute of Theoretical Physics for giving me a place and the means for work. This work could be performed thanks to the support of the state of Baden-Württemberg by providing the necessary computer power through bwHPC.

I enjoyed sharing the office with Dr. Lukas Salfelder and Gabriele Coniglio, and I want to thank them for the many nice discussions about physics and non-physics related topics. The time spent in Tübingen during the work on my PhD thesis will always be in good memory thanks to a lot of collaborators, colleagues and friends: Dr. Christoph Borschensky, Dr. Tom Kaufmann, Martin Lambertsen, Felix Hekhorn, Dr. Junya Nakamura, Johannes Scheller, Robin Sellnow, Anton Stoyanov, Dr. Juraj Streicher, and Marina Walt. Furthermore, I want to thank Ingrid Estiry for her help with all the administrative business.

Thanks a lot to Barbara Jäger and Julien Baglio for proofreading this work.

Last but not least, I want to express my deepest gratitude to my family and my wife Sarah for their support during this time.



## Appendices



# A Compiling and initializing the code

## A.1 Preface

The provided software packages were tested and developed for the POWHEG-BOX-V2 revision 3361. The code was released under GPL3 license on

```

http://powhegbox.mib.infn.it/,
https://github.com/MKesenheimer/weakinos, and
https://github.com/MKesenheimer/weakinos-jet.

```

Any user is free to download the source files and to use them for own projects. If unexpected behavior during compilation or execution is examined, the version of the POWHEG-BOX-V2 should be updated to the revision the code was developed for. In order to do so, the following commands should be executed in the POWHEG-BOX-V2 main directory:

```

$ svn info
$ svn up -r3361.

```

More information about the general setup and installation of the POWHEG-BOX on <http://powhegbox.mib.infn.it/>.

The layout of the FORTRAN code is as follows. The main directories `weakinos` and `weakinos-jet` contain general files and scripts for the processes  $pp \rightarrow \tilde{\chi}_i \tilde{\chi}_j$  and  $pp \rightarrow \tilde{\chi}_i \tilde{\chi}_j + \text{jet}$ , respectively. The main directories `weakinos` and `weakinos-jet` are divided into the subdirectories `neuIneuJ(+jet)`, `neuIchaJ(+jet)` and `chaIchaJ(+jet)` that are specific for certain neutralino and chargino combinations. In the following we will refer to these directories as the process subdirectories.

## A.2 Dependencies

The following prerequisites have to be met to successfully compile the codes we have developed.

- A Linux or Unix-based operating system.
- A FORTRAN compiler. The `gfortran` compiler version 5 or newer is recommended (<https://gcc.gnu.org/wiki/GFortranBinaries>).
- The CMAKE build software version 2.8 or newer (<https://cmake.org>).

## Appendix A

- The FASTJET software package for finding jets version 3.1.3 or newer (<http://fastjet.fr>).
- The LHAPDF interface for accessing parton distribution functions version 6.1.5 or newer (<https://lhapdf.hepforge.org>).

### A.3 Compiling

After the POWHEG-BOX-V2 has been set up correctly and the `weakino` or `weakino-jet` project have been downloaded, the static libraries that are necessary to run the executable have to be built. The additional libraries which the code relies on are

```
libdheLas3.a,  
liblooptools.a or libcollier.a, and  
libSLHA.a.
```

To compile these libraries, the software has to be configured for the specific operating system. All necessary configuration scripts can be called by a single command:

```
$ ./configure [compiler],
```

where the optional parameter can be either `gfortran` or `ifort`. The libraries are compiled by calling

```
$ make libdheLas3.a  
$ make libcollier.a  
$ make libSLHA.a
```

or short

```
$ make libs.
```

If the user wishes to use libraries that are different from the libraries present in the frameworks of `weakino-pair` or `weakino-pair` plus jet production (for example if a specific version of a library is desired), the precompiled library can be copied into the directory `./Tools/`. Alternatively, the paths to the libraries have to be provided in the makefiles.

After the libraries have been compiled, the main executables of the respective process can be built. The makefiles for the main executables are located in the specific process subdirectory. To compile these executables, the makefiles have to be called via the commands

```
$ cd <process subdirectory>
$ make clean-results && make -j4 do
```

or

```
$ cd <process subdirectory>
$ make -j4 libs
$ make clean-results && make -j4 do
```

for weakino-pair or weakino-pair plus jet production, respectively. In the second case, separate libraries for the virtual and real matrix elements have to be generated in advance. This step could be abbreviated by calling another script which generates executables for all subprocesses at once:

```
$ ./make-all.sh -j4 libs.
```

The `./make-all.sh` script is located in the main directory of weakino-pair or weakino-pair plus jet production.

We want to make an important note for Mac OSX users here: In order to link the object files properly with newer compiler versions, it might be advisable to compile all libraries using the `-lstdc++` flag.

## A.4 Preprocessor flags

In the current version, several C preprocessor (CPP) flags were implemented. The preprocessor runs in traditional mode for `gfortran`. Any restrictions of the file-format, especially the limits on line length, apply for preprocessed output as well. Therefore, it might be advisable to use the

```
-ffree-line-length-none
```

or

```
-ffixed-line-length-none
```

options (activated as default). If a preprocessor flag is changed, it is imperative to delete the old object files by calling

```
$ make clean
```

before compiling the source code once again.

Preprocessor flags are used to choose between multiple process-relevant options and to save runtime. By the implemented preprocessor flags, unnecessary code is sorted out automatically and only the relevant code pieces are compiled by the

## Appendix A

FORTRAN-compiler. This mechanism is also used for debugging purposes in the weakino-pair and weakino-pair plus jet codes. The user can choose between different verbosity levels to print out debugging information. The debugging level can be chosen in the process specific makefile with the option

```
LEVEL = n,
```

where  $n$  is a number between 0 and 4. More debugging information is given during runtime by a higher number  $n$ .

To choose between the different on-shell subtraction methods (c.f. Sec. 3.1), the following preprocessor flags can be used:

```
DR_I, DR_II, DSUB_I, DSUB_II.
```

These flags are mandatory and should not be deleted. In particular, they refer to the diagram removal type I (DRI), diagram removal type II (DRII) and diagram subtraction methods. The diagram subtraction method is divided into two methods. The first method (DSUBI) removes only the on-shell parts of the real amplitudes, however, the on-shell parts of the matrix elements are not integrated over a separate phase space. Thus, the DSUBI method can be used for debugging and for cross-checks. The second method (DSUBII) is activated by default. It is the method which we have used in our phenomenological analysis of weakino-pair and weakino-pair plus jet production. On-shell contributions are subtracted by a sophisticated counterterm and the regular on-shell parts are integrated over a separate phase space.

These are only a few examples of the preferences and options we have implemented in our code. A more detailed overview of additional preferences and options can be found in the makefiles themselves.

### A.5 Running and cleaning

Executing the weakino and weakino-jet programs is simple. The programs can either be executed manually by changing into the directories `./testrun` (or every other directory which contains the file `powheg.input`) and running `./pwhg_main_*`, or by calling

```
$ make do
```

in the respective project subdirectory. This command compiles the source code and runs the program automatically in the default directory `./testrun`. Alternatively,



the script `./runparallel.sh` can be used to control the execution of the POWHEG-BOX. More details on the `runparallel.sh` script can be found in App. C. All SM and SUSY parameters are read in from a single `slha`-file located `./testrun`. Runtime variables specific for the POWHEG-BOX-V2, such as the number of integration points, the number of events to generate, etc., have to be specified in `powheg.input` (c.f. App. B).

After the POWHEG-BOX has finished the generation of the event files, the parton shower has to be applied to the event files. To this end, the PYTHIA executable provided by the POWHEG-BOX-V2 can be used. To build the PYTHIA executable, the command

```
$ main-PYTHIA-lhef
```

can be used. PYTHIA is executed by changing into the directory where the event files are located and by calling

```
$ ../main-PYTHIA-lhef.
```

Additional executables to modify the event files can be found in `./Tools/programs`.

To clean up the project directories, various possibilities exist. Old object files that are generated during the compilation process can be removed by calling

```
$ make clean.
```

This has no effect on the compiled program. If only the results of a previous run (including grid files) should be removed from the `./testrun` directory, the command

```
$ make clean-results
```

can be executed. The command

```
$ make clean-all
```

can be used to clean all compiled object files, the executables and the runtime files.



## B Input parameters for the weakino and weakino-jet executables

The execution of the POWHEG programs is controlled by several parameters that have to be given in the input file of the POWHEG-BOX. The input files (`powheg.input`) can be found in the run directories `testrun_*` of the respective process subdirectories. We will go through the most important parameters for the execution of the weakino-pair and weakino-pair plus jet production codes. More information about parameters that are not important for weakino-pair and weakino-pair plus jet production can be reviewed in Ref. [135]. We follow the same syntax of the usual parameter convention of the POWHEG-BOX, which is

```
keyword value ! comment.
```

Keyword-value pairs can be commented out by putting a '#' or '!' in front.

Since weakino-pair and weakino-pair plus jet production can be divided into multiple subprocesses, the user can choose from different final-state combinations. The choice is between the PDG numbers of the neutralinos ( $\tilde{\chi}_1 = 1000022$ ,  $\tilde{\chi}_2 = 1000023$ ,  $\tilde{\chi}_3 = 1000025$ ,  $\tilde{\chi}_4 = 1000035$ ) and the chargino numbers ( $\tilde{\chi}_1^+ = 1000024$ ,  $\tilde{\chi}_1^- = -1000024$ ,  $\tilde{\chi}_2^+ = 1000037$ ,  $\tilde{\chi}_2^- = -1000037$ ) and is controlled by

```
fin1 1000022 ! Particle ids for final state weakinos
fin2 1000022 ! PDG convention.
```

All physical parameters have to be given in a separate SUSY Les Houches Accord (SLHA) file. The choice of the SLHA file, the number of incoming and outgoing flavors, and the flavor scheme<sup>5</sup> are controlled by the keywords `SLHA`, `incomingflavors`, `outgoingflavors` and `flavorscheme`, respectively. Usually the numbers of incoming and outgoing flavors, and the flavor scheme are chosen to be equal. However, we have implemented different keywords for debugging purposes and to have a better way to control the execution of the code.

```
! name of the SLHA input-file
SLHA 'input_p10MSSMd.slha'
incomingflavors 4 ! max number of incoming flavors
outgoingflavors 4 ! max number of outgoing flavors
flavorscheme 4 ! the flavorscheme to work in.
```

---

<sup>5</sup>Note, we use five active flavors for weakino-pair and four active flavors for weakino-pair plus jet production.

## Appendix B

If the calculation is performed in a scheme with less than five incoming flavors, a massive bottom quark has to be used. Whether to use a massive or massless bottom quark is decided automatically by the code. However, the user can choose if the  $\overline{\text{MS}}$ -mass or the pole-mass of the bottom quark should be used. This behavior is controlled by the keyword

```
msbar 1 ! (default 1) whether to use (=1) the
        ! msbar mass for the bottom or not (=0).
```

Furthermore, the user can choose from different PDF sets (LHA numbering) for the incoming hadrons with the keywords `lhans1` and `lhans2`. The beam energy in GeV of the first and second hadron is controlled by `ebeam1` and `ebeam2`, respectively.

```
lhans1 92000 ! PDF4LHC15_nlo_nf4_30
lhans2 92000 ! PDF4LHC15_nlo_nf4_30
ebeam1 7000d0 ! energy of beam 1
ebeam2 7000d0 ! energy of beam 2.
```

Since the cross-section for weakino-pair plus jet production would diverge for vanishing transverse momentum  $k_T$  of the jet particle, a phase space generation cut is used. The minimum  $k_T$  in the underlying Born<sup>6</sup> process is implemented in two ways. The generation cut can be set to a hard-coded value in `init_couplings.f` or the value of the cut in GeV can be controlled by

```
bornktmin 10d0 ! generation cut.
```

The value of the regulator of the on-shell subtraction method (c.f. Sec. 3.1) is controlled by

```
ewi 1d-8 ! regulator for single on-shell resonances
for the case of weakino-pair production, and by
ewi1 0d0 ! regulator for single on-shell resonances
ewi2 0d0 ! regulator for double on-shell resonances.
```

for weakino-pair plus jet production. The regulators are given in terms of the average squark (`ewi` and `ewi2`) and gluino (`ewi1`) masses and are therefore dimensionless.

Parameters for the integration of the matrix elements over the  $n$ -particle phase spaces are given by `ncall1`, `itmx1`, `ncall2`, and `itmx2`. The on-shell contributions are integrated over a separate phase space and the respective parameters are

---

<sup>6</sup>Every real process is associated with a specific Born configuration which is determined by merging two final-state partons of the real configuration into one parton with the appropriate flavor and quark-type.

`ncall1osres`, `itmx1osres`, `ncall2osres`, and `itmx1osres`. In either case, `ncall1*` determines the number of points (n.o.p.) for the grid initializations, `itmx1*` the number of grid iterations, `ncall2*` the number of points for computing the integrals, and `itmx2*` the number of iterations for computing the integrals. To start with, good values for `ncall*` are between 1000-10000. These values should be increased if the number of failures for the inclusive cross-section is above 1% of the total number of events. The number of failures for the third and fourth stage is given in the files `pwgcounters-st3-*.dat` and `pwgcounters-st4-*.dat`, respectively. For high precision runs, up to 100 million points or more have to be evaluated. However, to save execution time, the jobs can be parallelized with the `runparallel.sh` script which is the topic of the following section.

```
! integration paramters
ncall1 2000 ! n.o.p. for grid initialization
itmx1 4 ! number of grid iterations
ncall2 2000 ! n.o.p. for computing the integral
itmx2 4 ! number of integral iterations
! on-shell resonances
ncall1osres 3000 ! n.o.p. for grid initialization
itmx1osres 4 ! number of grid iterations
ncall2osres 3000 ! n.o.p. for computing the integral
itmx2osres 4 ! number of integral iterations.
```

In the case of weakino-pair plus jet production, additional parameters to improve the numerical stability are necessary. The `fold*` parameters can be increased if the virtual time (given in `pwgcounters-st2-*.dat`) is much larger than the real time. By increasing these numbers, the real amplitudes are called more often and more statistic is collected in the real contributions.

```
foldcsi 5 ! number of folds on csi integration
foldy 5 ! number of folds on y integration
foldphi 5 ! number of folds on phi integration.
```

The number of calls to set up the upper bounding function and the number of events to generate are set by `nubound` and `numevts`. To obtain a good statistical behavior, around one million events have to be computed in total for weakino-pair and weakino-pair plus jet production.

```
nubound 1000 ! set up the norm of ubound
numevts 1000 ! number of events to generate.
```

## Appendix B

The user can set the factorization and renormalization scales  $\mu_F = \xi_F \mu_{\text{ref}}$  and  $\mu_R = \xi_R \mu_{\text{ref}}$  with respect to a central reference scale  $\mu_{\text{ref}}$  (by default given by the sum of the masses of the final-state particles) by providing the renormalization scale factor  $\xi_R$  (`renscfact`) and the factorization scale factor  $\xi_F$  (`facscfact`). Additionally, the user can choose between a running or a fixed scale. The running scale is calculated from the transverse momentum of the sum of the final-state particles. By default we use no running scale and for  $\mu_F$  and  $\mu_R$  the central scale  $\mu_{\text{ref}}$ , that is by setting `facscfact` and `renscfact` to one.

```
renscfact      1d0 ! muren = muref * renscfact
facscfact      1d0 ! mufact = muref * facscfact
runningscale  0   ! use ref. scale=virtuality Q.
```

The following parameters are optional. For debugging purposes and to skip the computation of the virtual amplitudes for grid generation, the flag `fakevirtu`als can be set. Note that this keyword is usually commented out. Whether the real amplitudes have the correct infrared behavior can be checked by the keywords `softtest` and `colltest`. The results of this check can be found in a file called `pwhg_checklimits`. Born results can be obtained by setting `bornonly` to one. The evaluation of the amplitudes can be sped up by setting the keyword `smartsig` equal to one. If multiple amplitudes are numerically equal, only one amplitude is evaluated at a given phase space point and the result is reused for the other amplitudes. Histograms of the NLO run (second stage) can be obtained by setting `testplots` to one.

```
#fakevirtu
```

als 1 ! generate the grid with fake virtuals  

```
softtest      1 ! check soft singularities
colltest      1 ! check collinear singularities
#bornonly     1 ! if 1 do Born only
smartsig      1 ! remember equal amplitudes
testplots     1 ! write data for gnuplot histograms.
```

The reweighting method of events is a key technique to save execution time. Event generation is usually very inefficient since events are calculated by rejection sampling, meaning that the momenta and interaction properties of the event are randomly generated. Only sets are accepted that fit to the predicted cross-section of the process. Each event comes with a certain weight which is proportional to the probability of this event. Reweighting is the process of calculating a scaling factor which can be combined with the original event weight to give a new weight which

would be correct if the event had been generated under some different set of free parameter values [183]. If the process comprises the evaluation of time consuming virtual amplitudes, events can be generated without these amplitudes first. An additional weight, which includes all parts of the NLO calculation, is added at the end of the event generation to the event file. More specifically, for every momentum configuration the virtual contribution is calculated by the POWHEG-BOX-V2. Afterwards, the event without the virtual contribution is reweighted such that the cross section of the particular event matches the one with the full NLO amplitudes. To add the virtual amplitudes automatically after event generation, the following flags are used:

```
for_reweighting 1      ! add virtuals by reweighting
rwl_file 'wgts.xml'   ! reweighting information
```

In this case, the file `wgts.xml` consists of the definition of the first weight only:

```
<initrwgt>
<weight id='1'> Nominal weight </weight>
</initrwgt>
```

A manual reweighting of the event files is done by uncommenting the flags

```
rwl_add 1              ! add new weights to the events
rwl_file 'rwgt.xml'   ! reweighting information
```

and by defining the new parameter set in the xml-file `rwgt.xml`. For instance, if the event files should be reweighted to include different renormalization and factorization scales, one would use:

```
<initrwgt>
<weightgroup name='FAC' combine='envelope'>
<weight id='3'>renscfact=0.5 facscfact=0.5</weight>
<weight id='4'>renscfact=0.5 facscfact=1</weight>
<weight id='5'>renscfact=0.5 facscfact=2</weight>
<weight id='6'>renscfact=1 facscfact=0.5</weight>
<weight id='7'>renscfact=1 facscfact=1</weight>
<weight id='8'>renscfact=1 facscfact=2</weight>
<weight id='9'>renscfact=2 facscfact=0.5</weight>
<weight id='10'>renscfact=2 facscfact=1</weight>
<weight id='11'>renscfact=2 facscfact=2</weight>
</weightgroup>
```

## Appendix B

`</initrwgt >`

With this parameter set nine new weights are added to the event file. In this case the renormalization and factorization scales are varied from  $0.5\mu_{\text{ref}}$  to  $2\mu_{\text{ref}}$ , respectively. More information about the reweighting method of the POWHEG-BOX can be found in Ref. [135].



## C The `runparallel.sh` script

The `runparallel.sh` script simplifies the set up of arbitrary processes of the POWHEG-BOX-V2 by generating and modifying all necessary files. In the following, we want to shed light on how to use this script. The files used here, particularly the template files, can be found in the publicly available repository of the POWHEG-BOX-V2, in the subdirectories of `weakino-pair` and `weakino-pair plus jet production`.

In order to generate all necessary files, a template directory with the default name `testrun_clean` has to be present in the execution path. The template directory must contain the parameter file `powheg_clean.input`, the seed information file `pwgseeds.dat` and the SLHA file containing the particle masses, widths, mixing matrices and coupling parameters.

In general, a calculation is initialized by the command

```
$ ./runparallel.sh -e <executable> -d <run directory>
```

where the flag `-e` indicates the name of the executable and `-d` the name of the directory where all the parameter files can be found and where the results of the run should be stored. This command uses the default parameters present in `powheg_clean.input` and submits four jobs (default) in parallel on a standard desktop computer. More information about additional flags and their function can always be accessed by the commands

```
$ ./runparallel.sh -h or $ ./runparallel.sh --help.
```

### LO cross section and distributions on a desktop computer

The following command generates (parameter `-g`) a run directory `testrun1` from the default template `testrun_clean` and submits four parallel jobs on a desktop computer (parameter `-p`). The parameter `-c` initializes a clearance of the run directory, meaning that all possible grid files and old results present in `testrun1` are deleted<sup>7</sup>. In this example, results are generated for the process  $pp \rightarrow \tilde{\chi}_1^0 \tilde{\chi}_1^0 j$ . The physical parameters are read in from the SLHA parameter file `input_p10MSSMd.slha` (indicated by `--slha`) and the NNPDF23\_nlo\_as\_0119 PDFs with ID=230000 are used. Note that the parameter `lopdf` determines the LO accuracy of the calculation, al-

<sup>7</sup>The parameter `-c` should thus be used with special care.

## Appendix C

though NLO PDFs can be defined here. Only the first two stages are submitted and no events are generated. The number of integration points of the first and second stages are controlled by the parameters `ncall1` and `ncall2`. The final states for which results are to be computed are given by the parameters `--fin1` and `--fin2`.

Note, that if a parameter is present on the command line, the script overwrites the specific parameters in `powheg_clean.input`. Otherwise, if a parameter is not passed to the script, the default parameters of `powheg_clean.input` are used. Since the execution of LO calculation is usually very fast, this command can be used for debugging and fast checks. Furthermore, the script waits for every job of each stage to finish before submitting the jobs of the next stage.

```
$ ./runparallel.sh -g -c -e pwhg_main_ninj+jet \  
-d testrun1 -p 4 --fin1 1000022 --fin2 1000022 \  
--slha input_p10MSSMd.slha --ncall1 20000 \  
--ncall2 30000 --lopdf 230000
```

### NLO cross section on a desktop computer

The next command initializes a NLO computation. The script uses the template directory `testrun_template` (parameter `-t`) to generate the run directory `testrun1` and submits four jobs in parallel. The additional parameters `--ncall1osres` and `--ncall2osres` that define the number of integration points of the real on-shell contributions are necessary at NLO for weakino-pair and weakino-pair plus jet production. The upper bound number (parameter `--nubound`) is set to 1000 and 1000 events (parameter `--nevents`) are generated in the fourth stage. The execution time of each job is written out to the log file by using the flag `--time`.

```
$ ./runparallel.sh -g -c -e pwhg_main_ninj+jet \  
-t testrun_template -d testrun1 -p 4 --ncall1 20000 \  
--ncall2 3000 --ncall1osres 20000 --ncall2osres 3000 \  
--nubound 1000 --nevents 1000 --time
```

## NLO cross section on a high performance computer

On a high performance computer (HPC) with the MOAB queuing system the wall-time of each job must be defined. The walltimes in seconds are controlled by the parameter `-w<n>`, where `n` is the number of the respective stage. The flag `--usemsub` tells the script that the MOAB queuing system should be used. Alternatively, the QSUB queuing system can be accessed by `--usecondor`. This system works similar to MOAB, however, no walltimes have to be defined

To choose different seeds for each run, the parameter `--offset` can be used. With `--offset` equals to 100 and with a total number of 50 jobs, the seeds within the range [101, 150] are used.

```
$ ./runparallel.sh -g -c -e pwhg_main_ninj+jet \  
-d testrun1 -p 50 --fin1 1000022 --fin2 1000022 \  
--slha input_p10MSSMd.slha --ncall1 200000 \  
--ncall2 3000 --ncall1osres 200000 \  
--ncall2osres 3000 --offset 100 --usemsub \  
--w1 43200 --w2 259200
```

## A typical setup for neutralino-pair production with a jet

In the following, the job submitting procedure on an HPC for a typical event generation for weakino-pair plus jet production is given. The approximate execution time given in the following sections was determined on a system with Intel Xeon processors with 25 MB Cache and a processor base frequency of 2.20 GHz. Instead of submitting the jobs of all stages at once, the `runparallel.sh` script can be used to submit jobs only for one single stage as well. This behavior is determined by the `--st<n>` parameters, where `n` is the number of the stage that has to be executed.

### Stage 1, grid generation with three iterations on a QSUB system

This stage is carried out at least three times for 500 different seeds in order to get well converging grids. This behavior is controlled by the flag `--maxgridit <n>`, where `n` is the number of grid iterations. All the grid files of the third iteration are collected after completion. The grid files generated by this run have to be calculated only once for a given PDF and parameter set. They can be recycled for the subsequent NLO runs with different seeds. Since the topology of born and virtual processes

## Appendix C

are the same, the virtual amplitudes, which would unnecessarily prolong execution time, are not needed for the grid generation. Therefore, the `runparallel.sh` script automatically sets the flag `--fakevirt` to true for the first stage to accelerate the computation. Total execution time of this stage amounts to about 20 hours.

```
$ ./runparallel.sh -g -c -e pwhg_main_ninj+jet \  
  -d runGRD001_100 -p 100 --ncall1 200000 \  
  --ncall1osres 200000 --usecondor \  
  --st1 --offset 0 --maxgridit 3
```

### Stage 2, computation of the NLO cross section on a moab system

The grid files `*xg3*` from stage 1 with seeds 1 – 500 along with the template files from the directory `testrun_clean` are transferred manually into a new directory `runEVN001_500`. Afterwards, a total of 500 jobs with a comparatively small number of integration points are submitted. By default, the flag `--fakevirt` is set to false automatically in this stage. Execution time of this stage mounts up to about 12 hours.

```
$ ./runparallel.sh -e pwhg_main_ninj+jet -d runEVN001_500 \  
  -p 500 --ncall2 2000 --ncall2osres 50000 --usemsub \  
  --w2 345600 --offset 0 --st2
```

### Stage 3, set up of the upper bounding envelope

To set up the upper bounding envelope of the integrand, the following command is used. The number of upper bound calls is set to 1000. The execution time of several minutes is very small, however, to be on the safe side a sufficient high walltime is chosen.

```
$ ./runparallel.sh -e pwhg_main_ninj+jet -d runEVN001_500 \  
  -p 500 --ncall1 200000 --ncall2 2000 --nubound 1000 \  
  --usemsub --w3 18000 --offset 0 --st3
```

### Stage 4, event generation

With the next command and if the flag `for_reweighting` (implemented in POWHEG-BOX-RES and in weakinos+jet, Rev. 3361) is set, 1000 events without the computation of time consuming virtual amplitudes are generated. In this stage, the virtual amplitudes are added back by the POWHEG-BOX-V2 via the reweighting method.

This feature does not need any user interaction and is done automatically. The only requirement are the additional flags introduced earlier in App. B that have to be present in the file `powheg.input`.

The total execution time of this stage amounts to about 40 hours.

```
$ ./runparallel.sh -e pwhg_main_ninj+jet -d runEVN001_500 \  
-p 500 --nubound 1000 --nevents 1000 --usemsub \  
--w4 345600 --offset 0 --st4
```

### **Stage 1-4, automatic mode on a MOAB system**

To simplify the execution of the above commands, the commands can be clustered into a single command:

```
$ ./runparallel.sh -g -c -e pwhg_main_ninj+jet \  
-d runEVN001_500 -p 500 --ncall1 200000 \  
--ncall1osres 200000 --maxgridit 3 --ncall2 2000 \  
--ncall2osres 50000 --nubound 1000 --nevents 1000 \  
--usemsub --w1 43200 --w2 345600 --w3 18000 \  
--w4 345600 --offset 0
```



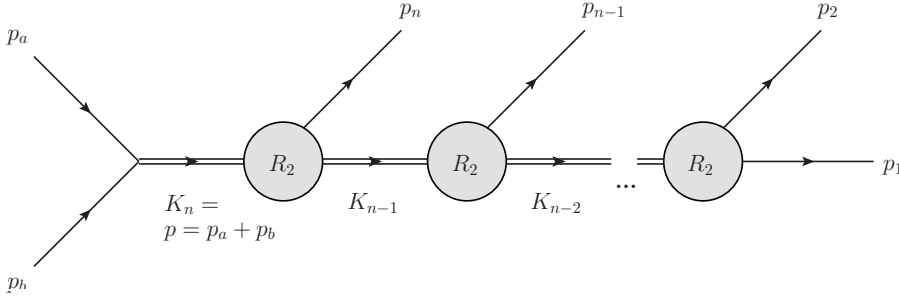


Figure D.1: The definition of a general phase space parametrization with arbitrary multiplicity.

## D Fortran routines for the parametrization of phase spaces

The subroutines we are referring to in this section can be found in `weakinos/phsp_routines.f` and `weakinos-jet/phsp_routines.f`, respectively. A simpler version of this code was earlier implemented in `phi1_2.f` of the POWHEG-BOX project POWHEG-BOX/Wp\_Wp\_J\_J. However, in order to comply with the requirements of weakino-pair and weakino-pair plus jet production, the code was heavily modified and extended in multiple parts. The code is now capable of generating arbitrary phase space parametrizations of multiplicity  $n$  and different splitting layouts. Multiple checks to circumvent bad numerical behavior, debugging information and many more options were implemented. The routines are now as general as possible and can be used for various other projects.

The following discussion aims at giving an overview of how to use these routines.

Recalling the formula of the  $n$ -particle phase space introduced in Sec. 2.2.1, we have

$$R_n(M_n^2) = \int_{\mu_{n-1}^2}^{(M_n - m_n)^2} dM_{n-1}^2 R_2(K_n; K_{n-1}^2, p_n^2) R_{n-1}(M_{n-1}^2), \quad (\text{D.1})$$

where the two-body phase space is defined as

$$R_2(K_n; K_{n-1}^2, p_n^2) = \frac{\lambda^{\frac{1}{2}}(K_n^2, K_{n-1}^2, p_n^2)}{8K_n^2} \int d\Omega_n. \quad (\text{D.2})$$

## Appendix D

A two-particle phase space with fixed masses and momenta of the final-state particles is generated by the call to the subroutine

```
R2phsp(xth, xphi, m1, m2, p0, p1, p2, jac).
```

For given random numbers  $xth, xphi \in [0, 1]$ , masses  $m1$  and  $m2$  of the final-state particles and incoming four-momentum  $p0$ , the final-state momenta  $p1$  and  $p2$  with Jacobian  $jac$  is generated. The random numbers  $xth$  and  $xphi$  are associated to the integration over the solid angle  $d\Omega = \sin\theta d\theta d\phi$ . Note that providing the mass of the incoming particle  $m0$  is not needed since it can be calculated from the incoming momentum  $p0$ . Thus, the two-particle phase spaces presented here can be used for particles of arbitrary masses and are as general as possible.

If a propagator occurs and the invariant mass squared of the particle has to be integrated over, the subroutine

```
R2phsp_s2(psgen, x2, xth, xphi, s2min, m1,
&          bwmass, bwwidth, p0, p1, p2, jac)
```

has to be used. For instance, this is necessary if two subsequent phase spaces are connected to one another. This subroutine uses three random numbers  $x2, xth$  and  $xphi$ , a lower limit for the  $s2$  integration  $s2min$ , an optional Breit-Wigner mass  $bwmass$  and width  $bwidth$  of the intermediate particle (here taken as  $p2$ ), and the incoming four-momentum  $p0$ . The upper limit of the  $s2$  integration is given by  $(\sqrt{p0^2} - m1)^2$  and it is calculated automatically by this subroutine from  $p0$  and the mass of the first final-state particle  $m1$ .

The subroutine

```
R2phsp_s1s2(psgen, x1, x2, xth, xphi, s1min, s1max,
&           s2min, bwmass1, bwwidth1, bwmass2, bwwidth2, p0,
&           p1, p2, jac)
```

is tailored to calculate the two-particle phase space with free invariant masses squared  $s1$  and  $s2$ . This subroutines demands the additional lower  $s1min$  and upper integration limit  $s1max$  for the  $s1$  integration.

In either case, the parameter  $psgen$  determines the random sampling which is used by the Monte-Carlo integrator:

- $psgen=0$ : flat in the integration variable  $s1$  or  $s2$  ( $bwmass$  and  $bwidth$  are not required),
- $psgen=1$ : Breit-Wigner sampling for  $s2$  or  $s1$  and  $s2$ ,



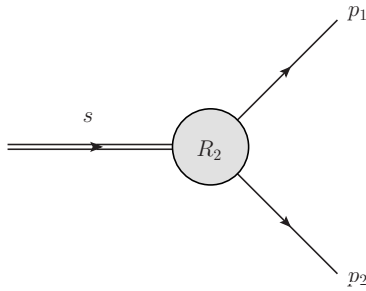


Figure D.2: The kinematics of a two-particle phase space.

- `psgen=2`: Breit-Wigner sampling for `s2` or `s1` and `s2` and flat below the resonance.

The random sampling should be chosen such that the integrals converge best for the process under consideration. At the end of every phase space generation a total Jacobian factor of  $(2\pi)^{-3n+4}$ , where  $n$  is the number of final-state particles, has to be provided manually by the user.

A two-particle phase space, as depicted in Fig. D.2, can be obtained by calling `R2phsp` followed by a global Jacobian factor. Since the integrand is symmetric under rotation about the  $z$ -axis, the random number `xphi` is not needed and can always be put to zero. The momenta `pab` is the sum of the incoming momenta of the incoming partons and can be chosen equal to  $(\text{dsqrt}(s), 0, 0, 0)$ , where  $s$  is the partonic center of mass energy squared. The code snippet for a two-particle phase space is as follows:

```
call R2phsp(xth,OD0,m1,m2,pab,p1,p2,jac)
jacobian = jacobian*jac

jacobian = jacobian/(2D0*pi)**2.
```

A three-particle phase space (see Fig. D.3) can be decomposed into two two-particle phase spaces. The first two-particle phase space is generated with a free parameter `s12` which is integrated over. The lower limit of the `s12` integration should be set manually by the user to `s12min = (m1+m2)**2`. The second two-particle phase space does not require an integration over an additional free parameter. Thus, a three-particle phase space with flat sampling in the `s12` integration is obtained by:

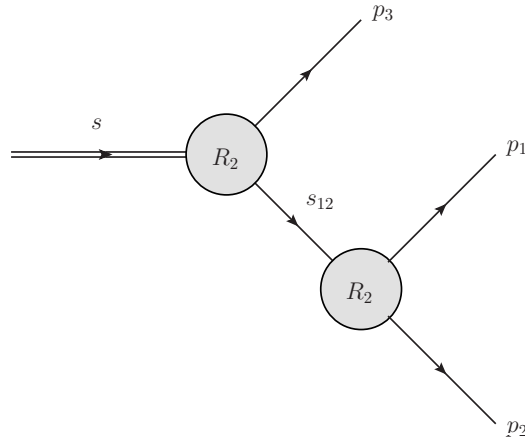


Figure D.3: A possible decomposition of a three-particle phase space.

```

call R2phsp_s2(0,x1,xth1,0D0,s12min,m3,0D0,0D0,
&      pab,p3,p12,jac)
jacobian = jacobian*jac
call R2phsp(xth2,xphi2,m1,m2,p12,p1,p2,jac)
jacobian = jacobian*jac

jacobian = jacobian/(2D0*pi)**5.

```

If a resonance is present on the intermediate line (for example an intermediate squark with mass `msq` and decay width `wsq`) the first call to the subroutine `R2phsp_s2` has to be replaced by

```

call R2phsp_s2(1,x1,xth1,0D0,s12min,m3,msq,wsq,
&      pab,p3,p12,jac).

```

With the subroutines defined in `phsp_routines.f`, four-particle phase spaces can be generated in two possible ways. The first possibility, depicted in Fig. D.4, is especially suitable for on-shell singly resonant diagrams that can appear in the real corrections of weakino-pair production processes plus jet. The intermediate particles with masses `m234` and `m34`, and decay widths `w234` and `w34` are considered. Two two-particle phase spaces with open parameters `s234` and `s34` are connected to one another. Similar to the three-particle phase space, the lower integration limits should be set manually by the user to `s234min = (m2+m3+m4)**2` and `s34min = (m3+m4)**2`. At the end, a two-particle phase space generates the momenta of the

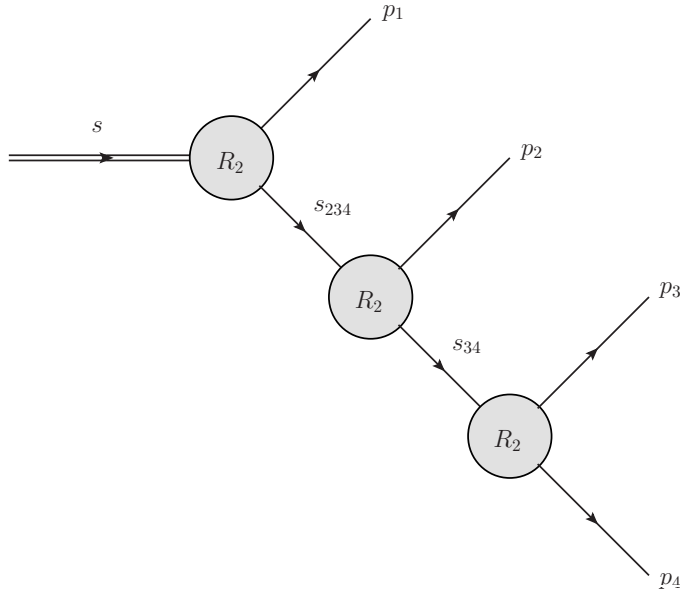


Figure D.4: The first possible decomposition of a four-particle phase space.

final-state particles  $p_3$  and  $p_4$ . The following code snippet illustrates the generation of a four-particle phase space:

```

call R2phsp_s2(1,x1,xth1,0D0,s234min,m1,m234,w234,
&
           pab,p1,p234,jac)
jacobian = jacobian*jac

call R2phsp_s2(1,x2,xth2,xphi2,s34min,m2,m34,w34,
&
           p234,p2,p34,jac)
jacobian = jacobian*jac

call R2phsp(xth3,xphi3,m3,m4,p34,p3,p4,jac)
jacobian = jacobian*jac

jacobian = jacobian/(2D0*pi)**8.

```

The second possible decomposition of a four-particle phase space is especially suitable for on-shell doubly resonant diagrams that can occur in the real corrections of weakino-pair production processes plus jet. Here, the two intermediate lines, which are integrated over the variables  $s_{12}$  and  $s_{34}$ , are tailored to the squark masses

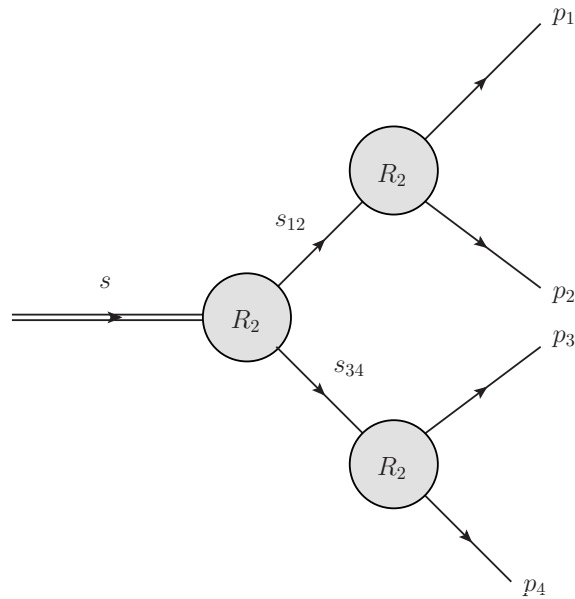


Figure D.5: The second possible decomposition of a four-particle phase space.

$m_{12}$  and  $m_{34}$ , and the widths  $w_{12}$  and  $w_{34}$  that can occur in those diagrams. Hence, this decomposition is perfect for the evaluation of doubly resonant diagrams with a Monte Carlo integrator. Again, the lower integration limits should be set manually by the user to  $s_{12min} = (m_1+m_2)**2$  and  $s_{34min} = (m_3+m_4)**2$ , respectively.

```

call R2phsp_s1s2(2,x1,x2,xth1,0D0,s12min,s12max,
&               s34min,m12,w12,m34,w34,pab,p12,p34,jac)
jacobian = jacobian*jac

call R2phsp(xth2,xphi2,m1,m2,p12,p1,p2,jac)
jacobian = jacobian*jac

call R2phsp(xth3,xphi3,m3,m4,p34,p3,p4,jac)
jacobian = jacobian*jac

jacobian = jacobian/(2D0*pi)**8.

```

## **E Selecting doubly on-shell resonant diagrams with FeynArts**

In collaboration with Thomas Hahn<sup>8</sup>, we have developed a MATHEMATICA extension to FEYNARTS which helps to select diagrams based on where a certain particle occurs in the topology of a Feynman diagram. The extensions we have developed can be found on [https://github.com/MKesenheimer/weakinos-jet/tree/master/Scripts/Modified\\_Files](https://github.com/MKesenheimer/weakinos-jet/tree/master/Scripts/Modified_Files). In the following we want to go through the details of using some of the functions by means of a small MATHEMATICA script.

The script starts by initializing FEYNARTS, FORMCALC and the respective FEYNARTSADD and FORMCALCADD extensions. We will focus here on the usage of FEYNARTSADD, however, many more useful functions are defined in the FORMCALCADD extension. For instance, a function to compute spin-correlated amplitudes has been implemented<sup>9</sup>.

```
Clear ["Global ' *"]
SetDirectory [NotebookDirectory []];
<< FeynArts '
<< FeynArtsAdd '
<< FormCalc '
<< FormCalcAdd '
ClearProcess []
```

---

<sup>8</sup><http://wwwth.mpp.mpg.de/members/hahn/>

<sup>9</sup>A script to calculate the spin-correlated amplitudes by the FORMCALCADD extension including a small test program to numerically evaluate the amplitudes of the process  $\bar{u}u \rightarrow \gamma g$  can be found on [https://github.com/MKesenheimer/Test\\_FormCalc\\_Amps](https://github.com/MKesenheimer/Test_FormCalc_Amps). Note, that this project is still work in progress and may not yield correct results.

## Appendix E

The next step is to set up the process. We neglect all particles and couplings that are not necessary for this discussion. As an example, we shall consider the process  $d\bar{d} \rightarrow \tilde{\chi}_1 \tilde{\chi}_2 d\bar{d}$  in the MSSM.

```
SetOptions[InsertFields, Model -> "MSSMCT",
  Restrictions -> {NoLightFHCoupling},
  ExcludeParticles -> {S[1 | 2 | 3 | 4 | 5 |
                      6 | 11 | 12], F[1 | 2]},
  LastSelections -> {! F[11], ! F[12]}}];

process = {F[4, {1}], -F[4, {1}]} -> {F[11, {1}],
  F[11, {2}], F[4, {1}], -F[4, {1}]}];
```

The following commands create the topologies and sort out unnecessary insertions. We only consider diagrams that contain squarks, thus, diagrams without squarks are deleted. After the `Paint` command, the diagrams of Fig. E.1 are generated.

```
tops = CreateTopologies[0, 2 -> 4];
ins = InsertFields[tops, process,
  InsertionLevel -> {Particles}];
insOS = DiagramSelect[
  ins, (FieldPointMemberQ[FieldPoints[##],
  FieldPoint[_][S[_], {_, _, _}], _, _] ||
  FieldPointMemberQ[FieldPoints[##],
  FieldPoint[_][_, _, S[_], {_, _, _}]] ||
  FieldPointMemberQ[FieldPoints[##],
  FieldPoint[_][_, S[_], {_, _, _}], _]) &];

Paint[insOS, PaintLevel -> {Particles}];
```

$$d \quad d \quad \rightarrow \quad \tilde{\chi}_1^0 \quad \tilde{\chi}_2^0 \quad d \quad d$$

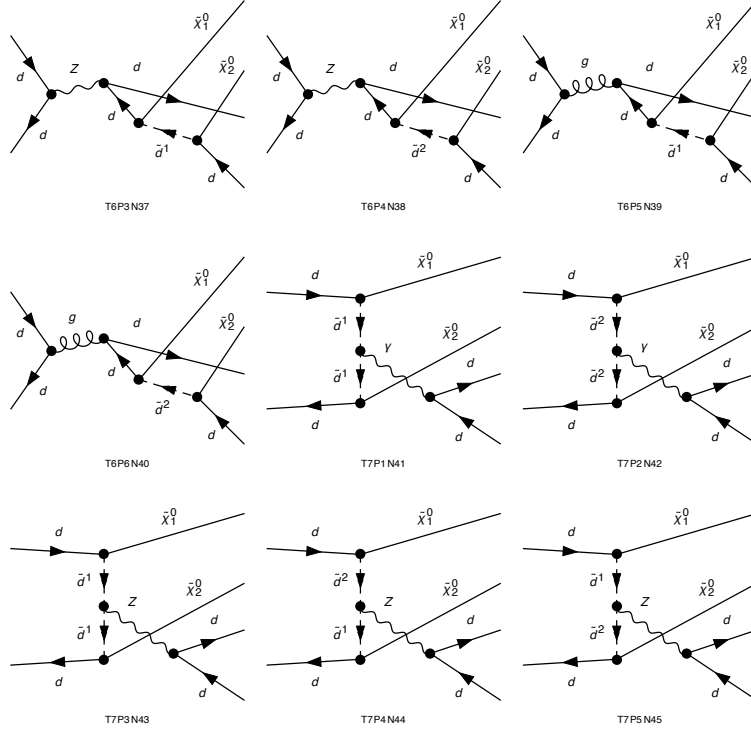


Figure E.1: A subset of the diagrams for the process  $d\bar{d} \rightarrow \tilde{\chi}_1^0 \tilde{\chi}_2^0 d\bar{d}$ . Still included are diagrams with single on-shell squark resonances and diagrams without any squark resonances.

We now look for squarks that occur on s-channel lines. If a diagram contains a t-channel squark, we delete it. After these commands, the diagrams depicted in Fig. E.2 remain.

```
insOSall = DiagramSelect[insOS, SChannelQ[S[_]]];
insOSall = DiagramSelect[insOSall,
    (Not[TChannelQ[S[_]][##_]) &];
Paint[insOSall, PaintLevel -> {Particles}];
```

## Appendix E

$$d \quad d \quad \rightarrow \quad \tilde{\chi}_1^0 \quad \tilde{\chi}_2^0 \quad d \quad d$$

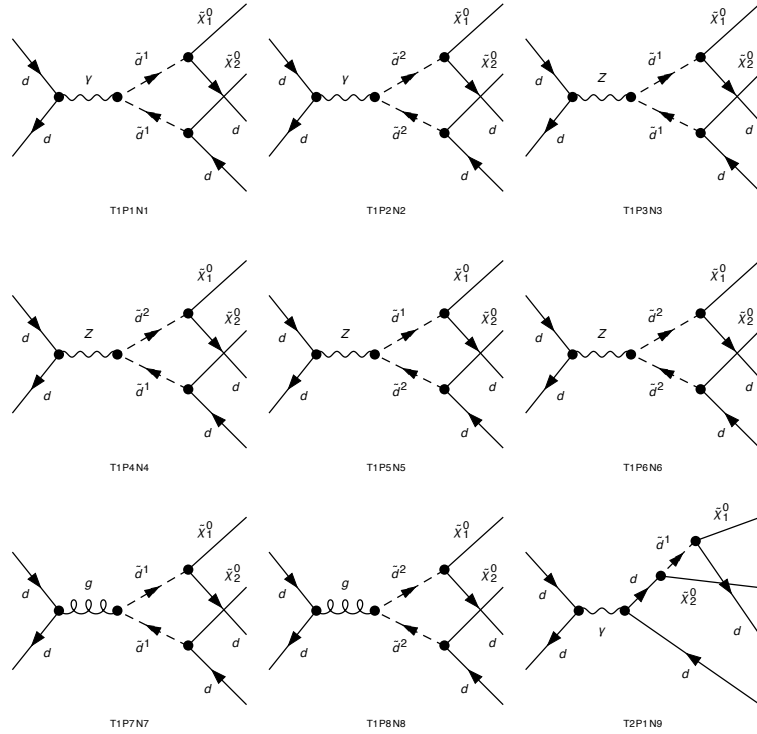


Figure E.2: A subset of diagrams with squark on-shell resonances. Parts of these diagrams are still singly on-shell resonant and thus have to be deleted.

For the final step, we look for s-channel squarks that couple only to the legs  $(3, 5) = (\tilde{\chi}_1, d)$  and  $(4, 6) = (\tilde{\chi}_2, \bar{d})$ , respectively. The final diagrams are shown in Fig. E.3.

```

insOSl35 = DiagramSelect[insOS,
    SChannelExtQ[S[_ , {1, _ , _}], 3, 5]];
insOSl35l46 = DiagramSelect[insOSl35,
    SChannelExtQ[S[_ , {1, _ , _}], 4, 6]];
Paint[insOSl35l46, PaintLevel -> {Particles}];

```



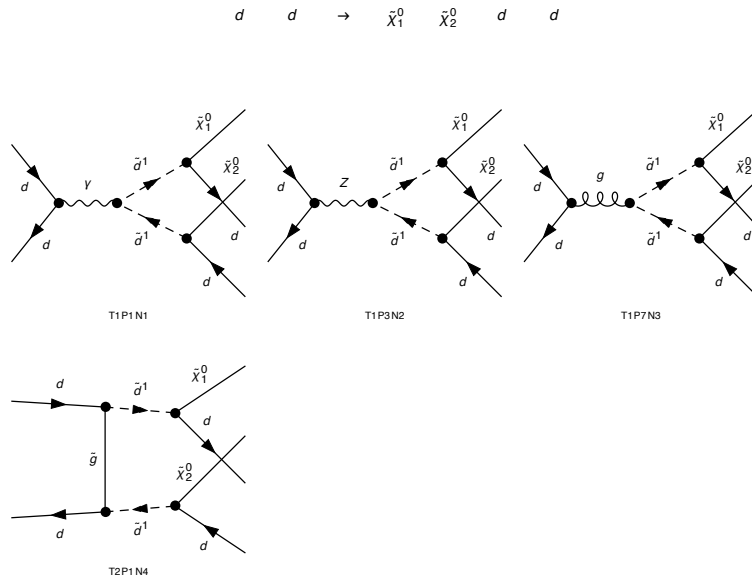


Figure E.3: Diagrams with doubly on-shell resonant squarks for the process  $d\bar{d} \rightarrow \tilde{\chi}_1^0 \tilde{\chi}_2^0 d\bar{d}$ . After the application of the newly implemented functions to sort out non-resonant diagrams, only diagrams with doubly on-shell resonant squarks that couple to the external legs (3, 5) and (4, 6) are left.



# Bibliography

- [1] T. Gutsche, M. Kesenheimer and V. E. Lyubovitskij, *Radiative and dilepton decays of the hadronic molecule  $Z_c^+(3900)$* , *Phys. Rev.* **D90** (2014) 094013, [1410.0259].
- [2] S. L. Glashow, *The renormalizability of vector meson interactions*, *Nuclear Physics* **10** (1959) 107 – 117.
- [3] A. Salam and J. C. Ward, *Weak and electromagnetic interactions*, *Il Nuovo Cimento (1955-1965)* **11** (Feb, 1959) 568–577.
- [4] S. Weinberg, *A model of leptons*, *Phys. Rev. Lett.* **19** (Nov, 1967) 1264–1266.
- [5] C.-N. Yang and R. L. Mills, *Conservation of Isotopic Spin and Isotopic Gauge Invariance*, *Phys. Rev.* **96** (1954) 191–195.
- [6] H. Fritzsch, M. Gell-Mann and H. Leutwyler, *Advantages of the Color Octet Gluon Picture*, *Phys. Lett.* **47B** (1973) 365–368.
- [7] Deutsches Elektronen-Synchrotron DESY, *Das Higgs*.  
[www.weltmaschine.de/physik/higgs/hintergrundinformationen](http://www.weltmaschine.de/physik/higgs/hintergrundinformationen),  
January, 2018.
- [8] P. W. Higgs, *Broken symmetries and the masses of gauge bosons*, *Phys. Rev. Lett.* **13** (Oct, 1964) 508–509.
- [9] F. Englert and R. Brout, *Broken symmetry and the mass of gauge vector mesons*, *Phys. Rev. Lett.* **13** (Aug, 1964) 321–323.
- [10] G. S. Guralnik, C. R. Hagen and T. W. B. Kibble, *Global conservation laws and massless particles*, *Phys. Rev. Lett.* **13** (Nov, 1964) 585–587.
- [11] C. L. Smith, *High energy behaviour and gauge symmetry*, *Physics Letters B* **46** (1973) 233 – 236.

## Bibliography

- [12] J. M. Cornwall, D. N. Levin and G. Tiktopoulos, *Uniqueness of spontaneously broken gauge theories*, *Phys. Rev. Lett.* **30** (Jun, 1973) 1268–1270.
- [13] Y. Nambu, *Quasi-particles and gauge invariance in the theory of superconductivity*, *Phys. Rev.* **117** (Feb, 1960) 648–663.
- [14] J. Goldstone, *Field theories with  $\hat{A}$  « superconductor  $\hat{A}$  » solutions*, *Il Nuovo Cimento (1955-1965)* **19** (Jan, 1961) 154–164.
- [15] J. Goldstone, A. Salam and S. Weinberg, *Broken symmetries*, *Phys. Rev.* **127** (Aug, 1962) 965–970.
- [16] C. E. Vayonakis, *Born helicity amplitudes and cross-sections in non-abelian gauge theories*, *Lettere al Nuovo Cimento (1971-1985)* **17** (Nov, 1976) 383–387.
- [17] ATLAS collaboration, G. Aad et al., *Observation of a new particle in the search for the Standard Model Higgs boson with the ATLAS detector at the LHC*, *Phys. Lett.* **B716** (2012) 1–29, [1207.7214].
- [18] CMS collaboration, S. Chatrchyan et al., *Observation of a new boson at a mass of 125 GeV with the CMS experiment at the LHC*, *Phys. Lett.* **B716** (2012) 30–61, [1207.7235].
- [19] G. e. a. Aad, *Measurements of the higgs boson production and decay rates and coupling strengths using pp collision data at  $\sqrt{s} = 7$  and 8tev in the atlas experiment*, *The European Physical Journal C* **76** (Jan, 2016) 6.
- [20] SUPER-KAMIOKANDE COLLABORATION collaboration, Y. Fukuda, T. Hayakawa, E. Ichihara, K. Inoue, K. Ishihara, H. Ishino et al., *Evidence for oscillation of atmospheric neutrinos*, *Phys. Rev. Lett.* **81** (Aug, 1998) 1562–1567.
- [21] THE SUPER-KAMIOKANDE COLLABORATION collaboration, R. Wendell, C. Ishihara, K. Abe, Y. Hayato, T. Iida, M. Ikeda et al., *Atmospheric neutrino oscillation analysis with subleading effects in super-kamiokande i, ii, and iii*, *Phys. Rev. D* **81** (May, 2010) 092004.
- [22] SNO COLLABORATION collaboration, Q. R. Ahmad, R. C. Allen, T. C. Andersen, J. D. Anglin, J. C. Barton, E. W. Beier et al., *Direct evidence for neutrino flavor transformation from neutral-current interactions in the sudbury neutrino observatory*, *Phys. Rev. Lett.* **89** (Jun, 2002) 011301.

- [23] KAMLAND COLLABORATION collaboration, K. Eguchi, S. Enomoto, K. Furuno, J. Goldman, H. Hanada, H. Ikeda et al., *First results from kamland: Evidence for reactor antineutrino disappearance*, *Phys. Rev. Lett.* **90** (Jan, 2003) 021802.
- [24] D. Clowe, A. Gonzalez and M. Markevitch, *Weak lensing mass reconstruction of the interacting cluster 1E0657-558: Direct evidence for the existence of dark matter*, *Astrophys. J.* **604** (2004) 596–603, [astro-ph/0312273].
- [25] M. Markevitch, A. H. Gonzalez, D. Clowe, A. Vikhlinin, L. David, W. Forman et al., *Direct constraints on the dark matter self-interaction cross-section from the merging galaxy cluster 1E0657-56*, *Astrophys. J.* **606** (2004) 819–824, [astro-ph/0309303].
- [26] G. Bertone and D. Hooper, *A History of Dark Matter*, Submitted to: *Rev. Mod. Phys.* (2016) , [1605.04909].
- [27] I. J. R. Aitchison, *Supersymmetry and the MSSM: An Elementary introduction*, hep-ph/0505105.
- [28] J. D. Wells, *Higgs naturalness and the scalar boson proliferation instability problem*, *Synthese* **194** (2017) 477–490, [1603.06131].
- [29] A. Belyaev, M. S. Brown, R. Foadi and M. T. Frandsen, *The Technicolor Higgs in the Light of LHC Data*, *Phys. Rev.* **D90** (2014) 035012, [1309.2097].
- [30] I. D’Souza and C. Kalman, *Preons*. World Scientific, Singapore, 1992.
- [31] K. Sugita, Y. Okamoto and M. Sekine, *Composite model of higgs bosons, II* *Nuovo Cimento A (1971-1996)* **106** (Feb, 1993) 271–273.
- [32] V. Miransky, M. Tanabashi and K. Yamawaki, *Dynamical electroweak symmetry breaking with large anomalous dimension and  $t$  quark condensate*, *Physics Letters B* **221** (1989) 177 – 183.
- [33] H. Georgi, *Towards a grand unified theory of flavor*, *Nuclear Physics B* **156** (1979) 126 – 134.
- [34] J. Ellis, M. K. Gaillard and B. Zumino, *A grand unified theory obtained from broken supergravity*, *Physics Letters B* **94** (1980) 343 – 348.
- [35] N. Bilic, *Supersymmetric dark energy*, *Rom. J. Phys.* **57** (2012) 793–802, [1004.4984].

## Bibliography

- [36] C. Froggatt, R. Nevzorov and H. B. Nielsen, *On the smallness of the cosmological constant in SUGRA models*, *Nucl. Phys.* **B743** (2006) 133–152, [[hep-ph/0511259](#)].
- [37] C. Froggatt, R. Nevzorov and H. B. Nielsen, *Dark Energy density in Split SUSY models inspired by degenerate vacua*, *PoS ICHEP2010* (2010) 442, [[1012.5121](#)].
- [38] P. van Nieuwenhuizen, *Supergravity*, *Physics Reports* **68** (1981) 189 – 398.
- [39] S. Coleman and J. Mandula, *All possible symmetries of the s matrix*, *Phys. Rev.* **159** (Jul, 1967) 1251–1256.
- [40] R. Haag, J. T. Łopuszański and M. Sohnius, *All possible generators of supersymmetries of the s-matrix*, *Nuclear Physics B* **88** (1975) 257 – 274.
- [41] S. L. Adler and W. A. Bardeen, *Absence of higher-order corrections in the anomalous axial-vector divergence equation*, *Phys. Rev.* **182** (Jun, 1969) 1517–1536.
- [42] L. Alvarez-Gaume and E. Witten, *Gravitational Anomalies*, *Nucl. Phys.* **B234** (1984) 269.
- [43] P. Fayet, *Mixing Between Gravitational and Weak Interactions Through the Massive Gravitino*, *Phys. Lett.* **70B** (1977) 461.
- [44] S. P. Martin, *A Supersymmetry primer*, [hep-ph/9709356](#).
- [45] K. A. Intriligator and N. Seiberg, *Lectures on Supersymmetry Breaking*, *Class. Quant. Grav.* **24** (2007) S741–S772, [[hep-ph/0702069](#)].
- [46] H. Nilles, *Supersymmetry, supergravity and particle physics*, *Physics Reports* **110** (1984) 1 – 162.
- [47] H. P. Nilles, *Dynamically broken supergravity and the hierarchy problem*, *Physics Letters B* **115** (1982) 193 – 196.
- [48] P. Fayet and J. Iliopoulos, *Spontaneously broken supergauge symmetries and goldstone spinors*, *Physics Letters B* **51** (1974) 461 – 464.
- [49] L. Girardello and M. Grisaru, *Soft breaking of supersymmetry*, *Nuclear Physics B* **194** (1982) 65 – 76.

- [50] Y. Nir, *CP violation in and beyond the standard model*, in *Proceedings, 27th SLAC Summer Institute on Particle Physics: CP Violation in and Beyond the Standard Model (SSI 99): Stanford, USA, July 7-16, 1999*, pp. 165–243, 1999. [hep-ph/9911321](#).
- [51] S. Dimopoulos and D. W. Sutter, *The Supersymmetric flavor problem*, *Nucl. Phys.* **B452** (1995) 496–512, [[hep-ph/9504415](#)].
- [52] S. Kraml, *CP violation in SUSY*, in *SUSY 2007 Proceedings, 15th International Conference on Supersymmetry and Unification of Fundamental Interactions, July 26 - August 1, 2007, Karlsruhe, Germany*, pp. 132–139, 2007. [0710.5117](#).
- [53] R. N. Mohapatra, *Supersymmetry and R-parity: an Overview*, *Phys. Scripta* **90** (2015) 088004, [[1503.06478](#)].
- [54] G. R. Farrar and P. Fayet, *Phenomenology of the production, decay, and detection of new hadronic states associated with supersymmetry*, *Physics Letters B* **76** (1978) 575 – 579.
- [55] H. K. Dreiner, *An Introduction to explicit R-parity violation*, [hep-ph/9707435](#).
- [56] R. Barbier et al., *R-parity violating supersymmetry*, *Phys. Rept.* **420** (2005) 1–202, [[hep-ph/0406039](#)].
- [57] S. Mine and S. K. Collaboration, *Recent nucleon decay results from super kamiokande*, *Journal of Physics: Conference Series* **718** (2016) 062044.
- [58] H. E. Haber, *The Status of the minimal supersymmetric standard model and beyond*, *Nucl. Phys. Proc. Suppl.* **62** (1998) 469–484, [[hep-ph/9709450](#)].
- [59] S. S. AbdusSalam et al., *Benchmark Models, Planes, Lines and Points for Future SUSY Searches at the LHC*, *Eur. Phys. J.* **C71** (2011) 1835, [[1109.3859](#)].
- [60] G. L. Kane, C. F. Kolda, L. Roszkowski and J. D. Wells, *Study of constrained minimal supersymmetry*, *Phys. Rev.* **D49** (1994) 6173–6210, [[hep-ph/9312272](#)].
- [61] H. P. Nilles, *Dynamically Broken Supergravity and the Hierarchy Problem*, *Phys. Lett.* **115B** (1982) 193.

## Bibliography

- [62] H. Nilles, *Supergravity generates hierarchies*, *Nuclear Physics B* **217** (1983) 366 – 380.
- [63] A. H. Chamseddine, R. Arnowitt and P. Nath, *Locally supersymmetric grand unification*, *Phys. Rev. Lett.* **49** (Oct, 1982) 970–974.
- [64] R. Barbieri, S. Ferrara and C. Savoy, *Gauge models with spontaneously broken local supersymmetry*, *Physics Letters B* **119** (1982) 343 – 347.
- [65] A. Dedes, A. B. Lahanas and K. Tamvakis, *Radiative electroweak symmetry breaking in the MSSM and low-energy threshold*, *Phys. Rev.* **D53** (1996) 3793–3807, [[hep-ph/9504239](#)].
- [66] J. R. Ellis, K. A. Olive and Y. Santoso, *The MSSM parameter space with nonuniversal Higgs masses*, *Phys. Lett.* **B539** (2002) 107–118, [[hep-ph/0204192](#)].
- [67] J. R. Ellis, T. Falk, K. A. Olive and Y. Santoso, *Exploration of the MSSM with nonuniversal Higgs masses*, *Nucl. Phys.* **B652** (2003) 259–347, [[hep-ph/0210205](#)].
- [68] K. J. de Vries et al., *The pMSSM10 after LHC Run 1*, *Eur. Phys. J.* **C75** (2015) 422, [[1504.03260](#)].
- [69] ATLAS collaboration, G. Aad et al., *Summary of the searches for squarks and gluinos using  $\sqrt{s} = 8$  TeV pp collisions with the ATLAS experiment at the LHC*, *JHEP* **10** (2015) 054, [[1507.05525](#)].
- [70] B. C. Allanach, *SOFTSUSY: a program for calculating supersymmetric spectra*, *Comput. Phys. Commun.* **143** (2002) 305–331, [[hep-ph/0104145](#)].
- [71] ATLAS collaboration, G. Aad et al., *Search for new phenomena in final states with large jet multiplicities and missing transverse momentum with ATLAS using  $\sqrt{s} = 13$  TeV proton-proton collisions*, *Phys. Lett.* **B757** (2016) 334–355, [[1602.06194](#)].
- [72] ATLAS collaboration, *twiki CERN*. <https://twiki.cern.ch/twiki/bin/view/AtlasPublic/SupersymmetryPublicResults>, January, 2018.
- [73] CMS collaboration, *twiki CERN*. <https://twiki.cern.ch/twiki/bin/view/CMSPublic/PhysicsResultsSUS>, January, 2018.



- [74] CMS collaboration, V. Khachatryan et al., *Measurement of the inclusive 3-jet production differential cross section in proton–proton collisions at 7 TeV and determination of the strong coupling constant in the TeV range*, *Eur. Phys. J.* **C75** (2015) 186, [1412.1633].
- [75] G. M. Prosperini, M. Raciti and C. Simolo, *On the running coupling constant in QCD*, *Prog. Part. Nucl. Phys.* **58** (2007) 387–438, [hep-ph/0607209].
- [76] D. J. Gross and F. Wilczek, *Ultraviolet behavior of non-abelian gauge theories*, *Phys. Rev. Lett.* **30** (Jun, 1973) 1343–1346.
- [77] H. D. Politzer, *Reliable perturbative results for strong interactions?*, *Phys. Rev. Lett.* **30** (Jun, 1973) 1346–1349.
- [78] G. Munster and M. Walzl, *Lattice gauge theory: A Short primer*, in *Phenomenology of gauge interactions. Proceedings, Summer School, Zuoz, Switzerland, August 13-19, 2000*, pp. 127–160, 2000. hep-lat/0012005.
- [79] F. Dulat, S. Lionetti, B. Mistlberger, A. Pelloni and C. Specchia, *Higgs-differential cross section at NNLO in dimensional regularisation*, *JHEP* **07** (2017) 017, [1704.08220].
- [80] H. Lehmann, K. Symanzik and W. Zimmermann, *Zur formulierung quantisierter feldtheorien*, *Il Nuovo Cimento (1955-1965)* **1** (Jan, 1955) 205–225.
- [81] R. P. Feynman, *Space-time approach to quantum electrodynamics*, *Phys. Rev.* **76** (Sep, 1949) 769–789.
- [82] J. D. Bjorken, *Asymptotic sum rules at infinite momentum*, *Phys. Rev.* **179** (Mar, 1969) 1547–1553.
- [83] E. Byckling and K. Kajantie, *Particle Kinematics*. Wiley Publ., 319 p., 1971.
- [84] E. Byckling and K. Kajantie, *Particle kinematics*. A Wiley-Interscience publication. Wiley, 1973.
- [85] P. A. M. Dirac, *The Evolution of the Physicist’s Picture of Nature*, *Scientific American* **208** (May, 1963) 45–53.
- [86] H. A. Bethe, *The Electromagnetic shift of energy levels*, *Phys. Rev.* **72** (1947) 339–341.

## Bibliography

- [87] J. C. Collins, *Renormalization: General theory*, hep-th/0602121.
- [88] G. 't Hooft and M. Veltman, *Regularization and renormalization of gauge fields*, *Nuclear Physics B* **44** (July, 1972) 189–213.
- [89] W. Pauli and F. Villars, *On the invariant regularization in relativistic quantum theory*, *Rev. Mod. Phys.* **21** (Jul, 1949) 434–444.
- [90] W. Siegel, *Inconsistency of supersymmetric dimensional regularization*, *Physics Letters B* **94** (1980) 37 – 40.
- [91] G. 't Hooft, *Lattice regularization of gauge theories without loss of chiral symmetry*, *Phys. Lett.* **B349** (1995) 491–498, [hep-th/9411228].
- [92] G. 'tHooft, *Renormalization of massless yang-mills fields*, *Nuclear Physics B* **33** (1971) 173 – 199.
- [93] G. Hooft, *Renormalizable lagrangians for massive yang-mills fields*, *Nuclear Physics B* **35** (1971) 167 – 188.
- [94] G. 't Hooft, *The Glorious days of physics: Renormalization of gauge theories*, hep-th/9812203.
- [95] A. Denner, *Techniques for calculation of electroweak radiative corrections at the one loop level and results for W physics at LEP-200*, *Fortsch. Phys.* **41** (1993) 307–420, [0709.1075].
- [96] W. A. Bardeen, A. J. Buras, D. W. Duke and T. Muta, *Deep-inelastic scattering beyond the leading order in asymptotically free gauge theories*, *Phys. Rev. D* **18** (Dec, 1978) 3998–4017.
- [97] G. 't Hooft, *Dimensional regularization and the renormalization group*, *Nuclear Physics B* **61** (1973) 455 – 468.
- [98] ATLAS collaboration, O. Brandt, *Measurements of the top quark mass with the ATLAS detector*, *PoS EPS-HEP2015* (2015) 324, [1510.00148].
- [99] S. Spannagel, *Top quark mass measurements with the CMS experiment at the LHC*, *PoS DIS2016* (2016) 150, [1607.04972].
- [100] ATLAS, CMS collaboration, T. G. McCarthy, *Top Quark Mass Measurements at the LHC*, in *Proceedings, 51st Rencontres de Moriond on*

- QCD and High Energy Interactions: La Thuile, Italy, March 19-26, 2016*, pp. 13–18, 2016. 1612.04994.
- [101] W. Beenakker, R. Hopker, M. Spira and P. M. Zerwas, *Squark and gluino production at hadron colliders*, *Nucl. Phys.* **B492** (1997) 51–103, [hep-ph/9610490].
- [102] S. P. Martin and M. T. Vaughn, *Regularization dependence of running couplings in softly broken supersymmetry*, *Phys. Lett.* **B318** (1993) 331–337, [hep-ph/9308222].
- [103] W. Hollik and D. Stockinger, *Regularization and supersymmetry restoring counterterms in supersymmetric QCD*, *Eur. Phys. J.* **C20** (2001) 105–119, [hep-ph/0103009].
- [104] S. Alioli, P. Nason, C. Oleari and E. Re, *A general framework for implementing NLO calculations in shower Monte Carlo programs: the POWHEG BOX*, *JHEP* **06** (2010) 043, [1002.2581].
- [105] A. Denner and S. Dittmaier, *The Complex-mass scheme for perturbative calculations with unstable particles*, *Nucl. Phys. Proc. Suppl.* **160** (2006) 22–26, [hep-ph/0605312].
- [106] T. Kinoshita, *Mass Singularities of Feynman Amplitudes*, *Journal of Mathematical Physics* **3** (July, 1962) 650–677.
- [107] T. D. Lee and M. Nauenberg, *Degenerate Systems and Mass Singularities*, *Physical Review* **133** (Mar., 1964) B1549–B1562.
- [108] J. C. Collins, D. E. Soper and G. F. Sterman, *Factorization of Hard Processes in QCD*, *Adv. Ser. Direct. High Energy Phys.* **5** (1989) 1–91, [hep-ph/0409313].
- [109] M. G. Echevarria, A. Idilbi and I. Scimemi, *Factorization Theorem For Drell-Yan At Low  $q_{\perp}$  T And Transverse Momentum Distributions On-The-Light-Cone*, *JHEP* **07** (2012) 002, [1111.4996].
- [110] G.-L. Zhou, *A Proof of Factorization Theorem of Drell–Yan Process at Operator Level*, *Commun. Theor. Phys.* **65** (2016) 193–203, [1307.4194].
- [111] J. C. Collins, *Proof of factorization for diffractive hard scattering*, *Phys. Rev.* **D57** (1998) 3051–3056, [hep-ph/9709499].

## Bibliography

- [112] P.-y. Chen, A. Idilbi and X.-d. Ji, *QCD Factorization for Deep-Inelastic Scattering At Large Bjorken  $x(B) \rightarrow 1 - O(\Lambda(QCD)/Q)$* , *Nucl. Phys.* **B763** (2007) 183–197, [hep-ph/0607003].
- [113] Y. L. Dokshitzer, *Calculation of the Structure Functions for Deep Inelastic Scattering and  $e^+ e^-$  Annihilation by Perturbation Theory in Quantum Chromodynamics.*, *Sov. Phys. JETP* **46** (1977) 641–653.
- [114] V. N. Gribov and L. N. Lipatov, *Deep inelastic  $e p$  scattering in perturbation theory*, *Sov. J. Nucl. Phys.* **15** (1972) 438–450.
- [115] G. Altarelli and G. Parisi, *Asymptotic freedom in parton language*, *Nuclear Physics B* **126** (1977) 298 – 318.
- [116] S. Catani and M. H. Seymour, *A General algorithm for calculating jet cross-sections in NLO QCD*, *Nucl. Phys.* **B485** (1997) 291–419, [hep-ph/9605323].
- [117] P. Z. Skands, *QCD for Collider Physics*, in *Proceedings, High-energy Physics. Proceedings, 18th European School (ESHEP 2010): Raseborg, Finland, June 20 - July 3, 2010*, 2011. 1104.2863.
- [118] R. K. Ellis, W. J. Stirling and B. R. Webber, *QCD and collider physics*, *Camb. Monogr. Part. Phys. Nucl. Phys. Cosmol.* **8** (1996) 1–435.
- [119] G. P. Salam, *Towards Jetography*, *Eur. Phys. J.* **C67** (2010) 637–686, [0906.1833].
- [120] G. P. Salam, *Elements of QCD for hadron colliders*, in *High-energy physics. Proceedings, 17th European School, ESHEP 2009, Bautzen, Germany, June 14-27, 2009*, 2010. 1011.5131.
- [121] M. Cacciari, G. P. Salam and G. Soyez, *The Anti- $k(t)$  jet clustering algorithm*, *JHEP* **04** (2008) 063, [0802.1189].
- [122] Y. L. Dokshitzer, G. D. Leder, S. Moretti and B. R. Webber, *Better jet clustering algorithms*, *JHEP* **08** (1997) 001, [hep-ph/9707323].
- [123] R. Atkin, *Review of jet reconstruction algorithms*, *Journal of Physics: Conference Series* **645** (2015) 012008.
- [124] S. Frixione, Z. Kunszt and A. Signer, *Three jet cross-sections to next-to-leading order*, *Nucl. Phys.* **B467** (1996) 399–442, [hep-ph/9512328].

- [125] S. Frixione, *A General approach to jet cross-sections in QCD*, *Nucl. Phys.* **B507** (1997) 295–314, [[hep-ph/9706545](#)].
- [126] A. Gehrmann-De Ridder, T. Gehrmann and E. W. N. Glover, *Antenna subtraction at NNLO*, *JHEP* **09** (2005) 056, [[hep-ph/0505111](#)].
- [127] A. Daleo, T. Gehrmann and D. Maitre, *Antenna subtraction with hadronic initial states*, *JHEP* **04** (2007) 016, [[hep-ph/0612257](#)].
- [128] B. W. Harris and J. F. Owens, *The Two cutoff phase space slicing method*, *Phys. Rev.* **D65** (2002) 094032, [[hep-ph/0102128](#)].
- [129] Z. Kunszt and D. E. Soper, *Calculation of jet cross sections in hadron collisions at order  $\alpha_s^3$* , *Phys. Rev. D* **46** (Jul, 1992) 192–221.
- [130] P. Nason, *A New method for combining NLO QCD with shower Monte Carlo algorithms*, *JHEP* **11** (2004) 040, [[hep-ph/0409146](#)].
- [131] J. Bellm et al., *Herwig 7.0/Herwig++ 3.0 release note*, *Eur. Phys. J.* **C76** (2016) 196, [[1512.01178](#)].
- [132] G. Curci, W. Furmanski and R. Petronzio, *Evolution of parton densities beyond leading order: The non-singlet case*, *Nuclear Physics B* **175** (1980) 27 – 92.
- [133] S. Frixione and B. R. Webber, *The MC@NLO 2.0 event generator*, [hep-ph/0307146](#).
- [134] S. Frixione, P. Nason and C. Oleari, *Matching NLO QCD computations with Parton Shower simulations: the POWHEG method*, *JHEP* **11** (2007) 070, [[0709.2092](#)].
- [135] S. Alioli, P. Nason, S. Milano-bicocca, P. Scienza and C. Oleari, *The POWHEG BOX user manual: common features*. <http://powhegbox.mib.infn.it>, 2011.
- [136] J. Alwall et al., *A Standard format for Les Houches event files*, *Comput. Phys. Commun.* **176** (2007) 300–304, [[hep-ph/0609017](#)].
- [137] J. Baglio, B. Jäger and M. Kesenheimer, *Electroweakino pair production at the LHC: NLO SUSY-QCD corrections and parton-shower effects*, *JHEP* **07** (2016) 083, [[1605.06509](#)].

## Bibliography

- [138] J. Baglio, B. Jäger and M. Kesenheimer, *Precise predictions for electroweakino-pair production in association with a jet at the LHC*, 1711.00730.
- [139] T. Hahn and M. Perez-Victoria, *Automatized one loop calculations in four-dimensions and D-dimensions*, *Comput. Phys. Commun.* **118** (1999) 153–165, [[hep-ph/9807565](#)].
- [140] T. Hahn, *Generating Feynman diagrams and amplitudes with FeynArts 3*, *Comput. Phys. Commun.* **140** (2001) 418–431, [[hep-ph/0012260](#)].
- [141] E. Re, *Single-top  $Wt$ -channel production matched with parton showers using the POWHEG method*, *Eur. Phys. J.* **C71** (2011) 1547, [[1009.2450](#)].
- [142] F. Demartin, B. Maier, F. Maltoni, K. Mawatari and M. Zaro,  *$tWH$  associated production at the LHC*, *Eur. Phys. J.* **C77** (2017) 34, [[1607.05862](#)].
- [143] T. Plehn and C. Weydert, *Charged Higgs production with a top in MC@NLO*, *PoS CHARGED2010* (2010) 026, [[1012.3761](#)].
- [144] R. Gavin, C. Hangst, M. Krämer, M. Mühlleitner, M. Pellen, E. Popena et al., *Matching Squark Pair Production at NLO with Parton Showers*, *JHEP* **10** (2013) 187, [[1305.4061](#)].
- [145] R. Gavin, C. Hangst, M. Krämer, M. Mühlleitner, M. Pellen, E. Popena et al., *Squark Production and Decay matched with Parton Showers at NLO*, *Eur. Phys. J.* **C75** (2015) 29, [[1407.7971](#)].
- [146] D. Gonçalves-Netto, D. López-Val, K. Mawatari, T. Plehn and I. Wigmore, *Automated Squark and Gluino Production to Next-to-Leading Order*, *Phys. Rev.* **D87** (2013) 014002, [[1211.0286](#)].
- [147] S. Catani, S. Dittmaier, M. H. Seymour and Z. Trocsanyi, *The Dipole formalism for next-to-leading order QCD calculations with massive partons*, *Nucl. Phys.* **B627** (2002) 189–265, [[hep-ph/0201036](#)].
- [148] D. G. Netto, *NLO Predictions for New Physics at the LHC*. PhD thesis, University Heidelberg, 2012.
- [149] B. Jäger, A. von Manteuffel and S. Thier, *Slepton pair production in the POWHEG BOX*, *JHEP* **10** (2012) 130, [[1208.2953](#)].

- [150] B. Jäger, A. von Manteuffel and S. Thier, *Slepton pair production in association with a jet: NLO-QCD corrections and parton-shower effects*, *JHEP* **02** (2015) 041, [1410.3802].
- [151] T. Fritzsche, T. Hahn, S. Heinemeyer, F. von der Pahlen, H. Rzehak and C. Schappacher, *The Implementation of the Renormalized Complex MSSM in FeynArts and FormCalc*, *Comput. Phys. Commun.* **185** (2014) 1529–1545, [1309.1692].
- [152] G. 't Hooft and M. J. G. Veltman, *Scalar One Loop Integrals*, *Nucl. Phys.* **B153** (1979) 365–401.
- [153] G. J. van Oldenborgh, *FF: A Package to evaluate one loop Feynman diagrams*, *Comput. Phys. Commun.* **66** (1991) 1–15.
- [154] H. Murayama, I. Watanabe and K. Hagiwara, *HELAS: HELicity amplitude subroutines for Feynman diagram evaluations*, Tech. Rep. KEK-91-11, 1992.
- [155] T. Stelzer and W. F. Long, *Automatic generation of tree level helicity amplitudes*, *Comput. Phys. Commun.* **81** (1994) 357–371, [hep-ph/9401258].
- [156] J. Alwall, P. Demin, S. de Visscher, R. Frederix, M. Herquet, F. Maltoni et al., *MadGraph/MadEvent v4: The New Web Generation*, *JHEP* **09** (2007) 028, [0706.2334].
- [157] B. C. Allanach et al., *The Snowmass points and slopes: Benchmarks for SUSY searches*, *Eur. Phys. J.* **C25** (2002) 113–123, [hep-ph/0202233].
- [158] W. Beenakker, M. Klasen, M. Krämer, T. Plehn, M. Spira and P. M. Zerwas, *The Production of charginos / neutralinos and sleptons at hadron colliders*, *Phys. Rev. Lett.* **83** (1999) 3780–3783, [hep-ph/9906298].
- [159] J. Butterworth et al., *PDF4LHC recommendations for LHC Run II*, *J. Phys.* **G43** (2016) 023001, [1510.03865].
- [160] A. Buckley, J. Ferrando, S. Lloyd, K. Nordström, B. Page, M. Rüfenacht et al., *LHAPDF6: parton density access in the LHC precision era*, *Eur. Phys. J.* **C75** (2015) 132, [1412.7420].
- [161] T. Sjöstrand, S. Mrenna and P. Z. Skands, *PYTHIA 6.4 Physics and Manual*, *JHEP* **05** (2006) 026, [hep-ph/0603175].

## Bibliography

- [162] M. Cacciari, G. P. Salam and G. Soyez, *FastJet User Manual*, *Eur. Phys. J.* **C72** (2012) 1896, [1111.6097].
- [163] P. Z. Skands et al., *SUSY Les Houches accord: Interfacing SUSY spectrum calculators, decay packages, and event generators*, *JHEP* **07** (2004) 036, [hep-ph/0311123].
- [164] B. C. Allanach et al., *SUSY Les Houches Accord 2*, *Comput. Phys. Commun.* **180** (2009) 8–25, [0801.0045].
- [165] A. Djouadi, J.-L. Kneur and G. Moultaka, *SuSpect: A Fortran code for the supersymmetric and Higgs particle spectrum in the MSSM*, *Comput. Phys. Commun.* **176** (2007) 426–455, [hep-ph/0211331].
- [166] M. Mühlleitner, A. Djouadi and Y. Mambrini, *SDECAY: A Fortran code for the decays of the supersymmetric particles in the MSSM*, *Comput. Phys. Commun.* **168** (2005) 46–70, [hep-ph/0311167].
- [167] D. Francescone, S. Akula, B. Altunkaynak and P. Nath, *Sparticle Mass Hierarchies, Simplified Models from SUGRA Unification, and Benchmarks for LHC Run-II SUSY Searches*, *JHEP* **01** (2015) 158, [1410.4999].
- [168] F. J. Tackmann, W. J. Waalewijn and L. Zeune, *Impact of Jet Veto Resummation on Slepton Searches*, 1603.03052.
- [169] ATLAS collaboration, G. Aad et al., *Search for direct pair production of a chargino and a neutralino decaying to the 125 GeV Higgs boson in  $\sqrt{s} = 8$  TeV  $pp$  collisions with the ATLAS detector*, *Eur. Phys. J.* **C75** (2015) 208, [1501.07110].
- [170] A. Denner, S. Dittmaier and L. Hofer, *Collier: a fortran-based Complex One-Loop Library in Extended Regularizations*, *Comput. Phys. Commun.* **212** (2017) 220–238, [1604.06792].
- [171] J. Taylor, *Ward identities and charge renormalization of the yang-mills field*, *Nuclear Physics B* **33** (1971) 436 – 444.
- [172] A. A. Slavnov, *Ward Identities in Gauge Theories*, *Theor. Math. Phys.* **10** (1972) 99–107.
- [173] A. A. Slavnov, *Slavnov-Taylor identities*, *Scholarpedia* **3(10):7119** (2008) .



- [174] J. Collins, F. Wilczek and A. Zee, *Low-energy manifestations of heavy particles: Application to the neutral current*, *Phys. Rev. D* **18** (Jul, 1978) 242–247.
- [175] R. Harlander, L. Mihaila and M. Steinhauser, *Two-loop matching coefficients for the strong coupling in the MSSM*, *Phys. Rev.* **D72** (2005) 095009, [[hep-ph/0509048](#)].
- [176] R. V. Harlander and M. Steinhauser, *Supersymmetric Higgs production in gluon fusion at next-to-leading order*, *JHEP* **09** (2004) 066, [[hep-ph/0409010](#)].
- [177] G. Cullen, N. Greiner and G. Heinrich, *Susy-QCD corrections to neutralino pair production in association with a jet*, *Eur. Phys. J.* **C73** (2013) 2388, [[1212.5154](#)].
- [178] ATLAS collaboration, M. Aaboud et al., *Search for the direct production of charginos and neutralinos in  $\sqrt{s} = 13$  TeV pp collisions with the ATLAS detector*, [1708.07875](#).
- [179] ATLAS collaboration, G. Aad et al., *Search for new phenomena in final states with an energetic jet and large missing transverse momentum in pp collisions at  $\sqrt{s} = 8$  TeV with the ATLAS detector*, *Eur. Phys. J.* **C75** (2015) 299, [[1502.01518](#)].
- [180] ATLAS collaboration, *Monojet Analysis Performance Plots with  $68 - 78pb^{-1}$  of 13TeV data collected by the ATLAS experiment*, Tech. Rep. ATLAS-EXOT-2015-005, 2015.
- [181] M. Maniatis, *The Next-to-Minimal Supersymmetric extension of the Standard Model reviewed*, *Int. J. Mod. Phys.* **A25** (2010) 3505–3602, [[0906.0777](#)].
- [182] U. Ellwanger, C. Hugonie and A. M. Teixeira, *The Next-to-Minimal Supersymmetric Standard Model*, *Phys. Rept.* **496** (2010) 1–77, [[0910.1785](#)].
- [183] L. Pickering, P. Stowell and J. Sobczyk, *Event reweighting with the NuWro neutrino interaction generator*, *J. Phys. Conf. Ser.* **888** (2017) 012175, [[1610.07053](#)].